ATLAS

Letter of Intent

Phase-I Upgrade

Letter of Intent

Phase-I Upgrade

Letter of Intent for the Phase-I Upgrade of the ATLAS Experiment

ATLAS Collaboration

ABSTRACT:

After the first successful years of running at the LHC, the ATLAS Collaboration is preparing to fully exploit the unprecedented physics opportunities offered by exploration of a completely new energy domain. This program builds on the excellent LHC accelerator complex performance demonstrated to date. A plan to consolidate and improve the physics capabilities of the current detector over the next decade, targeting the 2018 LHC shutdown as installation milestone, is presented in this Letter of Intent. The document primarily addresses the proposed enhancements to the ATLAS trigger system to cope with luminosities beyond the LHC nominal design value, while retaining the same physics performance. The Phase-I upgrades will allow ATLAS to maintain low p_T trigger thresholds for isolated leptons by increasing the granularity of the calorimeters involved in the Level-1 trigger and by introducing new muon trigger and tracking detectors in the forward direction. Precision measurements of the couplings of the Higgs boson, if found in the low mass region, as well as searches for supersymmetric particles in a large region of the SUSY parameter space, rely on the capability of efficiently selecting low p_T isolated leptons. Fast accurate tracking information provided near the start of the Level-2 trigger processing will lead to much more effective identification of events with isolated τ and b-hadrons, improving the selection of Higgs boson decays and sensitivity to many other physics channels. Finally, a new set of very far forward detectors will enable ATLAS to explore the new diffractive physics domain made accessible by the LHC energies and luminosities, providing an unprecedented sensitivity to large momentum transfer processes.

KEYWORDS: ATLAS, LHC, HL-LHC, Upgrade, CERN.

Contents

1. Introduction

The Large Hadron Collider (LHC) offers the best opportunities for exploration of new physics and for precision measurements of known phenomena at the energy frontier.

The collider began operations in 2009 and has delivered over 5 fb^{-1} of data with luminosities peaking at 3×10^{33} cm^{-2} s^{-1} at a center of mass energy of 7 TeV.

In 2012, the LHC is expected to continue its operation at a center of mass energy of 8 TeV and to deliver 10 to 20 fb^{-1} to the experiments. The repair of the splices in the main accelerator during a long shutdown in 2013-2014 (LS1) will allow the LHC to continue its operation (Phase-0) at its design parameters for the center of mass energy and the peak luminosities (10^{34} cm^{-2} s^{-1}) from 2015, which would allow ATLAS to collect a luminosity of 50-100 fb^{-1}.

A second shutdown (LS2) is being planned in 2018 to integrate the Linac4 into the injector complex, to increase the energy of the PS Booster to reduce the beam emittance, and to upgrade the collider collimation system. When data taking resumes in 2019 (Phase-I), the peak luminosity is expected to reach 2-3 $\times 10^{34}$ cm^{-2} s^{-1} corresponding to 55 to 80 interactions per crossing (pile-up) with 25 ns bunch spacing, well beyond the initial design goals. ATLAS Phase-I upgrades will enable the experiment to exploit the physics opportunities afforded by the upgrades to the accelerator complex. In particular, Phase-I will allow collection of an integrated luminosity of 300-400 fb^{-1}, extending the reach for discovery of new physics and the ability to study new phenomena and states. Furthermore, these upgrades are designed to be fully compatible with the physics program of the high luminosity HL-LHC, where the instantaneous luminosity should reach 5-7$\times 10^{34}$ cm^{-2} s^{-1} for a total integrated luminosity of 3,000 fb^{-1} (Phase-II).

The excellent performance of the LHC accelerator in 2011 has proven the ability to deliver luminosity that exceeds expectations and it is therefore prudent to plan for higher than anticipated luminosity and pile-up conditions, which go well beyond the initial design parameters of the detector.

ATLAS maintains a rich and diverse physics program with a strong emphasis on probing the origin of the electroweak symmetry breaking, as predicted by the Standard Model (SM), which leads to a major focus on the Higgs boson. ATLAS is sensitive to the allowed mass range and has already excluded most of this mass range above 130 GeV, using data from the 2011 running. With increased statistics, the SM Higgs should be either discovered or excluded in the coming year.

In the first case, during Phase-0, the various Higgs decay modes will be observed. Phase-I will provide an ideal laboratory to make precision measurements of the Higgs boson properties, and in particular its couplings to fermions and bosons. For example, the measurement of the couplings via the final states WH with the Higgs boson decaying as $H \rightarrow \tau\tau$, $H \rightarrow b\bar{b}$, $H \rightarrow WW^*$, $H \rightarrow ZZ^*$ measured by tagging the W-boson lepton, would allow reduction of the systematics due to the Higgs production mechanism. A low p_T ($\sim$25-30 GeV/c) single isolated lepton trigger will be used to select these events since its efficiency can be determined with high accuracy. A good resolution to identify final states with τ and b displaced vertices is also required.

If the Higgs is excluded, WW scattering measurements will become essential to unveil the electroweak symmetry breaking mechanism. Low p_T isolated lepton triggers and large acceptance in the forward direction are again required to maximize the signal efficiency.

Furthermore, ATLAS will continue the search for new phenomena or new particles that are predicted by alternative models and theories, such as supersymmetry (SUSY), technicolor, compositeness, extra-dimensions, etc. Important elements in SUSY searches, for example, demand sensitivity to a low p_T lepton ($\sim$25 GeV), produced through cascade decays, as well as a low threshold high efficiency missing E_T trigger.

In all cases, ATLAS capability to maintain an optimal trigger system as the luminosity increases beyond its nominal design value requires a strong reduction of the main source of backgrounds: jets mimicking electrons in the calorimeters and fake muons in the forward spectrometer. Otherwise, increased threshold cuts would have to be deployed to control rates that would reduce significantly the signal efficiency (by over a factor of two in the case of the WH associated production and in some currently favored SUSY scenarios). The success of the overall ATLAS physics program during Phase-I data taking is therefore dependent on the implementation of the upgrades proposed in this document.

The present Letter of Intent addresses the issue of improving the present Level-1 trigger of the ATLAS experiment, to be able to keep an acceptable trigger rate, while keeping present p_T thresholds for single isolated electrons and muons. This will be achieved in the case of the muon spectrometer by introducing a new tracking and trigger device in the inner layer of the forward spectrometer, that will not only provide a sharper trigger threshold, but also greatly improve the tracking performance under the higher backgrounds expected with the LHC upgrades. Similarly, for the case of electrons, new trigger read-out boards will be implemented in the electromagnetic and forward calorimeters to exploit the longitudinal sampling of the calorimeter as well as including a higher trigger granularity comparable to that presently available in the full calorimeter read-out, which will lead to an improvement in rejecting fake electron triggers. A new topological processor will add significant flexibility to the Level-1 trigger system. Fast accurate tracking at Level-2 trigger will permit the isolation of τ and b events and therefore improve the quality of the selected events without any substantial increase in rates. Finally, a new set of forward detectors will permit ATLAS not only to retain its capabilities for forward physics at the highest possible LHC luminosities, but to place the best possible limits on quartic gauge coupling of $\gamma\gamma WW$. Most of the arguments for the Phase-I upgrade of ATLAS are related to the trigger improvements needed to keep the physics capabilities of the experiment. However, preserving the full functionality of all the detector elements is also a critical factor to keep the physics capabilities of ATLAS. High radiation levels and high data rate could lead to a deterioration of the vertex detector, degrading the tagging of short live particles, while high background rates could affect the rapidity coverage of the forward calorimeters (increasing the rate of fake large missing E_T triggers). The possibilities of performing upgrades to the pixel system and/or to the forward calorimeter are therefore also briefly discussed in this LoI. However, current simulations and detector performance extrapolations suggest that such changes should not be required until Phase-II, but they would be the subject of separate documents if either will prove to be necessary sooner.

2. Detector Requirements for Operation Beyond Design Luminosity

2.1 Introduction

The LHC plans, as of today, are to deliver to ATLAS after the LS2 shutdown an instantaneous luminosity of $2 \times 10^{34} \mathrm{cm}^{-2}\mathrm{s}^{-1}$ or higher, with a 25 ns beam crossing rate, corresponding to ~ 55 interactions per beam crossing (μ) at design energy. It is prudent to plan at this stage an additional safety factor of about 30%, equivalent to an instantaneous luminosity of $3 \times 10^{34} \mathrm{cm}^{-2}\mathrm{s}^{-1}$ and to $\mu \sim 80$. The associated integrated luminosity is then 400 fb^{-1}. When estimating the total doses and particle fluences to qualify the electronics for the necessary radiation hardness, a further safety factor of 2 should be applied to take into account the uncertainties on the simulation predictions.

Furthermore, any component installed in Phase-I needs to be fully operational in ATLAS also through Phase-II, requiring therefore to be compatible with $7 \times 10^{34} \mathrm{cm}^{-2}\mathrm{s}^{-1}$, $\mu \sim 200$, and 3000 fb^{-1} of integrated luminosity.

How the inner detectors, the calorimeters, the muon spectrometer and the relevant triggers perform under conditions after LS2, is described in this chapter. Detector occupancy, detector resolution, trigger rates and trigger thresholds are discussed in detail, starting from the knowledge acquired so far during the current operations and data taking.

2.2 The planned upgrade of the muon spectrometer

In the muon spectrometer trigger rates, detector occupancy and momentum resolution are strongly affected by the level of background present in the cavern, both from particles generated at the interaction point, and from halo particles in the proton beams. This effect will increase as the peak luminosity evolves.

These backgrounds can be understood and predicted by a full simulation of the detector response, as well from the experience gained in the first years of running. The comparison of these two aspects allows extrapolation, with some confidence, of the detector performance with the evolving beam conditions.

The details of the muon spectrometer layout are presented in Figure 2.1 which shows a quadrant of the ATLAS detector along the beam axis (z-direction). The spectrometer is organized in three stations for the barrel: Barrel Inner (BI), Barrel Middle (BM) and Barrel Outer (BO). For the end-caps, the three stations correspond to End-cap Inner (EI), End-cap Middle (EM) and End-cap Outer (EO) as shown in Fig. 2.1. The sub-index "L", shown in the figure, refers to the large chambers. Each station contains Monitored Drift Tubes (MDT) as tracking devices, except for part of the EI station, Resistive Plate Chambers (RPC) in the BM and BO stations, and Thin Gap Chambers (TGC) in the EI and EM stations acting as trigger devices. The EI station consists of Cathode Strip Chambers (CSC) and EIL1,2,3,4 MDTs and TGCs chambers. Mechanically the End-cap Inner is organized in two separate structures: the inner part containing CSC and EIL1-3 is a single disk structure (the small wheel), while the outer EIL4 chambers form a ring structure surrounding the small wheel and supported inside the barrel part of the spectrometer. The η coverage of the small wheel is $|\eta| = 1.3 - 2.7$, which is about 50% of the $|\eta|$ acceptance of the muon spectrometer.
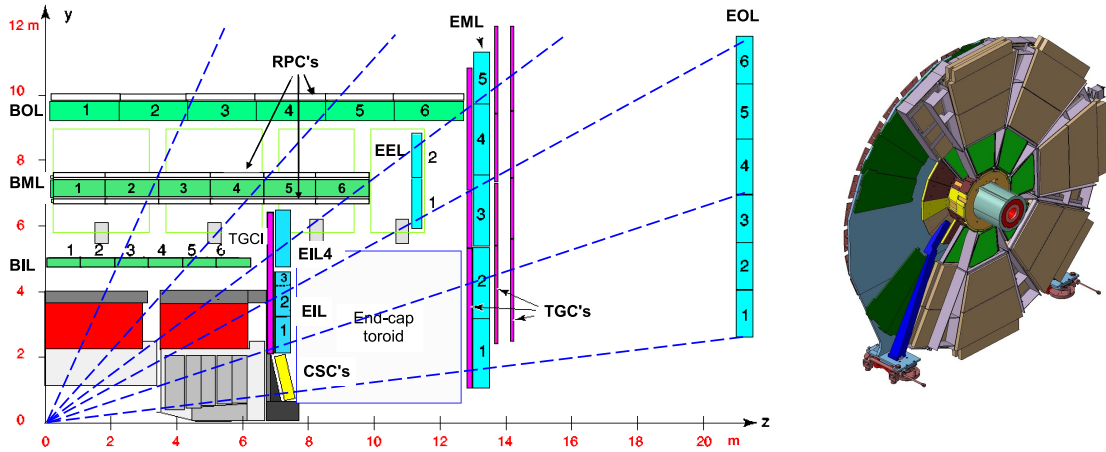
Figure 2.1. Left: A z-y view of 1/4 of the ATLAS detector. The blue boxes indicate the end-cap MDT chambers and the yellow box CSC. Right: A view of a small wheel mounted on the JD disk shielding.

2.2.1 Present understanding of the backgrounds in the muon spectrometer

In order to be able to extrapolate the expected background to higher LHC luminosities and energies, and to evaluate possible improvements, a careful comparison between data and Monte Carlo predictions has been performed using LHC data at luminosities in the range $1\text{-}3 \times 10^{33}$ cm^{-2} s^{-1}. These studies have taken into account the measured hit rates in the MDT chambers, as well as the HV currents in the RPC trigger detectors. Figure 2.2 shows the ratio of the measured hit rates to the corresponding simulation values for different MDT chambers. Except for the z=7 m region in the Barrel Inner (BI) station, the ratio is typically between 0.5 and 1.7.
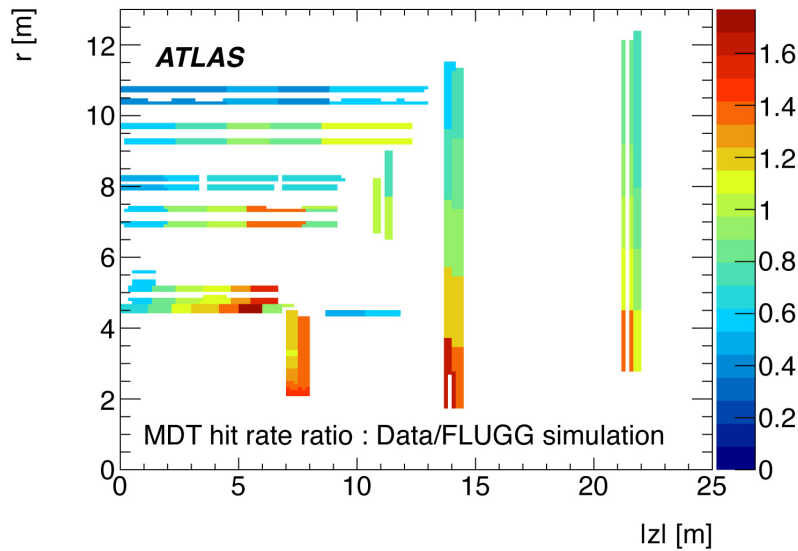
Figure 2.2. Ratio of measured to simulated MDT hit rate in during 2011 7 TeV run
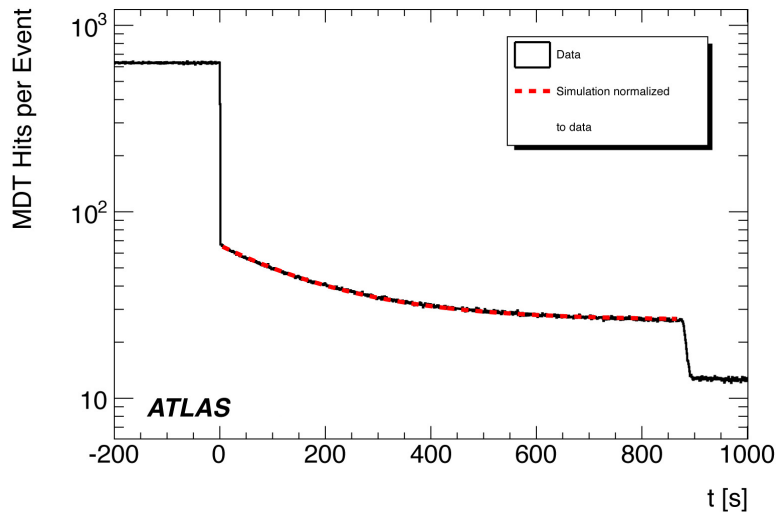
Figure 2.3. Time dependence of background. The measured hit rate in MDT after beam dump is in black. The drop at ∼900 seconds is the result of turning off HV. In red is a fit with an exponential function whose time constant is set equal to the time constant from simulations.

The barrel region at z=7 m, especially in the BI chambers, has high rates because of a gap in the shielding that allows background from the beam pipe region to exit unimpeded. This will be corrected by introducing additional shielding during the 2011-2012 winter shutdown.

The RPC HV power supply currents, which are linear with luminosity, provide precise time-averaged measurements of the total hit rates without the duty factor inherent in hits determined from triggered events. The conversion of HV current back to hit rates is sensitive to the composition of incident flux as well as their energy spectra. Incident fluxes from simulation are convoluted with the energy-dependent sensitivity of the RPC chambers to give the expected hit rates.

The agreement between data and simulation rates for the large sectors of BM and BO is at the ∼ 30% level.

The short-term time structure of background from individual p-p collisions is obscured by nearby bunch crossings; however, the long-term time structure due primarily to radioactive decays can be observed after beam removal. The measured MDT hit rate after beam dump is well described by an exponential with a time constant of 200 sec as shown in Fig. 2.3. Simulations predict the same time constant.

In summary, data and simulation agree to better than a factor of two with the largest discrepancy in the small wheel of ∼1.7 at the small radius region. This result gives confidence in the evaluation of the expected rates at higher LHC luminosities.

Most of the p-p collision products go forward. They hit the stainless steel beam pipe at grazing angle, and a hadronic shower is initiated. A lighter beam pipe material reduces this background. Non-interacting products of p-p collisions do not shower until they hit the shielding material, which happens at much greater distance from the interaction point due to the shallow angle of these particles. The shielding at large z is thicker and thus contains the showers more completely. A new aluminium beam pipe has been designed. It is being fabricated, and is scheduled for installation

during the 2013-2014 shutdown. The implementation of the aluminium beam pipe will reduce the background rate in the small wheel region by 30%. Furthermore a Li-doped polyethylene wall situated downstream of the end-cap toroid will be installed. Such a wall should reduce the neutron flux on the EM layer by as much as a factor 2, allowing this part of the detector to only be exposed to the present level of background, even after the Phase-I luminosity upgrade.

2.2.2 Muon spectrometer occupancy

In this section arguments will be raised to prove that in the end-cap region, and in particular in the first muon station (small wheel), the expected hits rate exceeds the existing detector capability and compromises the muon tracking performance. The small wheel was designed to be operational and to maintain its performance up to the condition of the nominal LHC luminosity, $1 \times 10^{34} \mathrm{cm}^{-2} \mathrm{s}^{-1}$, including a safety factor of 5 with respect to the cavern background level estimated at the time of designing the detector. However, the actual background level has been found to be higher than these original estimates. More recent simulations agree much better with the hit rate measurements, providing a more reliable estimate of the expectations for future operation, but the safety margins are significantly reduced.

Direct hit rate measurements using the muon detector have been performed at the current luminosities [1]. Figure 2.4 (left) shows the result from MDTs and CSCs in the small wheel region. The discontinuity at R∼210 cm is caused by the different sensitivity of MDTs and CSCs to cavern background particles. The expectation by FLUGG simulation [2] is also shown in the same figure. The simulation and measurements agree well in terms of their radial dependence. The measured results are then used to estimate the background rate on the small wheel as a function of radial distance from the beams, in the assumption the same technology is used over the full acceptance of the small wheel. In Fig. 2.4 (right) the observed rate in MDT (R>210 cm) and CSC (R<200 cm) are scaled to the value corresponding to the nominal luminosity $1 \times 10^{34} \mathrm{cm}^{-2} \mathrm{s}^{-1}$. In addition the CSC curve is scaled to have the same value as the MDT's one at their boundary to simulate the condition of an all MDT-type detector scenario. Similarly, the MDT curve is scaled to simulate the all CSC-type detector case. A comparison of these curves indicates the possible dependency of the background hit rate on the detector technology. The maximum rate for the MDT is about 2 kHz/cm^2 at the smallest radius of 100 cm. This corresponds to 14 kHz/cm^2 at the maximum Phase-II luminosity of $7 \times 10^{34} \mathrm{cm}^{-2} \mathrm{s}^{-1}$.

The highest tolerable rate for the present MDT chambers is 200-300 kHz/tube [3]. For a tube of 1.3 m long and 30 mm diameter, corresponding to the tubes at the smallest radius (210 cm) in the present small wheel, this tube rate corresponds to 510-770 Hz/cm^2. All this indicates that the present MDT should still work at the nominal luminosity, but there is only a small margin for operation at higher luminosity. Therefore the existing small wheel requires a major change in technology and must be upgraded for Phase-I.

All this is based on the measurements at $\sqrt{s}$=7 TeV. The ratio of background rate at 14 TeV and 7 TeV is about 1.3 in the small wheel region according to the Monte Carlo simulation using FLUGG. This increase will however be compensated by the consolidation work expected up to LS1: additional new shielding in the narrow gap between the end-cap calorimeter cryostat and the JD shielding, and the installation of an aluminium beam pipe in the region of the end-cap
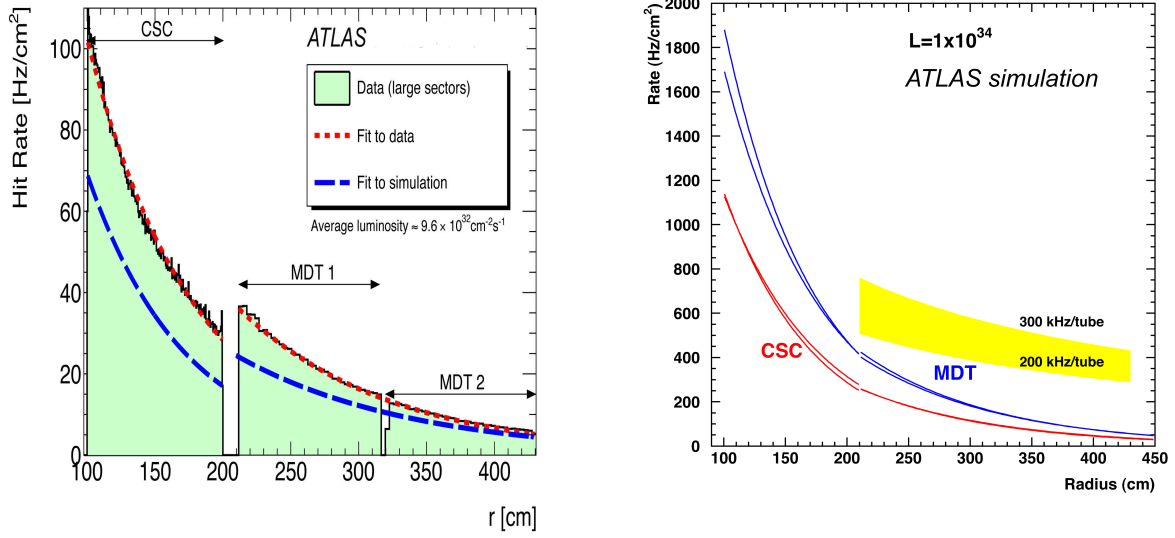
Figure 2.4. (Left) Measured hit rate of cavern background using MDT and CSC. Also shown are expectation of Monte Carlo simulation by FLUGG. (Right) Fitted curves obtained from the measured data of rate vs R, scaled to the nominal luminosity and by scaling the CSC curve to have the same value of the MDT one at the boundary (blue), and similarly scaling the MDT curve to CSC (red). The yellow band shows the area corresponding to the tube rate of 200-300 kHz/tube for the present 30 mm tubes.

calorimeter and the end-cap toroidal coils. The prediction in Fig. 2.4 is therefore taken as the central value of the expectation at 14 TeV.

2.2.3 Muon Level-1 trigger

Performance studies using collision data have shown the presence of unexpectedly high rates of fake triggers in the end-cap region. The relative trigger rates as a function of rapidity is shown for the L1MU20 trigger (a single muon of p_T threshold at 20 GeV) in Fig. 2.5. The rate is dominated by the contribution from the end-caps. The expectation at $\sqrt{s}$=14 TeV and at an instantaneous luminosity of $3 \times 10^{34} \mathrm{cm}^{-2}\mathrm{s}^{-1}$ is 60 KHz, to be compared to the total allowed Level-1 rate of 75-100 kHz.

Due to the limited p_T resolution of the Level-1 muon trigger system, raising the threshold above 20-30 GeV does not effectively reduce the rate and, furthermore, a higher threshold leads to a loss of physics acceptance as discussed in Chapter 9. Sharpening the Level-1 threshold is therefore necessary for the data taking in Phase-I and beyond. The Level-1 trigger upgrade addresses both the suppression of the fake triggers and improvement of the p_T resolution.

Presently, the Level-1 muon trigger in the end-cap is operating as follows. A track segment is identified first using hits on the 7 layers in the EM trigger chambers (TGC). Then, assuming the track is produced at the nominal IP position, its p_T is determined from the deviation of the segment angle from the direction pointing towards the nominal IP position. As a result, any background tracks in the magnetic field free region of the EM station can fake high p_T muons if their segments
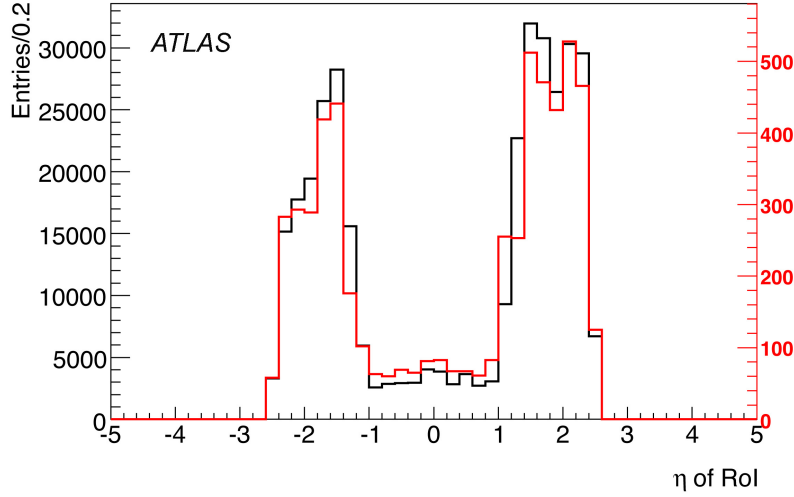
Figure 2.5. Relative trigger rate distribution as a function of η for the L1MU20 signal at 7 TeV. The red histogram is the 2011 data with 50 ns bunch spacing, and the black histogram is the 2010 data with 150 ns bunch spacing.

approximately point to the nominal IP as depicted in Fig. 2.6(a). Here the tracks B and C are background tracks causing fake triggers. The type B tracks are found to be mainly low momentum protons produced by collision of high energy neutrons with the materials of the end-cap toroid (e.g. the coils). This hypothesis is supported by the observed timing and time of flight between EM and EO stations for the tracks which are observed on EM and EO but not having associated hits in the small wheel.

Level-1 triggers caused by such background particles may be removed by requiring a corresponding activity in the small wheel, since such particles would have to traverse the end-cap magnetic field. Figure 2.6(b) shows how this works. For each EM trigger segment, by requiring the presence of a small wheel segment which is pointing toward the IP and matched to the corresponding EM segment in (η, ϕ), background triggers such as tracks B and C are efficiently removed. Studies have been made to see how well such approach works using collision data by emulating the small wheel segments in an upgraded detector using data from the existing detectors (MDT, CSC, TGC), The result is shown in Fig. 2.7. The left plot shows how the L1MU20 rate reduces by requiring i) the presence of small wheel segments, ii) the small wheel segment points to IP in θ ($|d\theta|$ typically less than 10 mrad) and iii) the small wheel segment matches in $(\eta - \phi)$ to the triggering EM segment ($|d\eta|$, $|d\phi|$ typically less than 0.1 rad). The L1MU20 rate is reduced by about one order of magnitude compared to the initial rate. The efficiency of these cuts for high quality and high p_T muons are also being studied, results are shown in Fig. 2.7. The efficiency is about 95%. Part of the loss due to the $d\theta$ cut is caused by poor angular resolution (long tail) of the CSC ($|\eta| = 2.0 - 2.7$). A higher signal efficiency is expected if the segment angle resolution of the new detector is as good as that of MDTs over the whole acceptance of the small wheel.

In today's L1MU20 trigger events, the fraction of high quality muons with $p_T > 20$ GeV is about 2% as shown in Fig. 2.7 in the right-most bin of the left plot. After the fake removal cuts,
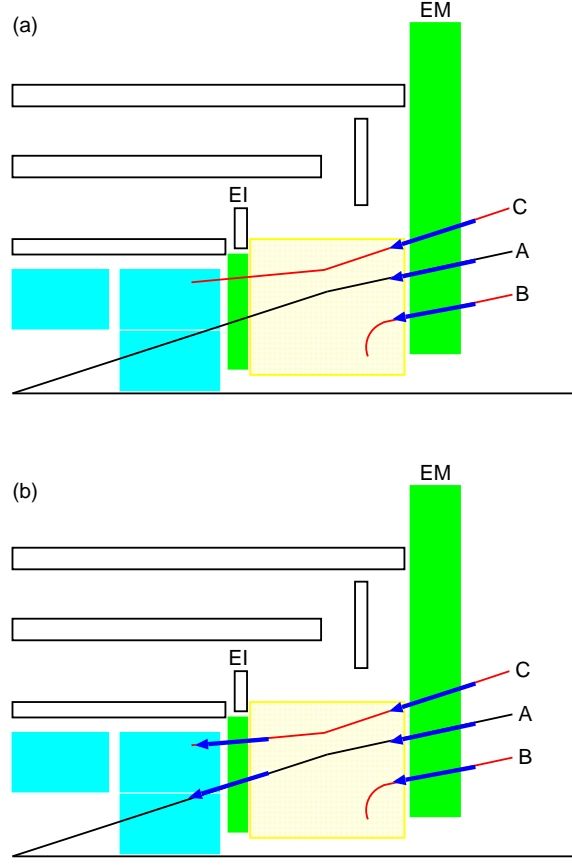
Figure 2.6. (a) EM segments producing Level-1 high p_T triggers. Track A is a high p_T muon originating from the IP. Tracks B and C are possible configurations of background segments. (b) By requiring an associated pointing segment on EI, background triggers may be eliminated.
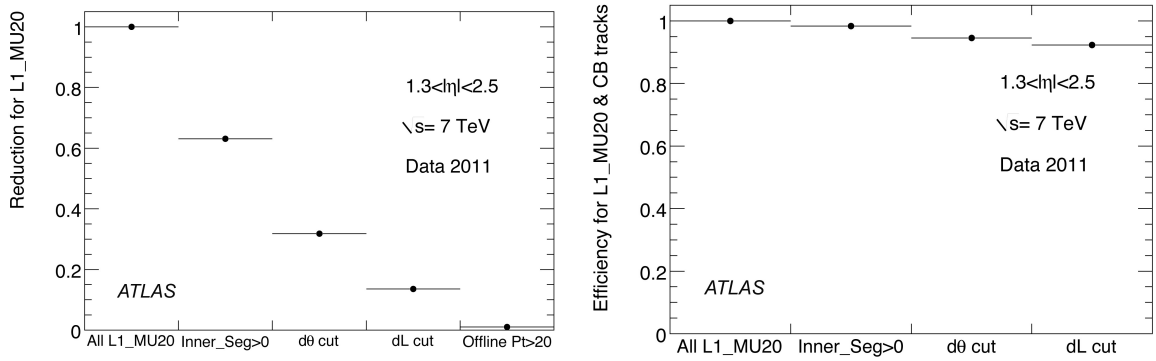
Figure 2.7. Left: Expected reduction of L1MU20 rate simulated using collision data by successive applications of requirements on the small wheel segments. Right: Efficiency for high quality high p_T muons due to the fake removal cuts.

the fraction still stays at a low level of ~10%. Figure 2.8 shows the p_T distribution of tracks found in the events with L1MU20 trigger set. The green histogram is the distribution after all the fake
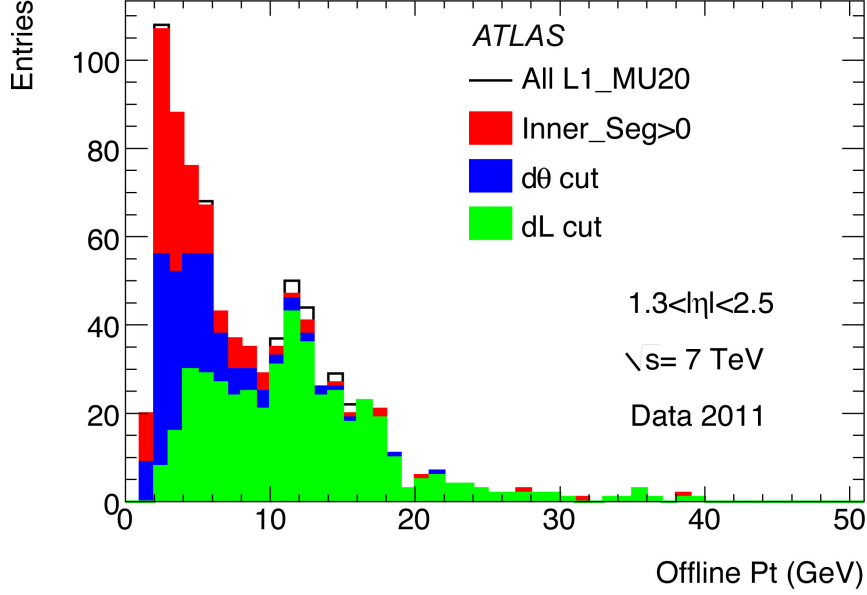
Figure 2.8. p_T distribution of high quality muons in the events with L1MU20.

removal cuts. There are still many low p_T muons below the nominal threshold of 20 GeV.

In order to reduce the low p_T components, the p_T resolution of the muon Level-1 system needs to be improved. The precision angle measurement at the small wheel can be used to improved the p_T resolution of the Level-1 trigger in the end-cap. In the present layout, the contributing factors to the p_T resolution are: i) angular resolution of EM trigger station ($\sim$ 3 mrad), ii) multiple scattering in the end-cap toroid ($\sim$ 0.5 mrad for high p_T muons), iii) multiple scattering in the calorimeters ($\sim$ 2-3 mrad), and iv) finite size of luminous region of p-p collision (corresponds to 1-2 mrad depending on η). Precision angle measurement by the small wheel can be used to eliminate the contributions iii) and iv) by correcting for these effects track by track, thus removing a part of the smearing effects to improve the p_T resolution. In order to achieve this improvement, a resolution of 1 mrad or better is required for the determination of the segment angle (angle relative to the pointing direction to IP) at the level of the small wheel. The expected improvement of p_T resolution is about 70%. Note that the 1 mrad requirement is compatible with the fake removal cuts discussed above for the $d\theta$ cut at 10 mrad (about 3σ of $d\theta$ distribution for good muons from the IP). Further improvements to reduce this rate will be performed for the Phase-II upgrade (see Chapter 10).

In summary, in order to effectively reduce the muon Level-1 trigger rate to the level of 10 kHz at ultimate luminosity, new small wheels must be constructed, capable to provide a trigger segment with a angular resolution of at least 1 mrad.

2.3 The calorimeter and its trigger system

As the LHC luminosity increases beyond its design value, the rates for most triggers involving

the calorimeters will increase linearly with luminosity (with the exception of the missing transverse energy and total scalar transverse energy triggers). For example, the rate for single isolated electromagnetic (EM) clusters above 23 GeV, projected to a luminosity of 2×10^{34} cm^{-2}s^{-1}, is approximately 80 kHz. Since in ATLAS the Level-1 total output rate in Phase-I will be limited to 75-100kHz, the existing Level-1 system will not be able to provide low thresholds with acceptable rates for electron and photon triggers. Further fine-tuning of the algorithms in the current Level-1 processors will lead to only modest performance improvements.

This section will show: i) how the rates will scale with increasing luminosity, and ii) what strategy and algorithms, currently used by the high-level triggers (HLT), ATLAS is planning to implement in the Level-1 calorimeter trigger system, in order to lower the rates for EM objects during Phase-I data taking.

Furthermore, the optimization of the Level-1 trigger menus during the 2010-2011 runs has indicated that the lowest single electron trigger should use approximately 10-20% of the total output trigger bandwidth. Therefore, a reasonable figure of merit to gauge how severe is the impact of the high luminosity pile-up on the performance of the trigger system and on ATLAS in general is the threshold corresponding to a 20 kHz trigger rate. The conclusions drawn in the following sections are based on this criterion.

2.3.1 Rate prediction at high pile-up with the existing Level-1 calorimeter trigger

Figure 2.9 shows the predicted EM thresholds at which a typical Level-1 trigger rate of 20 kHz will be measured, as a function of instantaneous luminosity. The 3 curves plotted in the figure correspond to different levels of noise suppression thresholds on each Level-1 trigger tower. At the instantaneous luminosity expected in the Phase-I run ($\mathscr{L} = 2 \times 10^{34}$cm^{-2}s^{-1}) the threshold is shown to be around 40-45 GeV, with the trigger being fully efficient above 50-55 GeV. The consequences are extremely severe since it would eliminate most of the W and Z signal.

Isolation requirements on Level-1 EM clusters would reduce effectively the overall rates, but they will not yet be sufficient to preserve thresholds below 30 GeV for the targeted 20 kHz rate. Figure 2.10 shows the expected rates for non-isolated and isolated Level-1 EM triggers as simulated with the current ATLAS detector for different values of the average number of interactions per beam crossing μ at $\sqrt{s} = 14$ TeV and with a bunch spacing of 25 ns. The isolation requirements for EM trigger objects are defined as threshold cuts on the energies deposited in rings surrounding the EM cluster for both the electromagnetic and hadronic calorimeters.

The curves in Figs. 2.10 are extracted from minimum bias Monte Carlo samples without simulation of cavern background, beam halo or beam gas effects, therefore providing an optimistic performance scenario .

2.3.2 High granularity trigger read-out, depth information and shower shape discriminants

The coarse granularity of the EM trigger towers, whose geometry is illustrated in Fig. 2.11, does not help to sufficiently discriminate against low p_T jets, which dominate the Level-1 EM rates at low E_T thresholds.

The calorimeter cells in each of the different sampling layers have different size by construction. Their analog signals are summed to form $\Delta\eta \times \Delta\phi = 0.1 \times 0.1$ trigger towers in 3 stages: in the shaper ASICs, in the Layer Sum Boards of the Front-End boards, and in the Trigger Tower
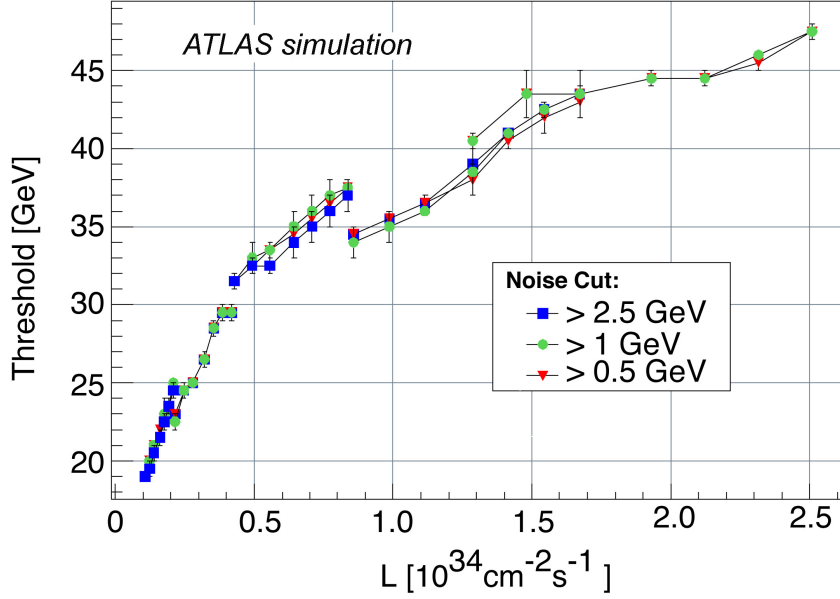
Figure 2.9. EM thresholds required to limit the Level-1 EM trigger rate to 20kHz as a function of instantaneous luminosity. The different curves correspond to different levels of noise suppression thresholds.
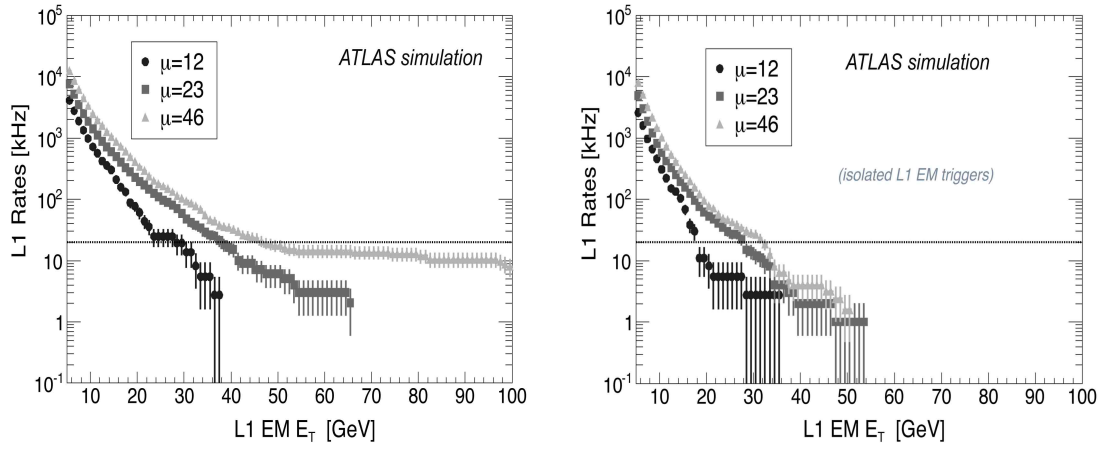
Figure 2.10. Rate vs. thresholds for the non-isolated (left) and isolated (right) Level-1 EM triggers for various values of μ (average number of minimum bias interactions per bunch crossing). The bunch-crossing spacing in the simulations is assumed to be 25 ns. The value $\mu=23$ corresponds to an instantaneous luminosity of $\mathscr{L} \simeq 8.5 \times 10^{33} \mathrm{cm}^{-2}\mathrm{s}^{-1}$.

Boards installed on-detector (see Chapter 4 for further details). A total of 64 read-out channels form an EM trigger tower.

At Level-2 and in the offline reconstruction, shower shape algorithms are currently used to improve electron identification and rejection against jets and π^os. The most effective discrimant

uses information from the second (Middle) layer of the EM calorimeter, measuring the lateral profile through the ratio of the energies deposited in clusters of 3×7 and 7×7 calorimeter cells in η,ϕ (i.e. equivalent to an area of $\Delta\eta \times \Delta\phi = 0.075 \times 0.175$ and $\Delta\eta \times \Delta\phi = 0.175 \times 0.175$ respectively) around the cluster seed defined as the "highest energy" calorimeter cell:

$$R_\eta = \frac{E_{3x7}}{E_{7x7}}$$

Preliminary studies show that shower shape algorithms based on finer granularity "Supercells" ($\Delta\eta \times \Delta\phi = 0.025 \times 0.1$) in the EM calorimeter's second layer achieve a background rejection factor for jets faking electrons similar to what is currently achieved in the Level-2 trigger with the full cell granularity.
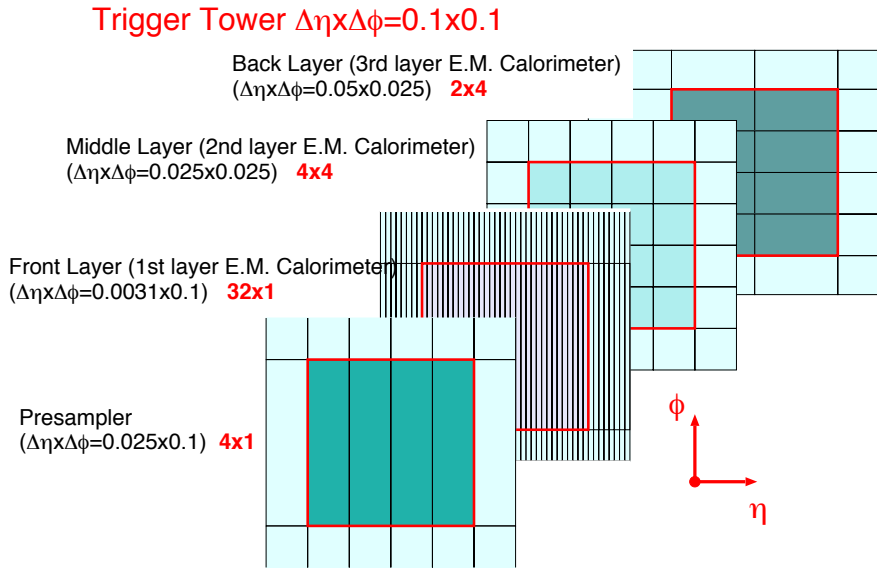
Figure 2.11. Geometrical representation of an EM trigger tower of the Liquid Argon calorimeters (LAr) in η,ϕ space.

These studies are based on a cluster seeding algorithm, which finds the highest energy Supercell ($\Delta\eta \times \Delta\phi = 0.025 \times 0.1$) within a pre-defined window of the initial RoI seed as provided by the current Level-1 position. The second highest energy slice in phi, above or below the seed, is selected for the calculation of the energies in the 3x2 and 7x2 "slice" clusters. The algorithm is shown schematically in Fig. 2.12.

The distribution of the R_η parameter for electrons and jets is shown in Fig. 2.13. Figure 2.14 shows the *"Receiving operating characteristic"* (ROC) curve, i.e. the efficiency for true electrons vs. the fraction of jets surviving the cut as the R_η discriminant threshold is varied. The ROC curve shows the effectiveness of the algorithm, given that it allows for a jet rejection factor between 3 and 4, while maintaining full efficiency (95-99%) on electrons.

2.3.3 Background rejection through isolation in the hadronic calorimeter

The importance of having depth layers from the hadronic calorimeters to suppress jet backgrounds has also been investigated.
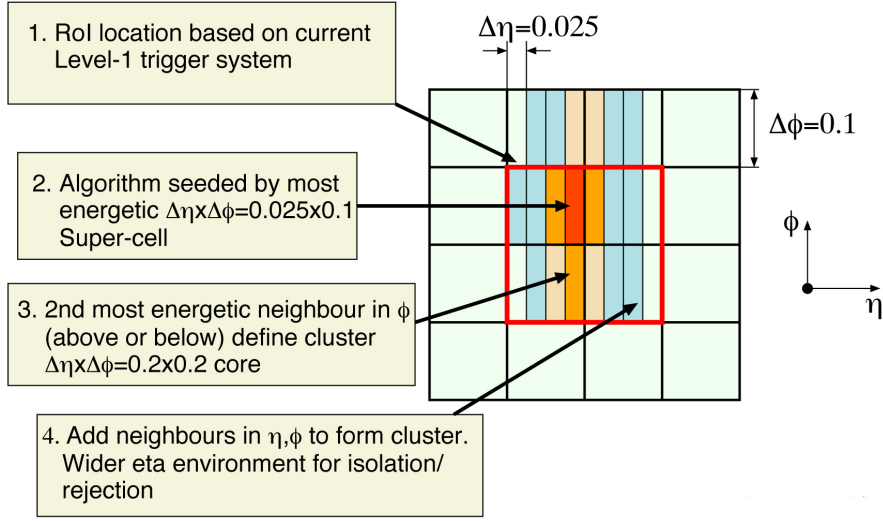
Figure 2.12. Shower shape calculations at Level-1 corresponding to the Level-2 and offline R_η parameter. The highest energy $\Delta\eta \times \Delta\phi = 0.025 \times 0.1$ "Super-cell" in the initial RoI, as provided by the current Level-1, is used to seed the 3x2 and 7x2 clusters; the second high energy "Super-cell" in ϕ, above or below the seed, is chosen to define the cluster core.
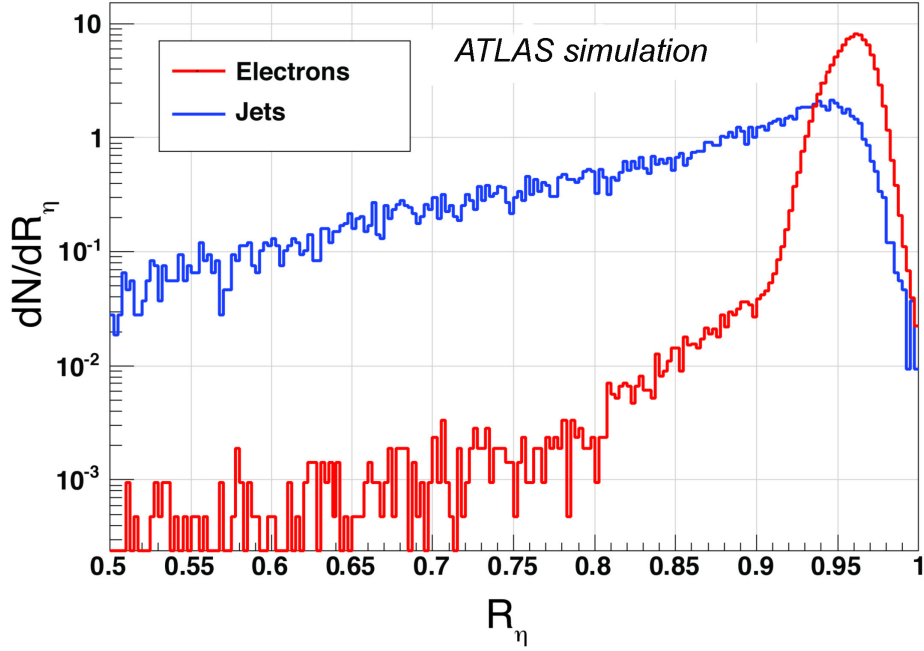
Figure 2.13. Distribution of the R_η parameter for electrons and jets, defined as the ratio of the energy in the 3x2 over the energy in the 7x2 clusters of the 2nd layer of the EM calorimeter. The size of each element in the cluster is: $\Delta\eta \times \Delta\phi = 0.025 \times 0.1$.

Table 2.1 summarizes the jet rejection efficiencies for cuts on several variables using information from the hadronic calorimeter. In the table "EM Cluster" refers to the energy deposited in a 2×1 or 1×2 η-ϕ trigger tower cluster, "EM Core" to the corresponding energy in the 2×2
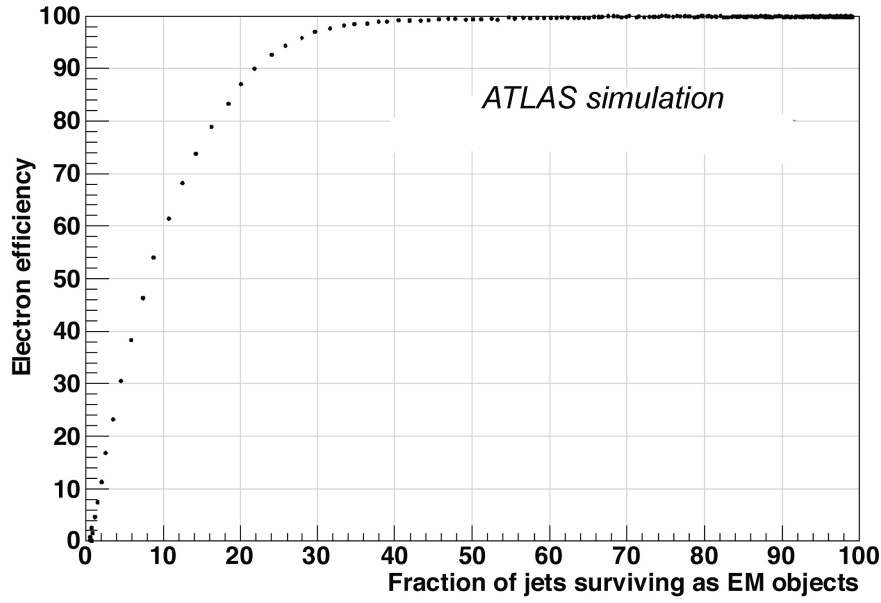
Figure 2.14. Electron efficiency vs. fraction of jets (%) surviving the parameter cut.

Cut variable and value	Cut Efficiency
Had core $E_T < 2.25$ GeV	0.51
Had core 1st layer $E_T < 1.00$ GeV	0.40
Had cluster (2×1) $E_T < 1.00$	0.47
Had cluster 1st layer $E_T < 0.75$ GeV	0.49
Had core fraction (Had 2×2/EM 2×2) < 0.08	0.60
Had core 1st layer fraction < 0.04	0.51
Had cluster fraction (Had 2×2/EM 2×2) < 0.03	0.45
Had cluster 1st layer fraction < 0.02	0.45
Had cluster 1st layer / EM cluster 2nd layer < 0.04	0.45
Had core 1st layer / EM core 2nd layer < 0.06	0.49

Table 2.1. Monte Carlo jet rejection efficiency for a 23 GeV p_T threshold (parameter values are tuned for 98% efficiency on electrons reconstructed offline) using the hadronic calorimeter information currently available in the Level-1 system.

cluster in the EM calorimeter. Similarly, "Had Cluster" and "Had Core" are defined as the energy deposited in the 1×2 or 2×1 and, respectively, 2×2, hadronic trigger towers behind the EM cluster. Table 2.1 shows also the effect of imposing cuts as fraction of the hadronic cluster/core to the EM corresponding quantities. The results have been obtained on Monte Carlo datasets for 23 GeV p_T threshold RoIs. The values of the cut parameters have been tuned for 98% efficiency on electrons reconstructed offline. In summary, no significant benefit is achieved by using individual layer information in the hadronic calorimeter vs. the full hadronic tower as far as the trigger electron efficiency and the jet rejection efficiency are concerned.

2.3.4 Expected rates in Phase-I with the proposed calorimeter trigger read-out upgrade

The rejection of jets with the discriminants described in sections 2.3.2 - 2.3.3 has been evaluated in QCD di-jet Monte Carlo samples and with enhanced bias data (i.e. data recorded with a very loose Level-1 trigger selection) taken during the 2011 run. The trigger efficiency of electrons has been calculated with $Z \to e^+ e^-$ Monte Carlo samples. Pileup effects for μ=46 and 25 ns bunch spacing are included in the Monte Carlo simulations.
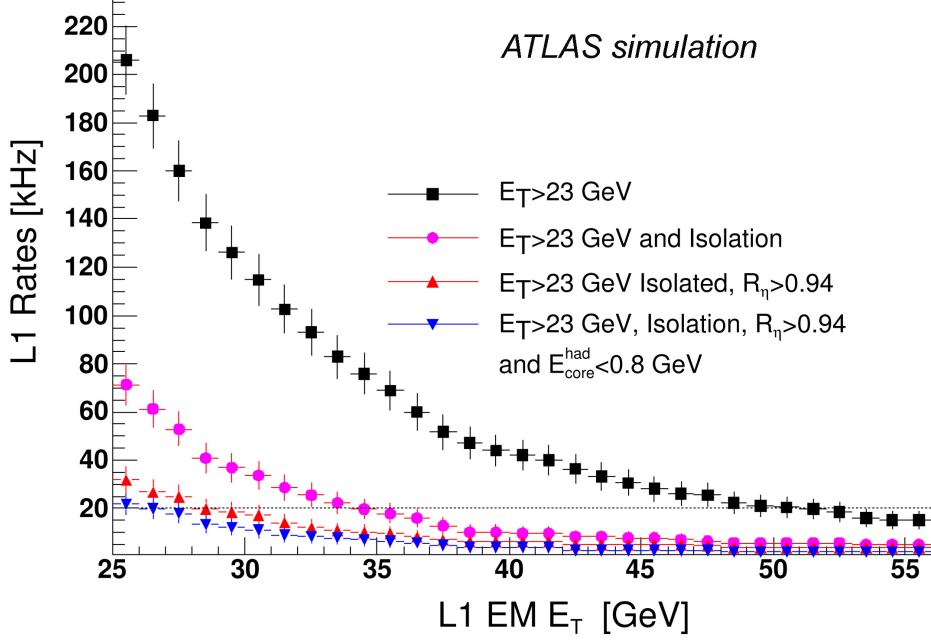
Figure 2.15. Expected Level-1 rates for different algorithms and conditions: rates calculated from Monte Carlo simulations with the current Level-1 trigger system for non-isolated EM objects (■), for isolated EM objects (●), for isolated EM objects after a shower shape $R_\eta > 0.94$ cut applied (▲), and after both $R_\eta > 0.94$ and $E_{core}^{had} < 0.8$ GeV cuts (▼). Monte Carlo simulations include pileup for μ=46 and with a bunch spacing of 25 ns.

A value R_η=0.94 has been chosen for this analysis: it provides an efficiency for true electrons above 99.3% and a jet rejection efficiency of 56.7% and 51.2% respectively on the Monte Carlo di-jet samples and on the 2011 enhanced bias data.

A further reduction of the Level-1 rates can be achieved by using higher energy resolution in the hadronic calorimeter trigger towers. Currently, the quantization of the calorimeter trigger read-out limits the precision to 1 GeV. For electrons with transverse energies in the range 20<E_T<80 GeV, higher resolution improves the rejection capability: in these studies it was assumed the digitizers having a 250 MeV least significant bit and a cut on the hadronic core energy $E_{core}^{had} \leq 800$ MeV has been applied.

Figure 2.15 shows the expected rates for EM non-isolated and isolated objects with the present Level-1 calorimeter trigger. The figure shows also the impact in the rate reduction when applying separately R_η and the combination (R_η and E_{core}^{had}). Furthermore, the plots show also the thresholds

required for a 20 kHz allocated bandwidth to EM triggers and confirms the results from minimum bias datasets described earlier in Section 2.3.1. It is clear from these results that ATLAS sensitivity to most channels with W or Z in the final states will be severely compromised. However, the conditions are recovered when both R_η and E_{core}^{had} cuts are applied: the 20 kHz threshold is lowered to around 25 GeV.

Finally, Table 2.2 summarizes the rate reduction shown in Fig. 2.15 for a threshold of E_T=23 GeV. The overall jet rejection with respect to the present Level-1 system for non-isolated and isolated objects is about a factor 9 and 3 respectively.

Both the previous arguments prove that the proposed upgrade is necessary for the operations of the Level-1 calorimeter trigger and to fully maintain the ATLAS physics search capabilities during the Phase-I data taking.

Selection criteria	Rate reduction	
	Fraction of (1)	Fraction of (2)
(1): Level-1 EM $E_T > 23$ GeV	100%	-
(2): (1) and Level-1 isolation	34.9%	100%
(3): (2) and R_η	14.25%	40.8%
(4): (3) and E_{core}^{had}	11.45%	32.8%

Table 2.2. Fraction of jet passing the Level-1 EM trigger with the present Level-1 isolation algorithms and with new discriminant variables.

2.3.5 Improvements of the missing energy trigger

At luminosities expected for the LHC Phase-I running, the large number of pile-up events will generate missing-transverse-energy values similar to those expected for physics processes with missing E_T signatures, like supersymmetric decay chains with a LSP escaping the detector.

The ATLAS trigger system is able to select events with missing energy at trigger Level-1 [4]. This trigger, implemented in hardware, is based on measurements of transverse energy summed up in trigger towers of $\Delta\eta \times \Delta\phi = 0.1 \times 0.1$. The transverse energy sum computed at Level-1 is shown in Figure 2.16, left panel, for ATLAS heavy ion data taken in 2010 [5]. Similar to pp collisions with pile-up, heavy ion events contain a large fraction of particles with a soft energy spectrum. The minimal energy thresholds applied to the Level-1 trigger towers of 1 GeV translate into an overall loss of reconstructed energy by the Level-1 trigger system. This is visible as an increasing energy offset when comparing the transverse energy sum determined by the Level-1 system and using offline event reconstruction. The offset amounts to up to 2 TeV at a $\sum E_T$ value of 14 TeV.

The right panel of Fig. 2.16 shows the $\sum E_T$ spectrum calculated by the EF trigger, which is software based. At this level, information from all calorimeter cells is available and a dedicated calibration at cell level is applied. Comparing to Level-1, a significantly better agreement with the offline calculation is obtained.

These results suggest that higher precision energy measurements at Level-1 will improve the trigger rates of the missing energy trigger in pp collisions at pile-up conditions expected for Phase-I. This can be reached by both a better geometrical granularity and a smaller value for the lowest energy deposit that can be resolved. An overall calibration of the calculated missing transverse

energy will be needed also for the hardware based trigger, but it can be performed in a more refined way with better granularity input.
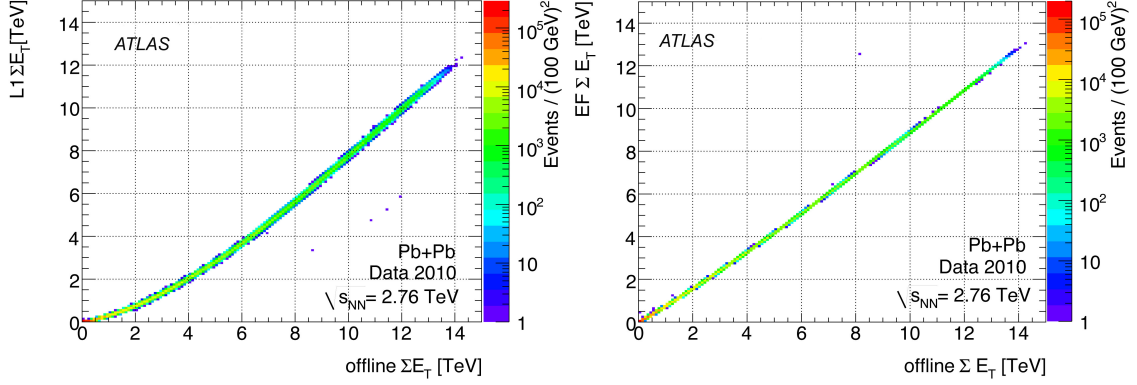
Figure 2.16. The total transverse energy sum, $\sum E_{\mathrm{T}}$, computed at Level-1 (left) and EF trigger level (right) is compared the corresponding quantity calculated offline for events measured by ATLAS during the heavy ion run in 2010.

The proposed calorimeter read-out (see Chapter 4) will provide energy measurements with finer granularity as input to the Level-1 trigger system. Energy deposits are separately provided in four depth layers in the LAr barrel and end-cap calorimeters and a single tower in the Tile calorimeters. The lateral segmentation in η-ϕ is planned to be 0.025×0.1 in the front and middle layer of the LAr calorimeter, and 0.1×0.1 in the presampler and back layer.

With this read-out configuration, the energy thresholds applied for each tower layer can be lowered such that the reconstruction of the missing energy and the total transverse energy sum at Level-1 will be improved. The dynamic energy range required for the read-out will have to be found in an optimization procedure.

Furthermore, refined calibration procedures for the jet and missing energy calculation will be available at hardware trigger level. Hadronic calibration as developed for the EF trigger chains [6] could be applied. The high granularity energies, E_{ij}, of each segment i in sampling j, are linearly combined to intermediate quantities, X_j, per sampling. These are then used to determine the global quantity $X = \sum_j (a_j X_j + b_j)$, where a_j and b_j are calibration constants, and X one of the corresponding variables like $E_{\mathrm{T}}^{\mathrm{miss}}$, $\sum E_{\mathrm{T}}$, $\sum E$. Such linear algorithms are ideal for hardware implementation. The corresponding Level-1 trigger performance is subject of ongoing and detailed studies.

2.4 Performance of present ID tracking

The performance of the present ID tracking up to 100 overlapping events (roughly twice that expected for a luminosity of $2 \times 10^{34} \mathrm{cm}^{-2} \mathrm{s}^{-1}$ and 25 ns beam crossing separation) has been studied extensively using Monte Carlo simulation [7] based on Geant4. The tracking efficiencies of the pixel and SCT layers have been shown, with appropriate cuts, to be stable as a function of pile-up for simulated electron, muon and pion samples. With tracking parameters tuned to give less than 4 % fake rate, the worst case pile-up for Phase-I leads to only 1-2% additional efficiency losses for muons and pions and 3-6% further losses for electrons. Many studies since November 2009 have confirmed the excellent agreement of the tracking simulation with data [8],[9],[10].

In particular, the performance of the present ID tracking up to luminosities of $2 \times 10^{34} \mathrm{cm}^{-2}\mathrm{s}^{-1}$ has been evaluated in simulations carried out for the Insertable B-layer (IBL) Technical Design Report [11]. The Monte Carlo studies for the IBL (Fig. 2.17) show that tracking efficiencies from $t\bar{t}$ events are rather independent of pile-up, all the way to $\mu \sim 50$, giving confidence that the global tracker performance is fairly robust for this range of pile-up values. It is also seen in Fig. 2.18 that, although the TRT occupancies can rise above 30%, the momentum resolution does not degrade dramatically with the pile-up levels expected for Phase-I luminosities. Furthermore, the inner detector read-out should have sufficient capacity to handle the Phase-I occupancy at the maximum 100kHz trigger rate. This assumes there is flexibility to provide further off-detector processing, if needed, by using additional RODs and read-out links.
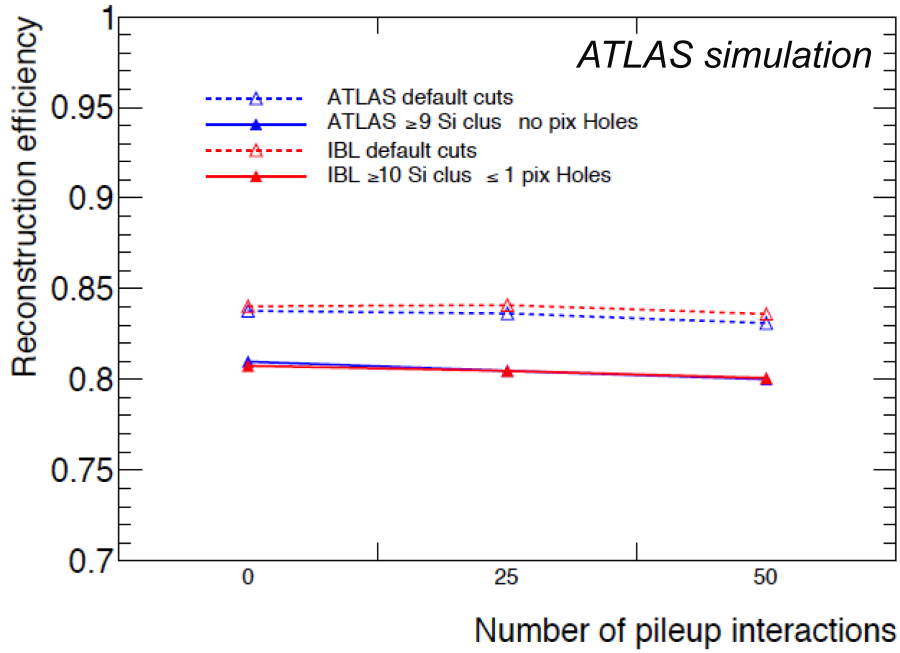
Figure 2.17. IBL TDR studies of efficiencies for reconstructing primary tracks ($p_T > 1$ GeV) with and without IBL in $t\bar{t}$ Events as a function of μ (pile-up)

A recent experimental test of the tracker performance at high occupancies has been provided by the track reconstruction efficiencies found with heavy ion (HI) data. Reference [12] describes the full tracker performance in an environment with up to 4000 tracks per event of $p_T > 500$ MeV.

In HI data, a tracking efficiency independent measure of the 'centrality' of the event is chosen to be the number of pixel B-layer cluster hits, since this is least sensitive to the p_T cut and the occupancy is still sufficiently low such that the effect of hit overlap is expected to be negligible. The centrality can correspondingly be defined by binning events with the hit occupancy of the B-layer and assuming equal numbers of entries for equal ranges of centrality.

The comparisons of data and simulation, for a range of centrality values, in terms of number of hits on tracks in the 3 sub-systems (Pixel, SCT and TRT) and impact parameter distributions, is remarkably good [12]. Even the most central events (0-10%), which correspond to B-layer pixel oc-
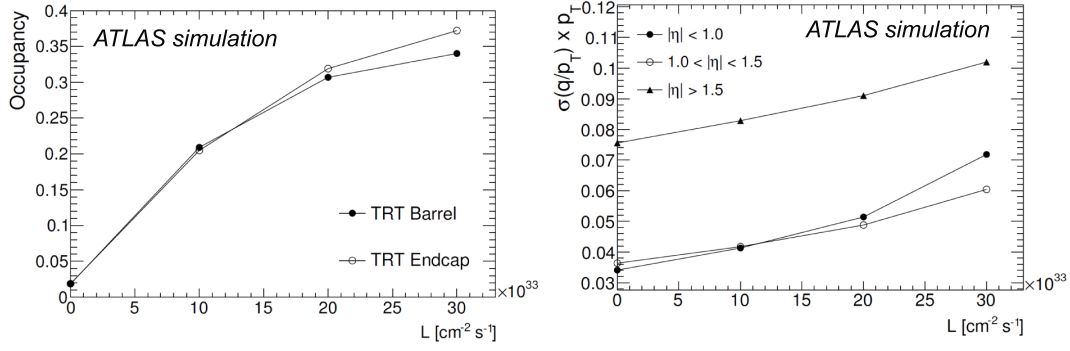
Figure 2.18. IBL TDR studies of TRT occupancies and the impact on momentum resolution for single 100 GeV muons as a function of instantaneous luminosity.

cupancies above 2×10^{-4}, are well modelled in all three detector systems. At these extreme values, the TRT is still seen to be contributing to the tracking (albeit with some reduced efficiency) even though 30% or more of the TRT tubes are hit. For centrality values up to 20%, the p_T resolution can still benefit by an 8-16% improvement by including the TRT information[13].
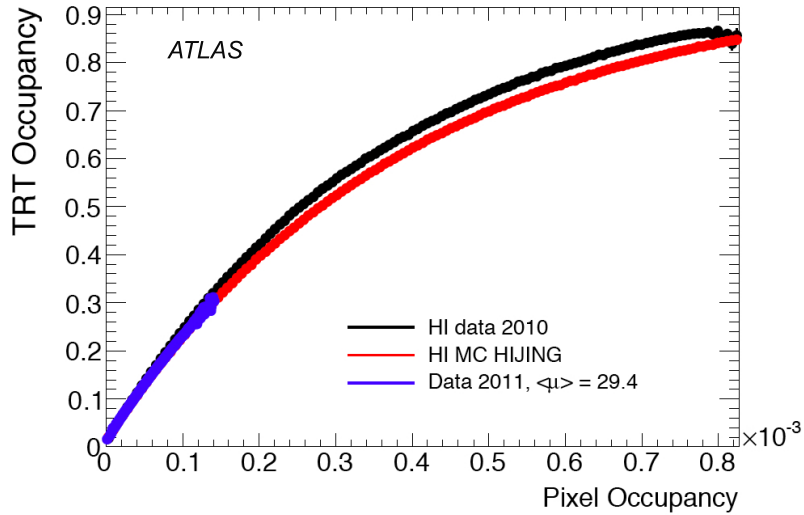
Figure 2.19. TRT Occupancy as a Function of the B-Layer Pixel Occupancy. This shows for heavy ion data (in black) and Monte Carlo (in red) TRT occupancies against those in the pixel B-Layer which is a measure of the "centrality" in the case of heavy ion data. At high TRT occupancy the relation between the two is no longer linear because of the increasingly higher probability for two hits to overlap in the TRT. The blue data show the results from dedicated LHC running (very sparse "fat bunches" to deliver high pile-up events to the experiments) at 3.5 TeV on 3.5 TeV in 2011 data (run 00190728).

Figure 2.19 confirms that 30% TRT occupancy is anticipated at $2\times10^{34}\mathrm{cm}^{-2}\mathrm{s}^{-1}$ and 25 ns beam crossing spacing ($\mu \sim 55$) since these conditions correspond to pixel occupancies around 2×10^{-4} (extrapolating from current data). The "fat bunches" running, heavy ion data and heavy ion Monte Carlo all coincide with the proton-proton Monte Carlo results discussed above, giving confidence in the Monte Carlo predictions for the TRT occupancies. 30% occupancies result in

roughly 10^5 TRT drift circles per event. Figure 2.20 then shows that, in this range, the number of hits per reconstructed track in the TRT is relatively stable, again confirming that TRT performance should not degrade significantly for conditions corresponding to Phase-I operation.
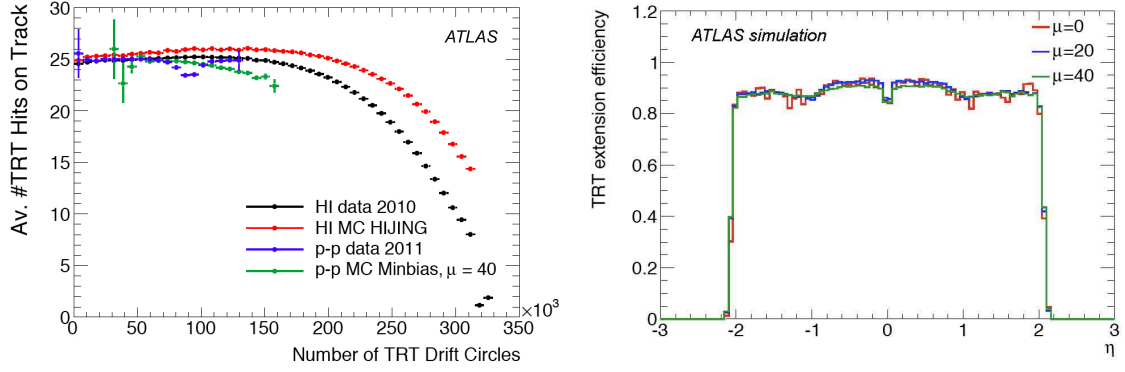
Figure 2.20. (Left) Average number of TRT hits on tracks as a function of the number of TRT drift circles.(Right) Efficiency of tracks from the SCT being associated with track segments in the TRT for different pile-up values over the full tracker acceptance. Note that the proton data here is for standard 2011 running conditions.

3. Upgrades of the Muon System

3.1 Introduction

The Phase-I upgrade of the muon spectrometer [14] focuses on the muon inner station (EI) of the muon end-cap. The small wheel is located between the end-cap calorimeter and the end-cap toroid. This is the region of the highest cavern background flux in the muon spectrometer. Cavern background is mainly due to low energy photons and neutrons. They normally cause random hits leading to high occupancy in the detectors. There is also a contribution from charged particles of various energies. They cause, when they penetrate the layers of the detector, aligned hits across the layers producing track segments in EI.

3.1.1 The goal of the small wheel upgrade

Based on the observations discussed in Chapter 2, one concludes that new small wheels should be designed and built to replace the existing ones, as part of the ATLAS Phase-I upgrade. This will allow ATLAS to be able to fully benefit from instantaneous luminosities beyond the nominal value and therefore significantly improve the physics performance of the experiment. The two main elements of the upgrade are:

- Precision tracker with performances at high luminosity as good as that of the present tracker at lower luminosity.

- A new function performing real time segment reconstruction at every bunch crossing and providing track positions and angular resolution of better than 1 mrad to be used by the Level-1 trigger. The trigger data of the small wheel should arrive at the electronics for building the end-cap trigger (the sector logic) not later than the arrival time of the main trigger data from the EM station. The maximum delay is 1.08 μsec or 43 clocks from the beam-beam collision time.

Since the new small wheel should be operated throughout the Phase-I and Phase-II periods, the detector and associated electronics have to be designed for the operation at the Phase-II luminosity of $5 \times 10^{34} \text{cm}^{-2}\text{s}^{-1}$. This means that the detector should maintain sufficient performance under the condition of background hits rates of $\sim$14 kHz/cm^2 (including a safety factor) down to the smallest radius of the acceptance (R=100 cm). During the running period after Phase-I, a total integrated luminosity of about 3000 fb^{-1} will be collected. The small wheel detector and associated electronics and services are therefore required to withstand the corresponding integrated radiation dose, as well as the instantaneous rate. For the detector at the smallest radii, this corresponds to an accumulated charge of order 1 C/cm^2 under the assumption of background rates as discussed above.

3.2 New small wheel scenario

The basic layout of the new small wheel should be the same as the present one (Fig. 2.1). The detector will be segmented in 16 azimuthal sectors. They are arranged in a alternating large-small sector layout in order to match the geometry of the rest of the muon spectrometer. This is important for track reconstruction and precise momentum determination.

With regard to the mechanical structure and detector layout, the new small wheel has to be designed with the constraint of integration inside the existing muon spectrometer. The position and dimensions of the detector will be similar to the present small wheel. Most of the existing radiation shielding structures will be reused; they include the JD disk and the plug shielding [15]. The support structure - the wheel - will have a new design, matched to the new detectors and incorporating improved accessibility to the detector components.

As in the present small wheel, an optical alignment device should be integrated as a part of the end-cap optical alignment system. In addition there must be a mechanism for providing internal alignment within each chamber module. This is particularly important for the detector construction where significant deformations are expected.

3.2.1 Interface to the trigger and DAQ system

The trigger data (list of track vectors) from the small wheels are sent to the sector logic in USA15 where they are combined with the main trigger data from the EM (big wheel) TGCs to generate a list of muon candidates with their p_T and RoI address, which are then used in the central trigger processor for generating the final Level-1 triggers. New sector logic boards will be built incorporating the new functions of removing fake triggers using the small wheel information and possibly making an improvement of the p_T resolution. All these processes will be performed without adding extra latency apart from a few additional clocks cycles needed inside the new sector logic for more complex processing compared to the present system. Further details are discussed in the TDAQ upgrade Chapter 7.

In the Phase-II upgrade on the other hand, significant changes of Level-1 trigger are anticipated, resulting in a longer Level-1 latency, higher Level-1 rate, or more complex Level-0/Level-1 arrangements (all these being under consideration). Details have to be further clarified in the future. The priority of the new small wheel design is on the Phase-I upgrade, however care should be taken to allow operation after the Phase-II upgrade with limited and modest changes to the system.

The DAQ system should be integrated in the current ATLAS TDAQ system and, at the same time, be able to support anticipated trigger rate and data throughput for Phase-II. The connectivity should be designed, in particular, to allow easy changes of an input or output interface according to the evolution of the global ATLAS standard. The design should also include the distribution of the data between read-out systems, to allow optimised communication with the Higher Level Trigger.

3.2.2 Integration and detector technologies

The detector will be assembled and fully tested before installation. The complete small wheel will be built on the surface well in advance of the installation time in ATLAS, allowing sufficient time for commissioning of the system, including the associated electronics.

In order to satisfy the requirements for the new small wheel, three detector concepts have been proposed. Extensive R&D has been carried out on all three options and each alternative has been shown to be very promising.

The next step is to define the new small wheel project with a single baseline technology to be chosen by early 2012. The three current options are discussed in the following sections.

3.2.3 Option A : small tubes MDTs and tracking TGCs

In this design, the detector module is a combination of small drift tube (sMDT) chambers for precision tracking and fast trigger chambers (sTGCs) that provide as well a second coordinate. This layout is common to the general concept of the present muon spectrometer. Both detectors (sMDT and sTGC) are based on existing and proven technologies currently used in the muon spectrometer (MDT and TGC), but with enhanced performance to match the requirements for the new small wheels.

- sMDT is made from tubes of half the diameter of the present MDT tubes, otherwise operating under the same conditions with respect to gas gain, gas composition and pressure [16]. The reduction of the tube diameter from 30 mm to 15 mm leads to an increase of the rate capability of the tubes by a factor 7, sufficient to cope with the level of background at high luminosity. This high rate capability is a combined result of smaller tube size (1/2) and shorter drift time (1/3.5)

- sTGC is a new type of TGC trigger chamber providing considerably improved spatial resolution in the bending plane, while preserving the basic mechanical structure together with the operating parameters of the proven TGC system (as presently used in the muon end-cap). An important change compared to the existing TGC is a reduced cathode resistivity of 100 $k\Omega/\square$, with which the rate capability has been increased substantially up to 30 kHz/cm^2. In the sTGC chambers, unlike the present TGC chambers, the wires are running along the radial direction. The bending coordinates are measured by strips of 3.5 mm pitch which are located behind the resistive cathode plane. The distribution of the induced charges on the strips is used to obtain the precision coordinate with an accuracy of < 100 μm. The other cathode planes of the sTGC are used for pad read-out. The coincidence of pad signals across stacked sTGC layers is used for selecting a RoI in which the strip information is processed by fast electronics to obtain precision segment coordinates for the Level-1 trigger.

Figure 3.1 shows a result of high rate test performed at the GIF facility using a full size prototype of sMDT chamber, in comparison with the performance of a standard 30 mm tube. While the segment efficiency starts to degrade at 200-300 kHz per tube for the standard MDT chamber (30 mm tubes), the sMDT chamber (15 mm tubes) maintains its efficiency beyond 1000 kHz/tube which is the expected rate at L=5×10^{34}cm^{-2}s^{-1} for 50 cm long tubes located at the smallest radii.

Large size sTGC chambers were built and tested with various conditions including high intensity γ rays and neutron flux. Combined beam tests with the sMDT chamber have also been performed and data analyses are in progress. Preliminary measurements on the position resolution, obtained by using a Time over Threshold method to find the centroid of induced charges on the strips, show better than 100 μm resolution. Good timing resolution was observed for coincidence of pad signals from four layers, proving that this method can be used for bunch identification. Furthermore, irradiation tests performed on small chambers demonstrated that a total charge per wire of 6 C/cm can be accumulated without any visible deterioration of the performance.

Like the present small wheel, each sector consists of three chamber units of trapezoidal shape. The structure of a typical chamber unit is shown in Figure 3.2. The sMDT structure consisting of two multi-layers (4 or 6 tubes each) sandwiched by two units of sTGC chambers, one in front and
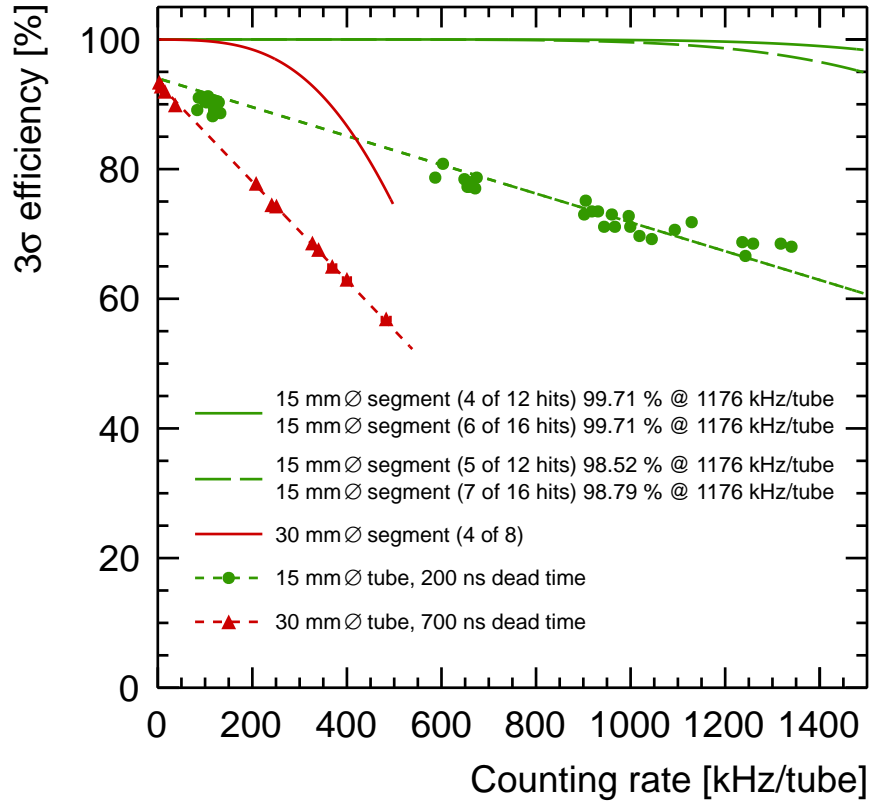
Figure 3.1. Tube efficiency, for hits within 3σ with respect to the expected track position, as a function of the tube hit rate. The red points are for the existing 30 mm tube while the green points are 15 mm tube. The red and green curves show corresponding segment reconstruction efficiency calculated using the single tube efficiency and requiring a minimum number of valid hits on the track as indicated in the figure.

the other behind of the sMDT unit. Each sTGC unit contains 4 layers of gas gaps. In total there are 8 or 12 samplings of charged particle tracks by sMDTs. In addition, sTGCs also provide 8 position measurements of the track with similar position resolution as the sMDTs. This layout allows up to 16 potential measurement points or 20 at small radii, ensuring efficient and robust reconstruction of track segments, with high precision in high background conditions. With a distance of about 30 cm between the sTGC packages, an angular resolution of < 0.4 mrad has been achieved, which allows the efficient removal of tracks not pointing to the primary vertex in the Level-1 trigger decision.

3.2.3.1 Read-out and trigger electronics   The read-out of the sMDT tubes will follow the proven architecture of the present MDT system. A number of additions and modifications will however be necessary in order to adapt the rate capability of the read-out chain to the requirements of the high luminosity LHC. For the mechanical integration of the read-out electronics with sMDT, the layout of the electronics will have to be adapted to the four times higher tube density at the ends of the chambers. The radiation tolerance of all components will have to comply with the high radiation levels, in particular at the inner border of the small wheel.
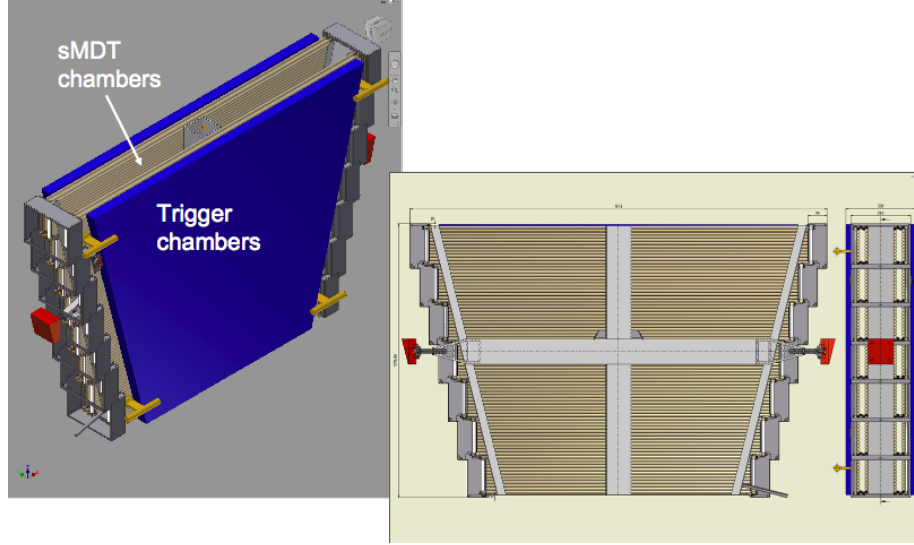
Figure 3.2. Left: A chamber unit with two sTGC chambers attached to a sMDT chamber. The distance between the TGC packages is about 30 cm. Right: Structure of a sMDT unit.

Given the high rate capability of the sMDT tubes, the bandwidth of the read-out system has to be increased. Due to the limitations of the internal buffering scheme and processing speed, the present TDC can only handle average tube rate of up to about 300 kHz/tube, while the sMDT tubes would run up to 1000 kHz. An improved TDC is therefore an essential requirement for the new system. Another limitation in the present system comes from the optical link connecting the CSM to the ROD, which only provides a usable bandwidth of 1.4 Gbit/s. The following new components are considered for the new system.

- The ASD is re-designed in 130 nm technology. A 4-channel prototype has already been produced and works correctly.

- The TDC will be replaced by the HPTDC, designed by the CERN-MIC group. This 32-channel device has an improved internal buffering as well as higher transfer and processing speed.

- The CSM collects data from a MDT chamber, formats the data and sends data, on receipt of Level-1 accept, via an optical link to the ROD in USA15. This unit will need to be updated to higher radiation tolerance.

- The link connecting the CSM to the ROD will be replaced by a GigaBit transmitter link (GBT) developed by CERN. This link provides a 3 times higher transfer rate compared to the presently used GOL serialiser.

The strip signals in the sTGC are used to reconstruct track segments in the small wheel with good angular resolution. In the two sTGC units, a local trigger is made from two sets of 3 out of 4 coincidence of pads from 4 layers each. The triggering pad tower selects the strips in its region for transmission to 8 centroid finders, one for each layer. This selection leads to a 20 fold

reduction in the number of strips to be processed as well as in the number of centroid finders. The four centroids in each sTGC package are averaged to define a vector track segment in the small wheel. The spatial resolution (<100 μm) together with the separation distance of 300 mm provides an angular resolution of better than 0.4 mrad; thus satisfying the requirement for the new Level-1 trigger function. A demonstrator has been implemented using commercial components to verify the functionality, in particular the resulting latency of the trigger logic.

The baseline for the front-end chip is to use the VMM front-end chip, now under development (see Section 3.2.5), including both ASD and read-out logic. The first prototype chip will be available in early 2012. The sTGC version of this ASD has LVDS output suitable for the trigger logic using Time over Threshold.

3.2.4 Option-B : small tubes MDTs and new trigger RPCs

Like the sMDT + sTGC layout, this concept follows the same principle of combining dedicated detectors for precision tracking and triggering, but adopting RPC technology for the trigger detector. The general layout is therefore the same as that of the sMDT+sTGC layout discussed in the previous section, each detector unit is made from a sMDT chamber sandwiched by two RPC chambers.

The choice of the RPC technology as trigger detector for the new small wheel is motivated by its excellent timing resolution, which is effective to reject low energy uncorrelated background hits in a hostile operating environment. Additional advantages of the RPC technology include: the simplicity of its structure, the relatively low cost construction, the possibility of being tailored to any shape and the small amount of space it occupies. In addition, a full MDT-RPC integration with DAQ was successfully tested. It is based on the same mezzanine cards and CSM circuits as developed for the sMDT, simplifying the DAQ system through the use of a uniform technology.

The RPC technology is used for the trigger chambers in the ATLAS barrel muon system. The present RPC is based on a 2 mm gap between two resistive plates of 2 mm thick, made of melamine coated phenolic laminate. The gas volume is sandwiched between two read-out panels with mutually orthogonal strips giving a point in the space for each avalanche generated in the gas volume. The RPC chamber for the small wheel upgrade is conceptually similar to the present barrel RPC, with a number of upgrades required for the much more difficult operating condition in terms of particle rate compared to the barrel.

- The single 2 mm gap is split into two 1 mm gaps leading to a better time resolution. Lower individual gains, possible due to the newly developed FE electronics, allow for an increase in the rate capability. A higher efficiency is possible due to the two gaps inducing simultaneous signals on the same strips. This structure, multi-gap RPC (mRPC), is the basis of the proposed layout.

- Recent development of a new low noise amplifier allows a substantial increase in the rate capability by allowing the mRPC signal detection with a factor 10 less charge delivered in the gas with respect to the present RPCs.

The baseline of the trigger chamber layout is a triplet of 1+1 mm bi-gap mRPCs (Figure 3.3). The trigger logic requires the 2 out of 3 coincidence within the same triplet, thus strongly reducing the

contribution from uncorrelated background hits, followed by the two fold coincidence of the two triplet signals for defining the track segment and determination of its vector.
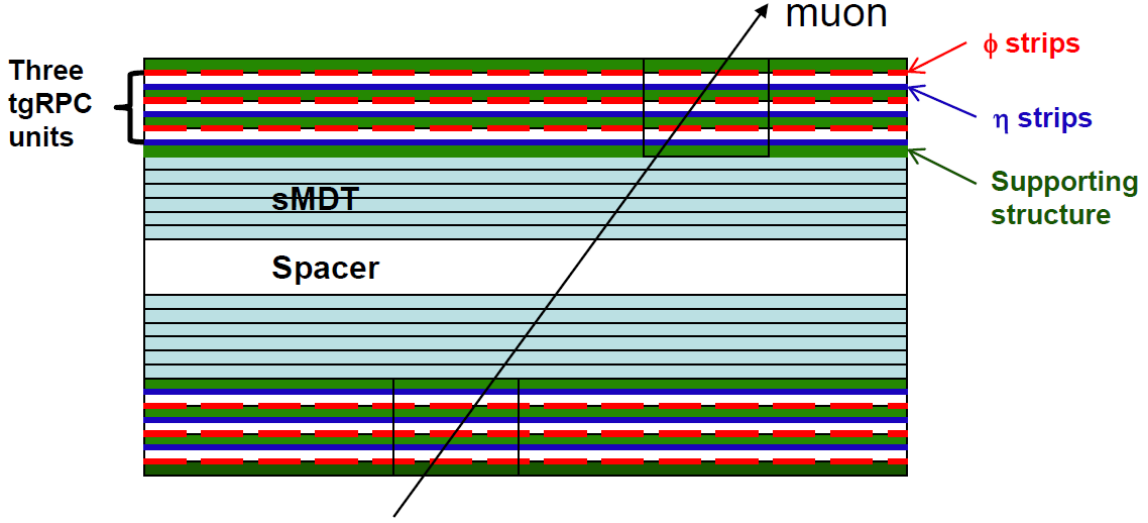
Figure 3.3. Layout of the mRPC chamber with three units on both sides of the sMDT chamber, where each gap represents a double gap. Each mRPC unit is read-out along both η and ϕ directions.

The layout of the mRPC detector will follow the layout of the sMDT chambers with large and small sectors. The mRPC chambers, consisting of 3 bi-gaps, will be mounted on both sides of the sMDT chambers with read-out strip position referenced to the sMDT tubes for internal alignment. In total there will be six types of mRPC chambers with different size, three for large sectors and three for small sectors. There are 96 chambers in total for each wheel. With an η strip pitch of 2 mm and read-out from both ends, the total number of read-out channels is 230 k for each wheel.

3.2.4.1 Read-out and trigger electronics Each gap is read out by orthogonal strip planes. The strip pitch is 1-2 cm in the ϕ coordinate, while the bending η coordinate is segmented in steps of 2 mm pitch. All the strips are equipped locally with the low noise front-end amplifiers. The strips are read out in groups of 8 by a specially developed circuit, the Maximum selector, allowing extraction of the strip or neighbouring strips with the maximum induced charge. A fast mean-timer circuit has also been developed with a resolution of 250 ps. It processes the signal coming from both ends of a η strip allowing prompt location of the particle impact in a very narrow space-time window of $\Delta\eta \times \Delta\phi \times \Delta t = 1\text{cm} \times 5\text{cm} \times 2$ ns.

In this configuration, position resolution per layer in ϕ and η coordinates are 3 mm and 0.3 mm, respectively. Given the lever arm of about 40 cm this would imply the angular resolution in η of less than 1 mrad as required for the Level-1 trigger upgrade.

3.2.5 Option-C : Micromegas

In contrast to the other proposals discussed above, the Micromegas design is based on a single detector technology. It combines trigger and precision tracking using the same detectors.

Micromegas is a micro-pattern gas detector with excellent high rate capability and good performance in terms of efficiency, spatial and time resolution; all strong points for its application in the new small wheels.

A micromegas detector consists of a planar drift electrode, a gas gap of a few mm thickness acting as ionization and drift region, and a thin metallic mesh at, typically, 100 μm distance from the read-out electrode, creating the gas amplification region [17]. A sketch of the micromegas operating principle is shown in Fig. 3.4. The HV potentials are chosen such that the electric field in the
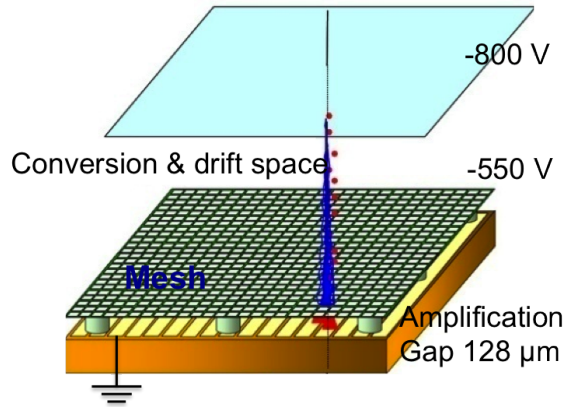
Figure 3.4. Sketch of the layout and operating principle of a micromegas detector.

drift region is a few hundred V/cm and in the amplification region is of the order of 40-50 kV/cm . Charged particles traversing the drift space ionize the gas, the ionization electrons drift towards the mesh. The mesh is transparent to most of the electrons as long as the electric field in the amplification region is sufficiently higher than the drift field. The electron avalanche takes place in the thin amplification region immediately above the read-out electrode. The micromegas technology takes advantage of the fast evacuation ($\sim$ 100 ns) of positive ions through the amplification mesh and therefore allows operation at very high particle fluxes. Reasonably high gas amplification, typically 10^4, can be achieved. Due to the very small size of charge foot-print on the read-out electrode (comparable to the gap size), a good position resolution is obtained, given a fine segmentation of the read-out electrode.

Micromegas detectors have been successfully used in particle physics in the past years when good spatial resolution at high rate were required. Micromegas were also successfully used as read-out devices for Time Projection Chambers. For the application in the new small wheels, there were, however, two issues to be overcome.

- The size of the small wheel detectors are typically 1m×1m. Micromegas of this size had never been built in the past.

- Due to very thin amplification gap, micromegas is vulnerable to sparking. Sparks occur when the total number of electrons in the avalanche reaches a few 10^7 (Raether limit). High detection efficiency for minimum ionizing muons requires gas gain of 10^4. Ionization processes producing more than 1000 electrons over distances compatible to the typical lateral extent

of an avalanche (a few 100 μm) might risk sparks. Such ionization levels are easily reached by slowly moving charged debris from neutron (or other) interactions in the detector gas or detector materials.

Through R&D studies in recent years, both of these problems are being solved.

The approach to the first problem is the use of 'bulk' micromegas technology [18]. It employs industrial processes used in printed circuit board technology to place the mesh at a fixed distance above the read-out electrode, allowing the production of precision structures with the required size at an affordable cost.

The spark problem is solved by adding a layer of resistive strips on top of a thin insulator directly above the read-out strip [19]. With this protection, the detector can be operated at higher gas gain and reduce the spark currents by about three orders of magnitude. In such a scheme, the charge created in the amplification region is not directly seen by the read-out electrode, instead the signals are capacitively coupled.

Detectors with resistive strip have been extensively tested in hadron and neutron beams up to rates far exceeding the expected rates in ATLAS. A large number of detectors have been exposed to 8 keV X-rays up to rates of several MHz/cm^2. Since the beginning of 2011, four small chambers are successfully operating in the ATLAS cavern and produce clean data. The largest detectors that have been constructed so far using this technology have the dimension and the shape of an ATLAS CSC chamber. The size is currently limited by the present size of the PCB facility at CERN, the active part of this chamber is 0.6×1.2 m^2 and covers half of the CSC surface. This chamber has been successfully exposed to the H6 hadron beam at CERN.

The read-out electrode can be segmented almost arbitrarily. The structure with overlaid strip layers of different directions was successfully tested with up to three read-out coordinates from a single gap, allowing for two orthogonal strip arrangement, x, u, v read-out arrangements or any other two-dimensional read-out pattern. Pad read-out can also be implemented.

The thickness of the drift gap will be about 5 mm leading to a maximum electron drift time of 100 ns. Muons from the IP enter the micromegas with angles ranging from 8° to 30° with respect to the normal incidence. This means that electrons spread over the distance of 1-2 mm on the mesh plane along the projected track. If all these charges are integrated, the fluctuations of the primary clusters will lead to a poor position resolution of the charge centroid. In order to achieve a good position resolution for such inclined tracks, the micromegas will be operated in a 'micro-TPC' mode in which the drift times of each electron arriving at different strips are measured and the track is reconstructed in 3-D over the drift gap with a good position and an angular resolution of a few degrees.

The layout of the chambers in the small wheel follows closely the current scheme, with large and small chambers and the same azimuthal overlap. However the radial segmentation will likely be four chambers per sector instead of three, limiting the radial extent of the chambers to less than 1 m and therefore stay within the dimensions of standard PCBs (see Fig. 3.5). With the radial segmentation in Fig. 3.5 there are in total 128 chambers. Each chamber has eight detection layers, grouped into two multi-layers separated by a support structure. This layout requires the construction of eight different chamber types, four each for large and small sectors.
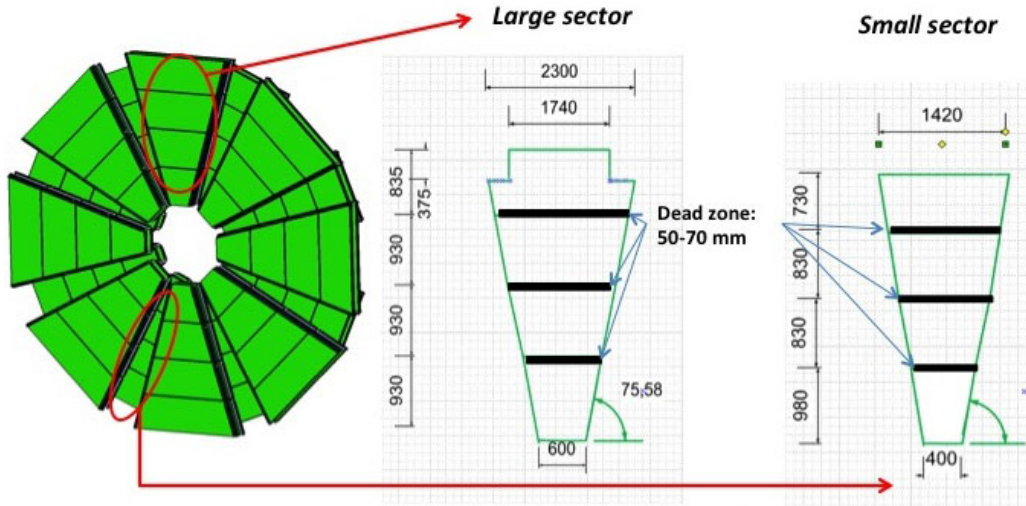
Figure 3.5. Micromegas chambers arranged in the large-small layout. Each sector is divided in 4 units.

The number of read-out channels is a parameter that depends on the final segmentation of the read-out electrodes and should be optimised according to the physics needs. The required spatial resolution in the bending plane can be achieved with a strip pitch between 0.5 and 1 mm. For the non-bending plane a strip pitch of several mm would be sufficient for a second coordinate resolution of a few mm. There is also a possibility of adding a pad read-out to help pattern reconstruction by resolving combinatorial background from multiple hits. Such a pad read-out could either replace some of the second coordinate read-outs, or it could be an additional third read-out layer of a single micromegas. In a preliminary arrangement of readout electrodes, the total number of readout channels is about 2 million for two wheels.

3.2.5.1 Read-out and trigger electronics   The function of the read-out electronics system is two-fold.

- Provide in real time a high resolution vector to be used in the formation of the muon Level-1 trigger.

- On the reception of a Level-1 accept, provide hit information of strips (charge and time) for precision tracking in the offline reconstruction.

The read-out and trigger system is required to handle a total of 2 million channels in the micromegas detector. The first function will be implemented with a data driven system that performs on-detector zero-suppression. For the trigger function, the design takes advantage of the micromegas with read-out strips of small pitch (order of 0.5 mm) to realise a trigger system with a factor of 64 fewer channels. This is achieved by considering only the first arriving hit in each 64-channel front-end chip at a given bunch crossing, resulting in a system that has effectively 3.2 cm granularity but providing spatial resolution better than half a millimeter. This greatly simplifies the task by reducing the number of channels by almost two orders of magnitude while not requiring any processing of

the raw signals to determine the hit coordinate with the precision required for a 1 mrad resolution in determining the angle of track segments.

A custom front-end ASIC is being developed based on the design used successfully for the read-out of a GEM based TPC [20]. A chip will contain 64 channels. It will provide the specific functions for the micromegas based new small wheels. At the same time, it is general enough to be used by any type of detector using charge interpolation to determine the precision coordinate such as sTGC or mRPC.

The micromegas, operating in the micro-TPC mode, require both charge and time measurements, the latter with a precision of about 2 ns. The ASIC provides the peak amplitude and time with respect to the bunch crossing clock in a data driven mode. They are stored in a de-randomizing buffer and read-out serially with a smart token passing scheme that only reads out the amplitude, timing and address of the channels with information.

Using the address of channel with the earliest signal, the trigger system will work as follows. At every bunch crossing, the 64 channel front-end ASIC outputs the 6-bit address of the channel with the first detected amplitude above a threshold. The loss of efficiency due to this simplification is insignificant. Even in a worst case scenario at the highest rate region, the probability of accidentally having another hit in a strip preceding a signal hit is at a level of 1%. On the detector there are four front-end cards, each carrying 8 front-end ASIC. The address of the first hit per chip is sampled at each bunch crossing and sent out to a trigger logic by Gigabit transceiver (GBTX). At the receiving end of the link, a system based on Content Addressable Memories is used to determine the segment parameters at high speed sufficient to satisfy the latency requirement on the Level-1 trigger function.

On receipt of a Level-1 accept, the already sparsified and digitised data in the buffer of the front-end chips are read out serially using the same GBTX link and routed to read-out drivers (ROD).

3.3 Timetable

In view of the scale and complexity of the new small wheel, it is planned to assemble the complete small wheels on the surface and to perform a thorough commissioning before installation. With the understanding that the installation of the new detector in ATLAS will be in 2018, the assembly of the small wheels needs to be completed in 2017. Counting the necessary years for production of the final detectors and the new large-scale electronics systems, including the development time required for iterating the designs, the project will need to start in early 2012 with a single baseline concept.

3.4 Summary and conclusions

Given the LHC luminosity upgrade plans and the expected physics requirements, the installation of the new small wheels during the long shutdown in 2018 is a vital step for ATLAS. It will allow ATLAS to maintain its good muon tracking performance, which otherwise would be seriously compromised without the proposed upgrade. It will also improve the Level-1 trigger performance in the end-cap region to control the trigger rate at high luminosity, without raising the p_T threshold for inclusive muons. R&D activities in the past years have yielded several promising technologies to achieve this goal, with the baseline to be selected in early 2012.

4. Upgrades of the Calorimeter System

4.1 Introduction

Higher transverse granularity and depth information is required by the Level-1 trigger system to reduce the rates and improve resolution for several trigger objects as shown in Section 2. Rejection factors of about 3-5 for low p_T jets faking electrons can be achieved by implementing shower shape algorithms using the 2nd sampling layer of the EM calorimeters. Furthermore, studies of discriminant variables using the 3rd sampling layer of the EM and the hadronic TileCal layers are in progress and could potentially lead to substantial improvements of the resolution of τs, jets and more importantly, missing E_T (MET) triggers.

This additional information will require a partial upgrade of the calorimeter front-end read-out architecture, part of the input stage of the Level-1 calorimeter trigger and the interfaces among the two systems. The upgrade plan for Phase-I is part of a more general staged program to be implemented over the next decade for the entire HL-LHC lifetime: the ultimate goal is a free-running digital architecture of all individual LAr and Tile calorimeter channels.

The proposed architecture will be validated by an in-beam system test planned for installation in ATLAS during the Phase-0 shutdown. The system will be run seamlessly within ATLAS during the pre-Phase-I data taking. It is aimed at improving the granularity in one $\Delta\eta \times \Delta\phi = 0.4 \times 0.4$ slice of the LAr and Tile barrel calorimeters, matching the size of the current L1Calo electron algorithm window. Two trigger Tower Builder Boards and four new Tile drawers (first one drawer and then, if successful, 3 more) with digitization of data at the front-end will be installed in order to test the digital trigger path and hardware implementations of novel single-object triggers.

For Phase-I, an intermediate stage is proposed. It combines analog and digital trigger read-out, fully compatible with the present analog transmission of the trigger primitives but with a digital read-out path that contains many of the elements required by the final upgrade. For the LAr calorimeters, this will be implemented by means of new Tower Builder Boards (sTBBs) that are modified by adding a digital read-out path (Sections 4.3.1- 4.3.4). This provides the trigger with finer granularity data in depth and in η. This architecture represents the most developed option so far by the calorimeter and calorimeter trigger community and serves as baseline design for this Letter of Intent. Alternative designs (e.g. a fully digital trigger read-out) are also being considered and will be fully evaluated in the next phase of the development: benefits, challenges, risk and cost analysis will be part of a global optimization process of the calorimeters and of its Level-1 trigger system in preparation for a Technical Design Report (Section 4.3.6).

The full digital read-out of the Tile calorimeter is planned for Phase-II. For Phase-I, an upgrade based on using the "D-cell outputs" (the outermost layer of TileCal) that are already available in USA-15 is being considered, if it can be motivated by simulations results.

4.2 Overview of the existing read-out system and interface to the Level-1 trigger

4.2.1 Liquid Argon calorimeters

The current LAr read-out architecture is depicted in Fig. 4.1. Because of the stringent performance requirements, the front-end electronics are mounted directly on the cryostats, both in the gap be-

tween the barrel and end-cap calorimeters and on the outer face of the end-cap cryostats [21]- [22].
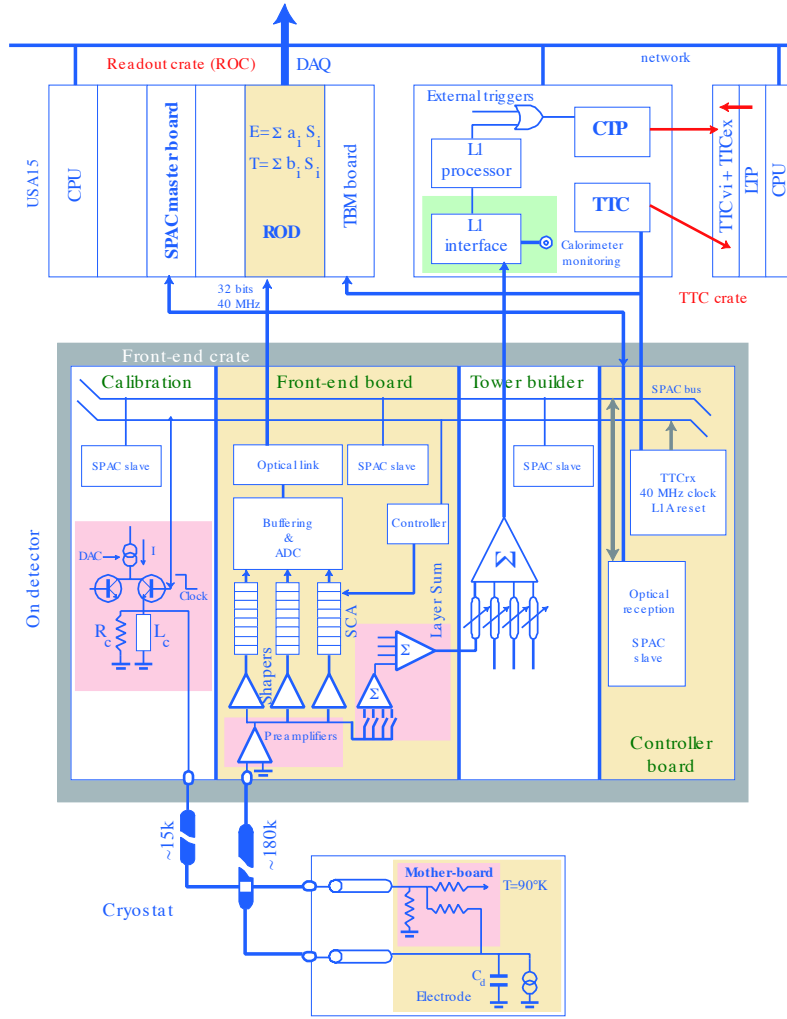
Figure 4.1. Block diagram of the current front-end read-out architecture.

The front-end boards (FEB) sample the calorimeter signals (128 channels per board) at approximately 40 MHz, hold the samples in an analog Level-1 pipeline, and after digitization, send five digitized samples off-detector for each detector cell at each Level-1 accept.

The tower builder boards sum the analog signals from multiple calorimeter cells into towers for the Level-1 calorimeter trigger, and are connected by long differential signal cables to the receiver modules in USA15. These are connected further to the Level-1 system which digitizes and processes the tower energies.

Calibration boards allow injection of known signals into the calorimeter for calibrations, and controller boards are used to configure and control the boards, as well as distribute clock signals. The components used in these boards, including more than ten ASICs, have all been qualified in terms of radiation tolerance for a total integrated luminosity of 700 fb^{-1}.

In USA-15 Read-out Driver modules (ROD) convert the raw data samples sent by the FEBs to

reconstructed energy and signal time. The results are merged with the Level-1 trigger information and sent to the read-out Buffers and the DAQ system [23].

4.2.2 Tile calorimeters

All of the on-detector electronics, apart from the low voltage power supplies are kept in replaceable "drawers" coupled in super-drawers (see Fig. 4.2).

The major design considerations for the on-detector electronics has been radiation tolerance, reliability, redundancy, minimization of noise and dynamic range. The major part has performed satisfactory but there are some areas that need improvement.

Inside the drawers PMT signals are grouped and summed into 0.1×0.1 trigger towers to form analog trigger signals, which are transferred via trigger cables to the Level-1 calorimeter trigger in USA15. The PMT signals are also amplified along two paths, high and low gain (gain ratio 64), inside the 3-in-1 front-end boards. These are then digitized in digitizer boards (2x10 bits) and stored locally in pipeline memories. Events selected by the Level-1 trigger are transferred from the pipeline into de-randomizer memories and sent via the interface board and optical fibers to the off-detector RODs. A synchronized clock, trigger decisions and commands (TTC) are sent in the other direction. The dynamic range achieved is close to 16 bits, but the precision is limited to a level compatible with the overall precision requirement.

The current power supply system distributes bulk DC high voltage (200V DC) from USA15 down to the detector, where it is converted to eight different voltages that are used in the drawer electronics by means of DC-DC converters. These supplies service the 3-in-1 cards, mother boards, digitizer and also the high-voltage control electronics. The high voltage part consists of: the PMT dividers; the individual HV regulation close to the PMTs and finally the HV supplies in the counting room that deliver one HV source voltage per super-drawer. Apart from this, the regulation cards support probes providing temperature information from several parts of the super-drawers.
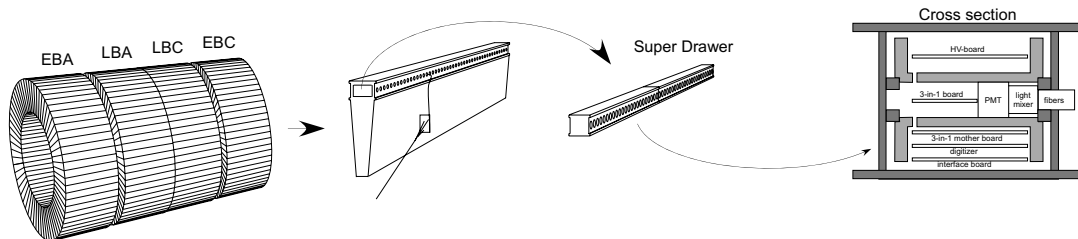
Figure 4.2. Present TileCal structure

The RODs receive events at an averaged Level-1 rate, which are analyzed with respect to Energy, Phase and Quality Factor using Optimal Filtering algorithms. These are implemented in Digital Signal Processors.

In addition to calibration directly from the data, three independent calibration systems are incorporated into the Tile calorimeter electronics and system design to aid in calibrating the detector. These systems are critical to the calibration of the system and to monitoring the status of the detector elements.

The linearity, gain and stability of the front-end electronics are monitored by the 3-in-1 charge injection system. As a permanent part of each front-end electronics channel, it is used to determine

the relative calibration of each channel and to map its response over the full dynamic range of input signals. Two precision capacitors that are part of the input shaping network are connected to ground through fast switches. The switch closing is synchronized with the LHC bunch crossing and its relative phase can be adjusted in steps of 100ps.

A ^{137}Cs monitoring system is used to calibrate and monitor the TileCal subsections. Three powerful (10 mC) ^{137}Cs γ sources embedded in metal capsules are carried by liquid flow inside calibration tubes passing all the calorimeter cells. When a cell is traversed by a source, photons with the energy $E_\gamma = 0.662$MeV induce light emission in the scintillating tiles that allow a measurement of the optical quality of the tiles and fibers. The currents are read out at a fixed frequency (90 Hz) via integrator circuits in the 3-in-1 modules and via the ROD modules.

The PMT performance and the fast read-out chain are also monitored using fast laser light pulses transported to the photocathode of each PMT by dedicated clear, plastic optical fibers. The shape of the laser signal is very similar to that of the scintillating light, and its amplitude covers the whole dynamic range up to the saturation level of the PMTs. The laser itself is monitored by 4 photodiodes and 2 PMTs, where the photodiodes control the amplitude and the PMTs measure timing and allow sending the laser light in empty LHC bunch crossings.

4.3 Proposed upgrade of the Liquid Argon read-out and Level-1 trigger interface

4.3.1 Possible architectures and system implementations

Figure 4.3 schematically points out the main differences between what is currently implemented to read-out the LAr calorimeters and prepare the Level-1 trigger information and what is being proposed for the Phase-I upgrades. While the main read-out is unchanged, all the elements which form and process the information for the Level-1 trigger will be re-designed.

The calorimeter signals are firstly amplified and summed in the main shaping amplifier ASIC housed on the Front-End Board (FEB). The ASIC provides an analog sum of its 4 inputs. Those sums are either across η or ϕ depending on the calorimeter section and layer. The signals are further grouped and summed in plugin boards, the Layer Sum Boards (LSB), 2 on each FEB, which provide the analog shaped sum of $\Delta\eta \times \Delta\phi = 0.1 \times 0.1$ "slices" in a single sampling layer of the EM-calorimeter, and then propagated to the Tower Builder Boards (TBB) through dedicated base planes, installed in the front-end crates.

The TBBs fulfil three main functions: fixed pole-zero cancellation for each of the layer sums, delay adjustments through a custom LC-lumped network programmed by a Bimux ASIC, and the actual sum across the 4 layers of the EM calorimeters to form analog trigger tower signals. The signals are then transmitted differentially over about 70 meters to the receiver system, where variable-gain amplifiers (VGA) allow the adjustment of the signal gains.

Any upgrade planned for Phase-I will need to be adiabatic with respect to the current system since the main Level-1 calorimeter trigger architecture will remain as is: the system will need to maintain the existing functionality but will also provide additional information and processing capability. Figure 4.3 shows in red the functional blocks which are either new or need to be replaced: higher granularity data in the analog front-end, in particular at the output of the LSB plugins through the backplane, a new hybrid tower builder board, which filters, processes the analog signals (and forms the $\Delta\eta \times \Delta\phi = 0.1 \times 0.1$ trigger towers), digitizes and sends them over fast
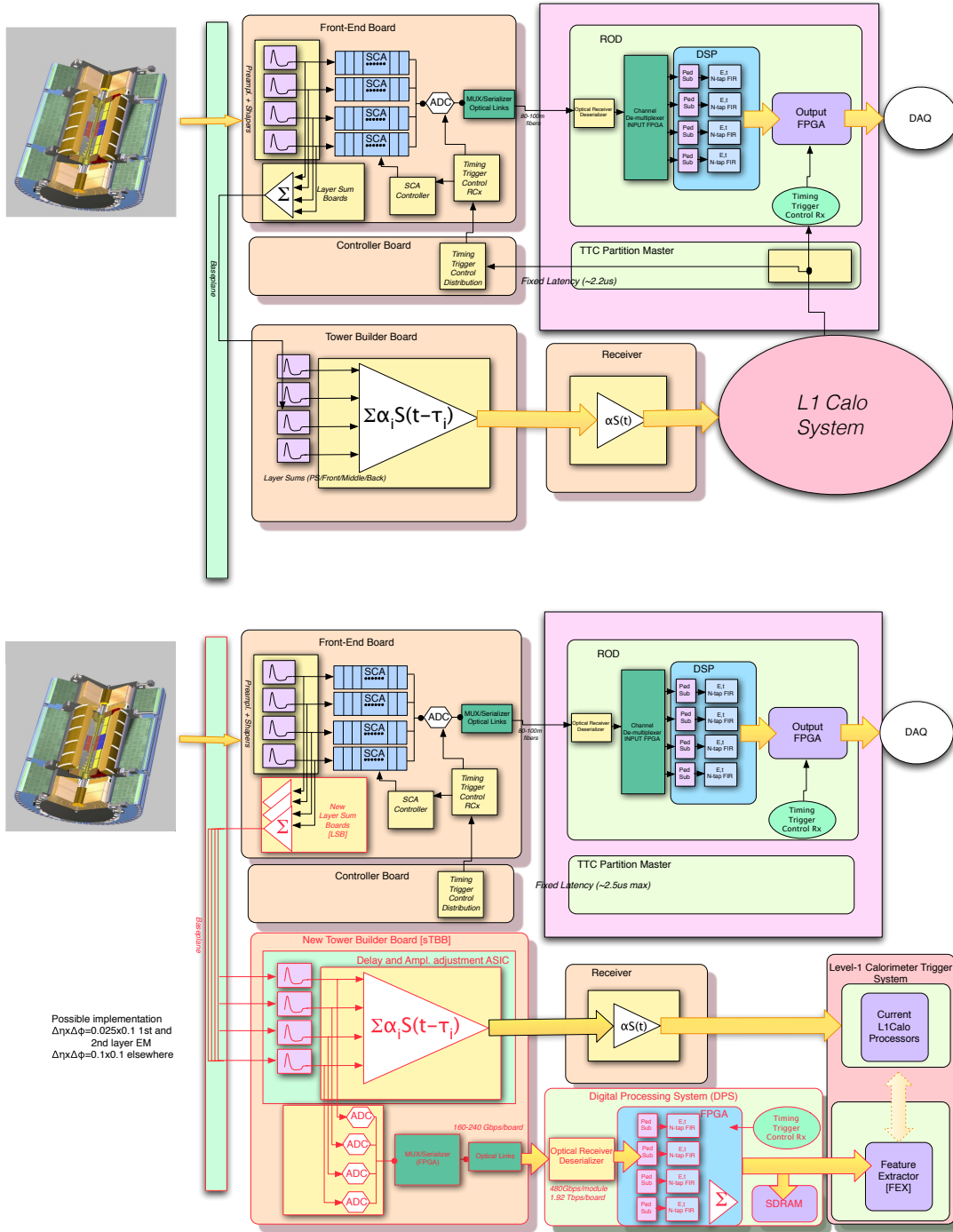
Figure 4.3. Top Panel. Current architecture of the LAr-Level-1 trigger interface. Bottom Panel. The architecture proposed for the Phase-I upgrades. In red the proposed new LAr elements.

parallel optical links to the receiver systems, where the raw-data samples are transformed to fully calibrated transverse energies deposited in each detector "slice" element at every bunch crossing.

4.3.2 Analog front-end read-out

The first two stages of summing of analog signals are made in the Front-End Boards [24].

4.3.2.1 The linear mixer of the front-end shaper ASIC   The shaper ASIC [25], designed in AMS 1.2 μm Bi-CMOS technology, implements a linear mixer circuit, which sums the output of the 4 preamplifiers with gain selectable through an external pull-up pin. The last stage of the linear mixer is a CR-RC shaper. The block diagram of the linear mixer is shown in Fig. 4.4.
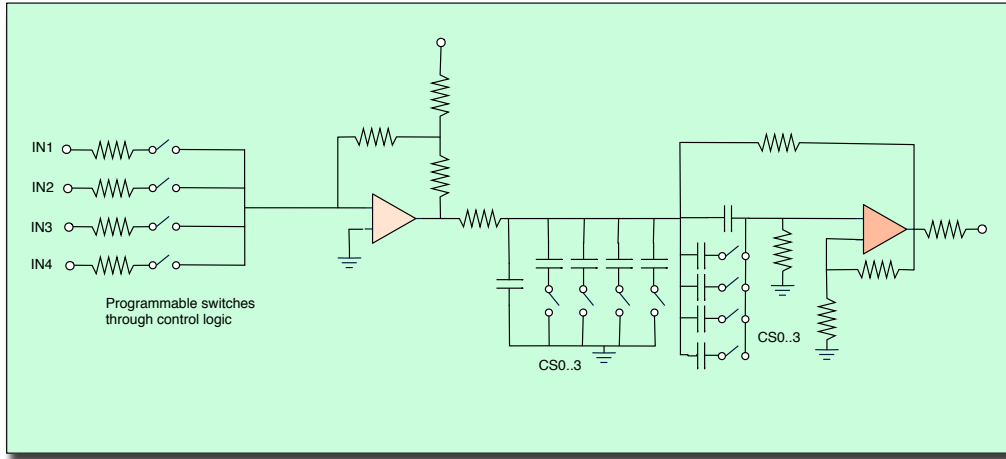
Figure 4.4. Simplified schematic of the linear mixer circuit in the front-end shaper.

The calorimeter channels are mapped to the FEBs in a well defined way [26], which remains unchanged during the Phase-I upgrade. Therefore, signal sums of the linear mixer circuit are identical to those performed currently. When extracting trigger signals directly at the output of the linear mixer, the following granularities are available in the 4 LAr barrel EM calorimeter layers: $\Delta\eta \times \Delta\phi = 0.1 \times 0.1$ (presampler), 0.0125×0.1 (front layer strips), 0.025×0.1 (middle layer pads), 0.05×0.1 (back layer pads).

This configuration cannot be changed without a complete redesign of the FEB, which is not foreseen for the Phase-I upgrades.

4.3.2.2 Layer sum boards   The second stage of summing is made on the FEB through the layer sum boards (LSB), which are pluggable daughter cards, 2 on each FEB, to provide analog sum signals for a corresponding area of $\Delta\eta \times \Delta\phi = 0.1 \times 0.1$ in each of the 4 sampling layers. Table 4.1 summarizes, as an example, the configuration on each of the FEBs installed on the EM barrel calorimeter [22]. To increase transverse granularity, the LSB for the front and middle layer FEBs have to be replaced by new LSBs, with different summing and optimized gains.

4.3.2.3 Front-end trigger baseplanes   While currently each TBB board receives 116 analog signals, for the Phase-I upgrades, the numbers of input signals will be increased by more than a factor 2 (for a total of 284 signals in the configuration summarized in Table 4.1). A new baseplane is required for the Phase-I upgrades to handle the larger number of signals at the input of the Tower Builder. The channel density in the new baseplanes is feasible but will require attention at the design level to preserve signal integrity and keep low noise levels.

EMB layer	Input $\Delta\eta \times \Delta\phi$	Current LSB Type	No. of outputs (current cfg)	Upgrade LSB type	Upgrade Output $\Delta\eta \times \Delta\phi$	No. of outputs (upgrade cfg.)
PS	0.1×0.1	S1x16	16	S1x16	0.1×0.1	16
Front	0.0125×0.1	S8x2	2	S2x8	0.025x0.1	8
Middle	0.025×0.1	S4x4	4	S1x16	0.025×0.1	16
Back	0.05×0.1	S2x8	8	S2x8	0.1×0.1	8

Table 4.1. Current and proposed upgrade configuration of the Layer Sum Boards on the barrel EM calorimeter (EMB)

4.3.3 On-detector mixed analog-digital trigger sums

Analog trigger tower as well as the additional information from each calorimeter layer is formed and prepared for the trigger processors in the Tower Builder Boards (sTBB). A new mixed analog-digital design is required to shape, digitize, serialize and transmit on optical fiber bundles all the 284 LSB output signals. If backward compatibility with the original TBB needs to be maintained, trigger tower signals of $\Delta\eta \times \Delta\phi = 0.1 \times 0.1$ are formed and driven differentially over existing 70 m twisted pair cables to the receiver stations in USA-15.

4.3.3.1 Analog trigger tower signal conditioning The output trigger tower sums of the sTBB will be required to follow the specification of the original board: signal peaking time of 35 ± 3 ns, gain precision better than 5%, and integral non-linearity better than 1% over the full dynamic range (0-2.5V). The upper limit of the dynamic range should correspond to 256 GeV E_T at $\eta = 0$. The noise of the total trigger from the LSB is around $\simeq 500$ MeV, and the intrinsic contribution of the sTBB components has to be negligible (<10% of the total noise). Signal conditioning requires the implementation of the following functional blocks for each of the arriving signals:

- Impedance controlled, fixed gain, input receiver.

- Linear fanout and drivers to the new digital section for each of the input layer sum signals.

- First stage of linear mixer to sum the individual layer sums in square sums of size $\Delta\eta \times \Delta\phi = 0.1 \times 0.1$.

- Pole zero compensation to equalize signal peaking time and amplitude compensation for all the signals coming from the different layers.

- Programmable delay line to compensate the differences in cable length and the particle time-of-flight between the different inputs.

- Impedance controlled delay line receiver.

- Linear mixer among the four calorimeter layers to form the trigger tower sum.

- Output differential drivers.

The development of a dedicated ASIC either in pure CMOS (0.13 or 0.18 μm) or in SiGe BiCMOS technology to implement all the functional blocks is being considered by the collaboration.

The main benefit of such an approach with respect to a more traditional design based on discrete components relies on it being a cost effective solution which will remove challenging integration issues in the design and layout of printed boards as well as in its power management.

4.3.3.2 Digitization The high granularity analog signals have to be digitized individually by a high precision fast converter. Studies on the specification and the optimization of its main parameters (sampling frequency, dynamic range, effective number of bits) are in progress, in particular in relation to their impact on the overall trigger performance. The minimum sampling frequency is 40 MHz. The dynamic range and effective number of bits need to be optimized in order to allow the Level-1 trigger processors to make use of better resolution to implement more selective algorithms while keeping the performance requirements manageable.

More importantly, these devices will have to be characterized by low power consumption (see Section 4.3.3.4) and by extremely short conversion time. A strong constraint on the trigger readout system is imposed by the trigger Level-1 latency which requires Level-1 accept signals to be received by the FE electronics within a limited fixed latency (see Chapter 7 for further details).

Two main lines of R&D are being pursued in parallel by several groups in the collaboration to address questions related to the technology and the architecture of these converters: characterization of commercial-off-the-shelf devices and design and development of ASIC ADCs. The former has the advantage of being cost effective (no development costs), and a few devices have been found meeting the technical constraints and satisfying requirements in terms of total ionisation dose. However their sensitivity to single event effects are a concern which is being investigated. The latter presents the advantage of using radiation tolerant technologies but with higher development costs and time. The baseline plan, at this stage of the development, relies on an ASIC implementation for the production and installation of the final system, while a commercial device will be used as backup choice and for the early demonstrator phase.

Early architectural studies, using pipelined and successive-approximation-register designs are being developed. Also, early prototypes in CMOS 0.13μm technology are confirming the design's performance expectations [27], [28].

4.3.3.3 Serialization and optical transmission Digitized data from the individual layers will need to be multiplexed then serialized for the off-detector transmission.

Multiplexers and serializers will need to implement some of the following functional blocks:

- Form a transmission frame where a local clock counter may be inserted into the ADC data.

- Encode the frame which provides the deserializer in the receiver side to recover the word boundary.

- Scramble to provide DC balance.

- Insert error correction or detection (for example, parity bits for each frame).

Different encoding and error detection schemes are being evaluated: both standard encoding schemes commonly used in high speed optical links, e.g. 8b/10b and 64b/66b, or novel encoding/framing schemes optimized for prompt corrections and re-synchronizations of the links [29]. Embedded synchronization codes or cyclic control and synchronization messages and redundancy

schemes may be needed for high speed serial communication systems installed in a radiation environment. Indeed single event upsets may appear as single bit flips or as burst errors which cause the deserializer at the receiving end to lose the word alignment requiring a re-synchronization sequence. Technology selection and dedicated design techniques will be used to minimize these type of events, but most probably they cannot be completely eliminated.

In the configuration of a TBB sending 284 signals at 40MHz, the total bandwidth may range approximately between 200-300Gbps (depending on the overhead of the encoding/decoding and error detection and correction schemes). Configurations with 4 optical transceivers supporting 10Gbps/channel are being considered and developed, taking advantage of the rapid industry developments on parallel optical transceivers.

4.3.3.4 Integration and power distribution Integration and system aspects of the sTBB board are part of the initial studies and developments given the several boundary conditions of the current powering and cooling systems. The power consumption of the board is limited to 80-100 W, corresponding to 350 mW/channel. The density of the read-out channels is a factor 2.5 higher than the current Front-End board design. Power management, cooling interface, noise minimization and proper grounding are among the many system aspects to be considered in the design and specification. To maximize flexibility, ease of maintenance and future upgrade of external interfaces, the board is conceived as an assembly of different pluggable modules as illustrated in Fig. 4.5.
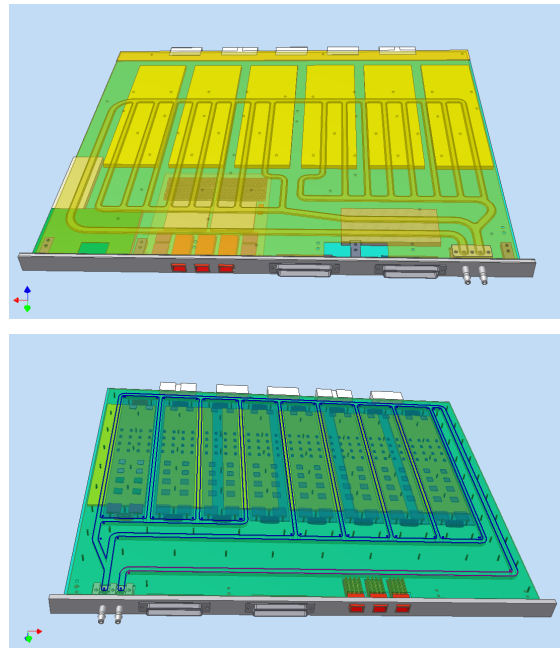
Figure 4.5. 3D model of the sTBB board for mechanical integration studies and developments.

4.3.4 Receiving, processing system and interface to the Level-1 calorimeter trigger system

The analog trigger tower information will continue to be processed by the Level-1 calorimeter trigger system without modification. The signals will be sent to the receiver system in USA-15,
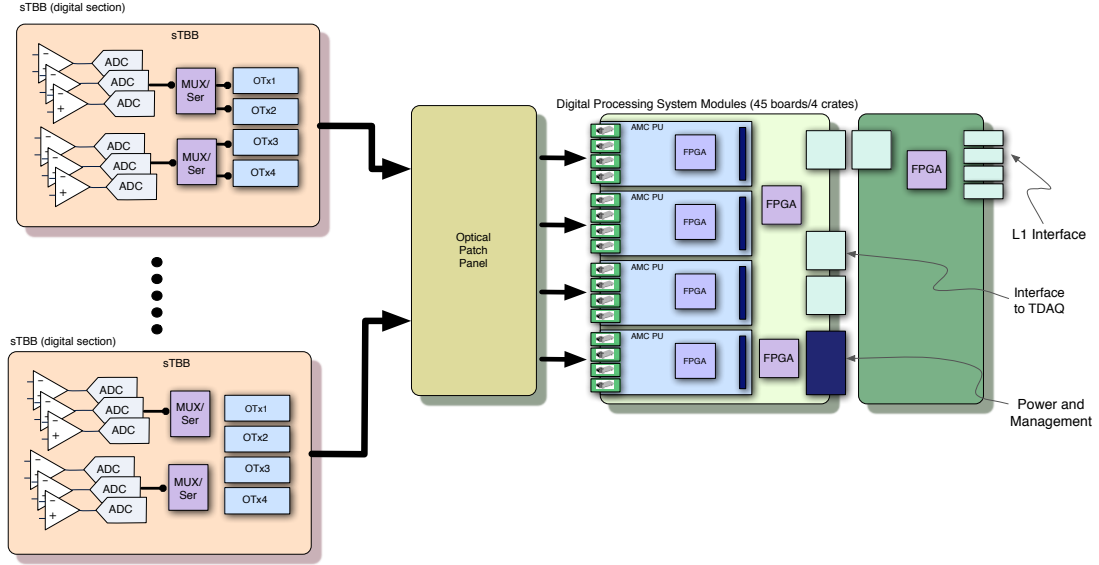
Figure 4.6. Block diagram of the receiving/processing system and interface to the Level-1 calorimeter processors.

which form the physical boundary between the LAr electronics and the Level-1 trigger electronics. This system implements four basic functions:

- Process analog signals with an integration stage and gain adjustment for loss compensation in the 70 meter cables from the detectors (to equalize gains at 2.5 V for E_T=250 GeV).

- Make two-fold analog sums among different modules to cover the calorimeter transition regions (e.g. where the corresponding trigger towers are split between barrel and end-cap detectors)

- Rearrange the input signals to an ordering appropriate for the Level-1 calorimeter trigger logic.

- Provide analog outputs to monitor signal waveforms.

The optical fibers carrying the digitized higher granularity data will be transmitted to receiving and processing modules before being sent to the Level-1 calorimeter trigger system (see Section 7.2 for further details). Figure 4.6 exemplifies a possible implementation under investigation:

- As for the analog trigger tower signals, the arriving optical signals are rearranged through an optical splice panel.

- Receiving modules realize opto-electrical conversion, time alignment of digital signals, error detection and correction.

- Proper subtraction of the baseline looking at the signal history over approximately 600ns, taking into account out-of-time pile-up contributions.

- FPGA-based processing units apply digital filtering techniques and convert raw ADC data to fully calibrated energy, and to transverse energy.

- Finally filtered data are transmitted serially to the following stage (see Section 7.2.3). The interface to the trigger will be designed and developed aiming at full compatibility with a similar interface to be developed for the Phase-II upgrades.

- Filtered data are locally buffered awaiting a Level-1 decision. Upon arrival of a Level-1 accept signal, data are transmitted to the DAQ and/or to the high-level trigger system.

A global optimization of the full chain is required because of the latency budget constraints during the Phase-I upgrade data taking: in particular the digitization process, and the different SER/DES stages may impact the latency budget significantly.

4.3.5 System considerations

Table 4.2 summarizes the number of the TBBs for all the LAr calorimeters, as well as the number of processing boards in USA-15. Approximately 120 new TBBs are needed to instrument all the EM calorimeters. About 30 processing boards (DPSs in Figs. 4.3 4.6), i.e. two full crates, will be required in USA-15.

Detector	Front-End Crates	sTTB	Processing Boards (DPS)
EM Barrel	32	64	16
EC Standard	16	32	8
EC Special	8	24	6
Total EM	56	120	30
HEC	8	16	2[‡]
FCal	2	4	
Total HEC+FCAL	10	20	2

Table 4.2. Summary table of the number of boards needed for the high granularity digital trigger for the LAr EM calorimeters. Also, the quantities needed for the FCal and the HEC are shown, in case such an upgrade will be extended to those detectors.

The table also includes the case of the hadronic end-cap (HEC) and forward calorimeters (FCal).

In those detectors tower builder boards (TBB) are replaced by tower drivers boards (TDBs) where no summation is made. Each TDB has 96 read-out channels driven directly to the receiver boards in USA-15. Plans to upgrade the TDB with mixed analog-digital boards similarly to that proposed for the EM calorimeters are being considered. However, it is not possible to increase the granularity in η, ϕ of the data sent to the trigger for the HEC.

4.3.6 Alternative designs

Alternative designs of the trigger read-out are being considered by the collaboration. They will be fully evaluated as part of an ATLAS-wide optimization process of the calorimeter trigger read-out

---

[‡] including also FCAL proto-trigger data

architecture and of its Level-1 trigger system in preparation for the Technical Design Reports of each system. Such a process will analyze benefits, challenges, risks and disadvantages, as well as costs and resource implications for each option. An example of alternative design is based on digitized data only, i.e. no analog trigger tower information is sent off detector. Input signals will be driven only to AD converters. No pole-zero correction, delay nor summing stages are implemented. The digitized information will be sent to the digital processing system where the original trigger tower signals will be reconstructed digitally. This alternative design has clearly the advantage of simplifying the design of the read-out on-detector, decreasing the overall channel density on-board and, therefore, in principle the risks associated.

However the implications on the overall Level-1 latency budget have to be fully analyzed (risk assessment including margins for the LAr calorimeters and the other systems). Also, major implications will follow in the calorimeter trigger systems, whose pre-processors, and, likely, the cluster modules and both e/γ and jet processors will have to be redesigned and rebuilt. Finally, an additional complication lies in the inter-calibration and data synchronization between the analog signals from the hadronic calorimeters and the digitized information from the EM calorimeters.

4.4 Proposed upgrade of the TileCal read-out

The full upgrade of the TileCal electronics is foreseen to occur in Phase-II. In anticipation of this it could be useful to make limited upgrades of the existing system in Phase-I provided the projected improvements fulfil needs and motivate risks and costs. Along these lines it has been considered to use the existing, so called, "muon trigger cables" to bring data from the outermost D-layer to USA-15 to deliver information about the depth distribution of the energy deposition should that prove to increase the trigger performance. Whether this is the case or not is subject to simulations. It is known that this does not improve the isolation in the electron triggers much, however, its value when considering jets and missing E_T is being studied.

It is judged that the detector itself (steel, scintillators, fibers, and PMTs) requires only minor adjustments. Only the elements with higher radiation exposure, the gap and cryostat scintillator systems, are expected to suffer significant damage.

The gap and cryostat scintillator detectors are designed to correct for energy losses in dead material between the Tilecal barrel (long barrel, LB) and extended barrel (EB), and between the central and forward electromagnetic calorimeter cryostats. These systems will suffer from radiation damage and are designed to be easily replaceable, exchanging the scintillator and wavelength-shifting fibers and re-using the "cans". The cryostat scintillators in particular, covering the rapidity range from 1.2 - 1.6, are in a high radiation environment of up to 10 kGy/year and are expected to suffer significant light loss (up to a factor of 2) after 10 years of nominal ATLAS running (100 fb^{-1}/year).

At the luminosities expected after the upgrades, the radiation damage will be even more severe. However the radiation dose is not uniform over the cryostat scintillators, but peaks rapidly towards the inner radius of the scintillators. The scintillators and read-out for each cryostat scintillator are subdivided into two radial segments, covering pseudo-rapidity intervals from 1.2-1.4 and 1.4-1.6, with the latter experiencing the highest radiation intensity.

There is a need to investigate possible use of new radiation-hard scintillators and wavelength-shifting fibers, as well as changing the eta segmentation to avoid the most radiation-intense region

from 1.5 to 1.6. A successful conclusion of this R&D investigation would lead eventually to the upgrade of those scintillators during Phase-I.

Even though the TileCal calibration system will be upgraded in Phase-0, most certainly there will be issues that need consolidation during Phase-I.

4.5 Proposed time plan and milestones
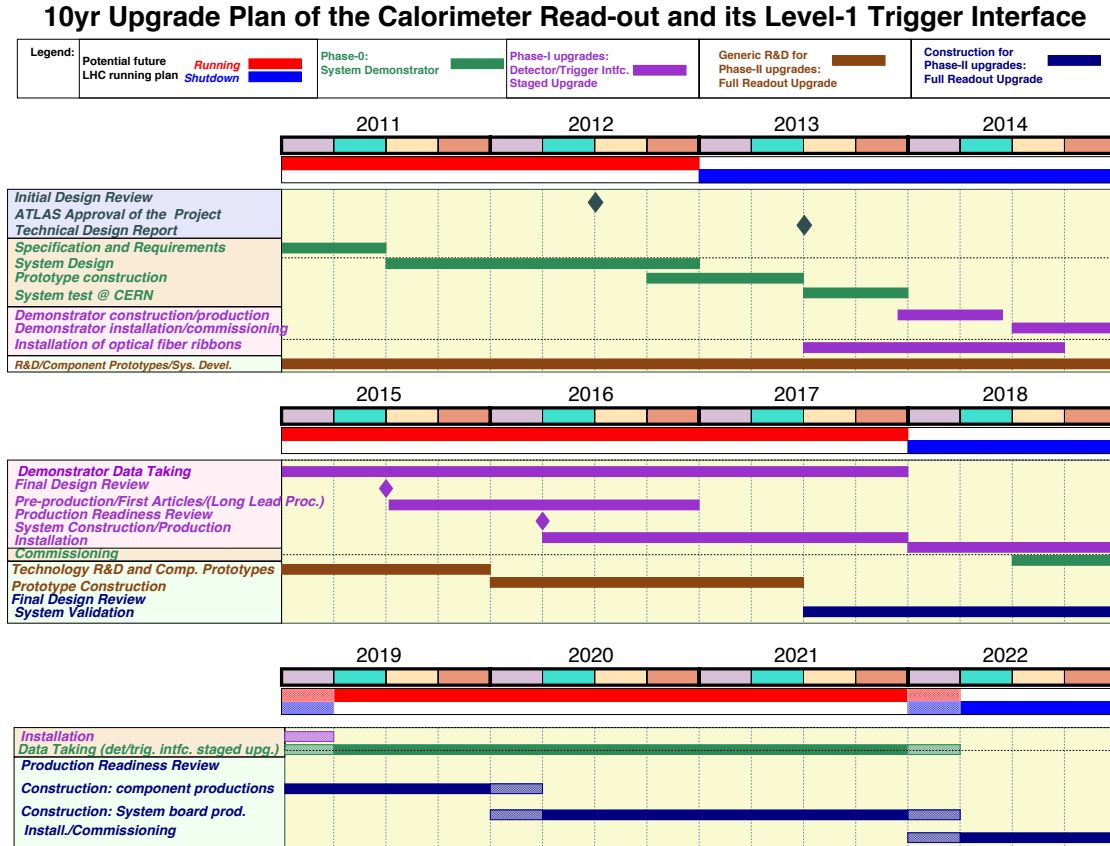
Figure 4.7. Possible implementation and timeline of a staged upgrade of the calorimeter read-out through the different phases of the LHC and ATLAS upgrades.

The ultimate objective (to be implemented for the HL-LHC) is to upgrade the whole calorimeter read-out, the on-detector electronics and the read-out driver in USA-15 as described in Section 10.2. The plan of upgrade the calorimeter trigger read-out in Phase-I and the full front-end read-out in Phase-II can be envisaged as a 4-stage program, whose guiding principle is to provide a "safe" way to gradually develop and validate the new architecture while keeping disruption to the existing system at a minimum.

More importantly, the staged solution allows time to understand operation at higher luminosity and allow for more intelligent algorithms already at the Phase-I stage. These more intelligent triggers (e.g. shape analysis, better reconstruction of the EM cluster position at Level-1, better timing and BC identification) will enhance the performance of the trigger significantly, allow the

implementation of more robust algorithms at Level-1 as the luminosity is increased and allow for much of the benefits mentioned in Section 2.5.

4.5.1 Implementation of a staged program

The staged upgrade program can be summarized as follows (a possible timeline of the staged program is depicted in Fig. 4.7):

- Architecture system test project implemented on a $\Delta\eta \times \Delta\phi = 0.4 \times 0.4$ calorimeter partition during the Phase-0 shutdown.

- "Adiabatic" upgrade of the calorimeter trigger read-out and of its trigger system in Phase-I as described in the previous sections.

- Continuing full support of R&D of critical front-end components for the Phase-II upgrades.

- Full upgrade of the detector read-out in Phase-II.

5. Forward Physics System

The proposal is to install an ATLAS Forward Proton (AFP) detector in order to detect protons at 206 and 214 meters on both side of the ATLAS experiment at very small scattering angles. The physics program addressed by AFP described in this section could not be performed using the other ATLAS forward detectors. For instance ALFA will be operated only in special high β^* beam optics conditions with the main purpose to measure the total pp cross section and the luminosity.
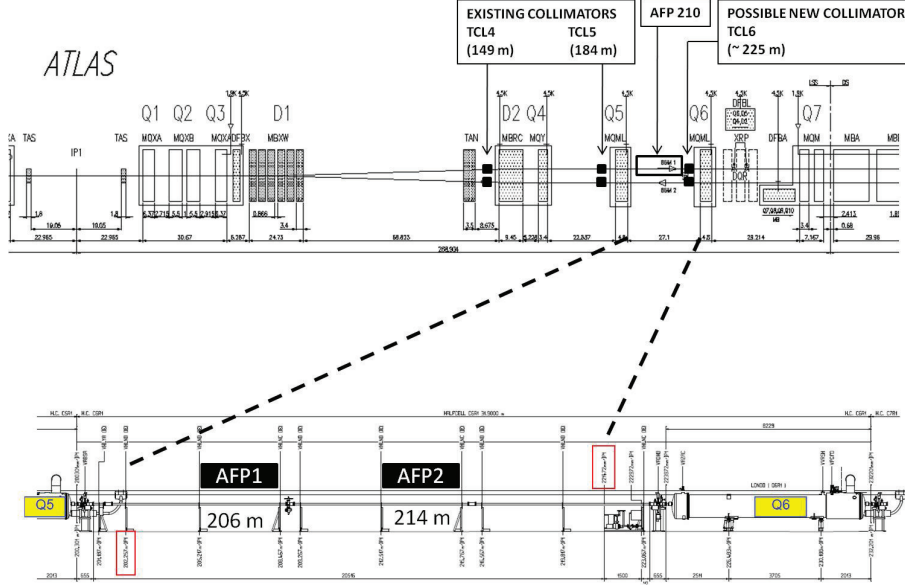
Figure 5.1. Sketch of the LHC beamline region where deployment of one arm of the AFP detector is planned. *Upper part:*Layout of the straight section from the ATLAS IP to the quadrupole Q7. The position of the AFP detector and of the collimators discussed in the section on the detector acceptance is indicated. *Lower part:* Expanded view of the region between 202.257 and 221.472 *m* where the AFP detector will be located. The two stations AFP1 at 206 *m* and AFP2 at 214 *m* are shown.

Figure 5.1 is a sketch of the LHC beamline region where deployment of the AFP detector is planned. This arm will consist of two sections (AFP1 and AFP2) of specialized beam pipe (see Section 5.3), that allows the detectors to be in a retracted position during the injection of protons into the LHC, and remotely positioned close to the beam after stable beam collisions are established. AFP1, is a small section of beam pipe with a "pocket" containing a 6 layer silicon tracking detector as described in Section 5.4. The second station AFP, which is about 8m further downstream from the ATLAS interaction point, will contain two pockets. The first pocket (ordering with increasing distance from the IP) has another tracking detector identical to the first AFP station, while the second pocket contains the QUARTIC timing detector described in Section 5.5. The aim of this setup, mirrored by an identical arm placed on the opposite side of the ATLAS IP, will be to tag and measure the momentum, angle, and time-of-flight of protons emerging intact from the pp interactions thus allowing ATLAS to expand its physics capabilities both in Standard Model and exploratory physics as described in Section 5.1. This program will be unique among the LHC experiments, thanks to the important capability added to this project by the timing detectors which

allow one to reconstruct with a few *mm* precision the *pp* interaction vertex using the two tagged protons. In this way one can efficiently reject the pile-up background of a central system superimposed on two single and independent diffractive proton events in the same bunch crossing. This type of fake background becomes quite significant, and would overwhelm many of the signals of interest at the highest values of μ anticipated in Phase-I. The above mentioned few *mm* spatial resolution corresponds to the presently achieved time resolution of about 10 *ps*, which is eventually to be considered as an upper limit, with respect to the goal and possible performance of the proposed timing detector.

The acceptance of the detector and the strategy proposed to optimize it by changing the collimator settings is described in Section 5.2. Finally, in Section 5.6 the proposed time scale for the detector installation will be presented.

The physics reaches reported in Section 5.1 are obtained after a full simulation using the ATLAS MC of both signal and backgrounds (including pile-up effects).

5.1 Physics motivation

The purpose of the new forward detectors described in this Letter of Intent is to open a possibility to identify and record events with leading intact protons emerging from diffractive collisions occurring in ATLAS. The main physics output comes from the remarkable capability of AFP to tag and measure both protons in the final state and can be divided in two different classes:

- "exploratory" physics, concerning in particular the search for anomalous couplings between γ and W or Z bosons, which allow models beyond the SM (for example extra-dimension and Higgs-less models) to be probed with an unprecedented precision at the LHC. In addition, in the case that the Higgs or some other new particle is discovered, it can potentially be produced and (depending on its mass) observed in the exclusive diffractive mode, allowing its spin and its mass to be determined on a per event basis with high precision.

- "standard" QCD physics, such as double Pomeron exchange (DPE) measurements in the jet, Z, W channels, and the search of exclusive production in the jet channel for instance. For these processes, both protons in the final state are tagged. DPE production of dijets and W/Z bosons are described in the QCD part. These topics follow the measurements obtained in diffraction at HERA (H1/ZEUS) and the Tevatron (CDF/D0), and allow extension of these measurements to a completely new kinematical domain. Tests of QCD evolution as well as a better determination of the partonic structure of the exchanged colorless object, the Pomeron, can be performed.

In the following, these two topics are described further. As a baseline for the analysis, 40/300 fb^{-1} are taken for exploratory physics and 10 fb^{-1} for QCD processes. In the full simulation an average number of interactions per bunch crossing $\mu =$23 or 46 are assumed.

Within such a high pile-up environment, the leading background is from non-diffractive events overlapping with two intact protons originating from pile-up events. The AFP acceptance together with the timing detectors allows a significant reduction in the background as shown in Fig. 5.2. The background reduction factor is about 200 at $\mu \sim 23$ requiring both protons to be inside the AFP acceptance and for timing detectors with a 10 ps resolution. Requiring the diffractively produced
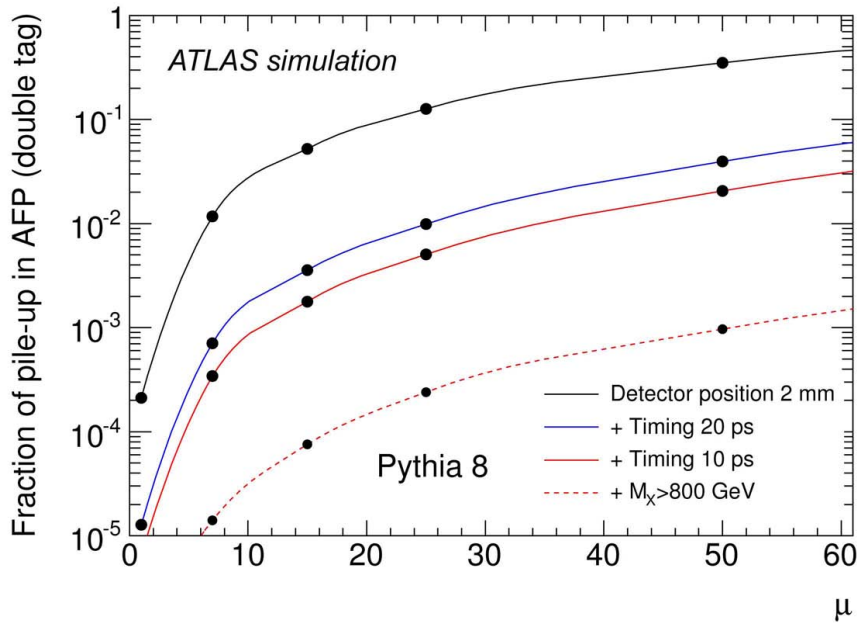
Figure 5.2. Fraction of pile-up events in AFP (double tagged events) as a function of the average number of interactions with a timing resolution of 20, 10 ps, and for a diffractive mass greater than 800 GeV.

object to be at high mass above 800 GeV allows the fraction of pile-up background events to be reduced to 2×10^{-4} for $\mu = 23$ and 10^{-3} for $\mu = 46$.

5.1.1 Exploratory physics: anomalous couplings between *W/Z* bosons and γ

The AFP will improve the reach of ATLAS for physics beyond the Standard Model. At the same time, the reach for probing Higgs-less or extra-dimension models can significantly be enhanced. One possible key parameter is the sensitivity to anomalous couplings, which has been shown to probe both Higgs-less and extra-dimension models far behind what other analysis might do by combining very forward proton information to more central topologies. The search for anomalous couplings originating from dimension 6 operators between γ and W/Z bosons is obviously fundamental if no Higgs boson is found at the LHC, since alternative Higgs-less models will be needed. Even in the case that a Higgs boson is discovered, gauge anomalous couplings originating from dimension 6 operators are still predicted by extra-dimension theories. In either case, the improved sensitivity is sufficient to indicate the presence of extra-dimensions or other new physics. Low cross-section measurements, such as the search for anomalous quartic couplings, will require the AFP detector to operate at high instantaneous luminosity, where overlaps or pile-up backgrounds must be considered. To study this, the process of W pair production induced by the exchange of two photons as shown in Fig. 5.3 [30] has been simulated. It is a pure QED process in which the decay products of the W bosons are measured in the central detector and the scattered protons travel intact in the beam pipe at very small angles, where they are eventually detected by the AFP. The superposition of a standard W pair event with two single diffractive events is the leading background for this process.
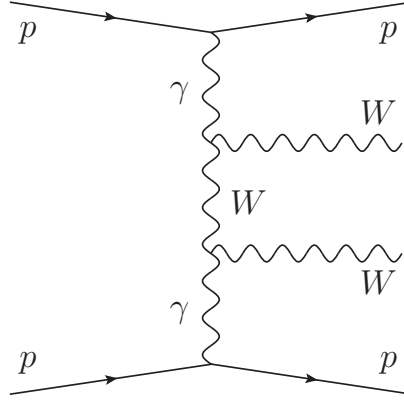
Figure 5.3. Sketch diagram showing the two-photon production of a central system.

The lowest order interaction Lagrangian involving two photons are dim-6 operators and the following parameterizations of the quartic couplings is adopted.

$$\mathcal{L}_6^0 = \frac{-e^2}{8} \frac{a_0^W}{\Lambda^2} F_{\mu\nu} F^{\mu\nu} W^{+\alpha} W_\alpha^- - \frac{e^2}{16\cos^2\theta_W} \frac{a_0^Z}{\Lambda^2} F_{\mu\nu} F^{\mu\nu} Z^\alpha Z_\alpha$$

$$\mathcal{L}_6^C = \frac{-e^2}{8} \frac{a_C^W}{\Lambda^2} F_{\mu\alpha} F^{\mu\beta} \frac{(W^{+\alpha} W_\beta^- + W^{-\alpha} W_\beta^+)}{2} - \frac{e^2}{16\cos^2\theta_W} \frac{a_C^Z}{\Lambda^2} F_{\mu\alpha} F^{\mu\beta} Z^\alpha Z_\beta \quad (5.1)$$

where a_0, a_C are the parameterized new coupling constants and the new scale Λ is introduced so that the Lagrangian density has the correct dimension four and is interpreted as the typical mass scale of new physics.

The results concerning the search for quartic anomalous couplings are presented in the physics chapter of this document and the gain is about two orders of magnitude with respect to the standard ATLAS reach without the AFP, reaching the sensitivity needed to probe Higgs-less and extra-dimension models.

5.1.2 QCD physics

The new AFP detector will allow ATLAS to explore QCD and the structure of diffraction in a completely new kinematical domain at high mass and high p_T following the measurements performed at HERA and at the TEVATRON. The following fundamental questions will be explored:

- What is the structure of diffraction? Can one understand the structure of the colorless exchanged object (the Pomeron) and describe it in terms of quarks and gluons? Can the QCD evolution be described in terms of the Dokshitzer-Gribov-Lipatov-Altarelli-Parisi [31] (DGLAP) mechanism?

- What is the structure of this object at the LHC energy, where very high gluon densities are reached. This has important consequences in QCD since non-linear QCD effects and new phenomena such as saturation are expected to appear. The test of the QCD evolution using the jet cross-section measurements will allow ATLAS to probe such effects.

- What is the production cross-section for exclusive diffractive events in the photon or jet channels? It is fundamental to understand this new class of events and to constrain further the exclusive Higgs production [32].

- In addition to the hard diffractive regime, in at least 90% of the events, the hard interaction is accompanied by soft exchanges which fills the rapidity gap or removes the intact proton in the final state. The understanding of the survival probability relates directly to soft exchanges and underlying events and is fundamental for many processes at the LHC.

More details on the strategy of AFP to address these points can be found in Section 9.3.

5.2 Collimators, beam simulation and detector acceptance

Protons that have lost typically 100 GeV or more energy in the primary interaction, emerge laterally in the AFP acceptance after passing through quadrupoles and bending magnets as shown in Fig. 5.4. The acceptance and energy resolution of the forward detectors depends on the LHC beam optics and on the position of the detectors relative to the beam.

Collimators are placed around the outgoing beams from ATLAS to protect beamline elements from collision debris. These TCL collimators have been nominally set in simulation, but the present baseline scheme for the LHC beamline has the effect of obstructing the acceptance of the downstream proposed detector stations. A solution is proposed (see Fig. 5.1) in which the existing collimators TCL.4 and TCL.5 (at approximately 150 and 184 m from the interaction point) are retained and a new collimator TCL.6 is installed at 225 m. The addition of the new collimator allows
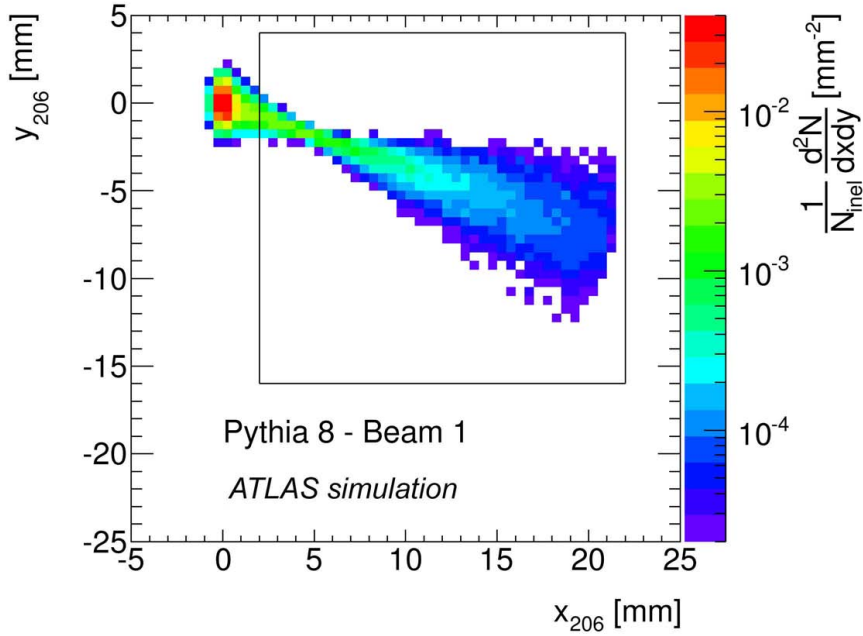
Figure 5.4. Simulation of the diffractively scattered proton position distribution at the level of the AFP1 station at 206 m. Superimposed to the distribution is a square of 20 mm x 20 mm, representing the acceptance of one layer of the Silicon detector tracker.

the aperture of TCL.4 and TCL.5 to be relaxed and restores the acceptance. Apertures for TCL.4, TCL.5 and TCL.6 of 30σ, 50σ and 40σ, respectively, have been shown in simulation to provide excellent protection for the beamline while allowing a good acceptance for the AFP stations [33].

Detailed studies have been carried out regarding the machine-induced backgrounds in the Long Straight Section (LSS) of ATLAS, describing the background and radiation environment [34]. Furthermore RF and impedance studies have been made of prototype pocket designs [34], showing that the RF impact on the beam is small for both single and double pocket configurations.

The fast tracking program, FPTrack [35], now incorporated into the ATHENA package, has been verified in detail against the MAD-X package, and is used to study acceptances and resolutions. Forward protons emerging from the interaction region are tracked through the system of magnets and collimators that comprise the beamline. An updatable model of the LHC beamline optics is implemented, using fully momentum-dependent thick-magnet formula at each beamline element. Collimators are taken into account, as are the apertures of the beamline elements. The ExHuME and FPMC Monte Carlo [36] have been used to generate outgoing protons from the central exclusive production of various final states. For a given optics, the position and direction of a proton hitting the 210 m detectors depend chiefly on the energy E and scattering angle θ of the proton emerging from the primary interaction. These primary quantities can be obtained from the measurements by means of a parameterized formula, enabling the mass of the centrally produced object to be determined independently of the measurements in the ATLAS detector, and usually much more precisely. Figure 5.5 shows the acceptance for detecting centrally produced objects generated by the photon-photon process, as a function of their mass and of the distance of the tracking station from the beam. The collimator settings affect the acceptance at higher mass values.

The measured mass resolution of an exclusive centrally-produced narrow object is affected by:

- the Gaussian width of the momentum distribution of the circulating proton beam (0.77 GeV);

- the lateral uncertainty of the position of the interaction;

- the angular spread of the interacting beams, equivalent to a lateral momentum smearing of 0.21 GeV on the outgoing proton;

- the position measurement uncertainty in the detector system;

- the angular measurement uncertainty in the detector system.

A mass resolution of 3-4 GeV can be achieved if the proton impact point and horizontal direction are measured to 10 μm and 1 μrad respectively, degrading to 5 GeV if the direction is measured to 2 μrad.

A consistent alignment of the silicon system relative to the magnets, the beamline and the experimental hall can be achieved in real time by means of beam position monitors (BPMs). Two options for BPMs are being considered: a large-aperture BPM mounted directly on the moving beampipe and related to the position of the silicon detectors by knowledge of the mechanical structure of the assembly, and a system of BPMs mounted on the (fixed) LHC beampipe at both ends of

the region, with their position and the moving silicon detectors' positions referenced to an alignment wire using a Wire Positioning Sensor (WPS) system. It is likely that both systems will be employed. A measurement precision of a few microns is expected.

However to take into account any unknown or unforeseen effects, it is necessary to calibrate the momentum measurement of the protons. The procedures to perform this calibration are under study. One promising candidate is, for instance, a calibration performed by means of the photoproduction of lepton pairs, of which muon pairs give the best precision, in the central ATLAS detector. Triggers exist that should be able to record events in which a muon pair is produced by the photon-photon process where the photons radiate off the protons. The accurately measured momenta of the muons allow the momenta of the forward protons to be accurately evaluated, and compared to the values measured in the forward system. It is not necessary to record both of the forward protons in any given event. Using the LPAIR program to generate muon pairs produced within a rapidity range of ± 2.5, the rates of calibration events that can be obtained in this way has been estimated. To calibrate a shift of the mean momentum of one-seventh of its measured resolution, 50 events would be required, since the backgrounds will be small. With the silicon detectors positioned at a distance of 2.0, 2.5, and 3.0 mm from the beam an integrated luminosity of 1.1, 2.6 and 6.6 fb^{-1} will be required to make a calibration. Obviously the situation is improved if the detectors are as close as possible to the beam.
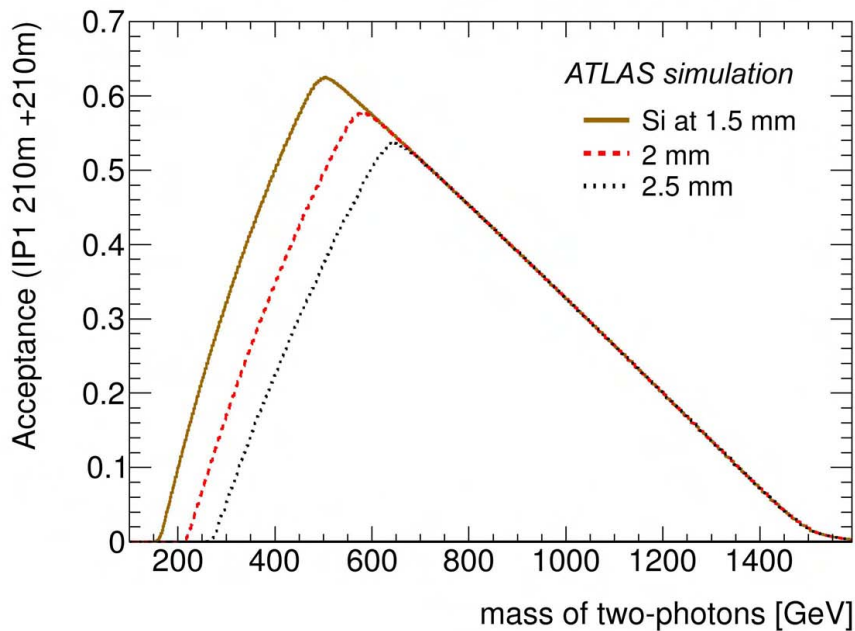
Figure 5.5. Acceptance as a function of centrally produced mass for 210 + 210 m proton tags for the edge of the silicon detector active region located at different distances from the beam. The collimators are closed. Version 6.503 of the LHC optics files has been used with: beam energy spread $\sigma_E = 0.77$ GeV, $\beta^* = 0.55$ m; angular divergence at the IP $\sigma_\theta = 30.2$ μrad; crossing angle = 142.5 μrad in the vertical plane at IP1 .
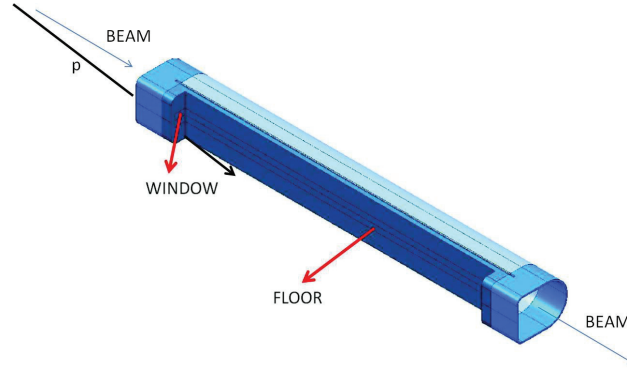
Figure 5.6. Design of the thin window. A pictorial view of an intact proton from diffractive interaction traveling close to the beam and crossing the detector volume is also provided.

5.3 The movable beam pipe

In order to measure the scattered protons, a specialized movable beam pipe (Hamburg Beam Pipe, HBP) is under development, based on a design successfully deployed at DESY in 1995 [37]. In its design, the dominant aspect is the minimization of the thickness of the portions called floor and window (see Fig. 5.6). In order to minimize multiple scattering and secondary particle emission the thickness of the window must be as low as possible. In order to maximize the physics acceptance, it is also necessary to minimize the distance between the detectors and the beam including the thickness of floor. As the size of the detectors is approximately 20×20 mm, the initial design uses a height of 24 mm for both floor and window as well as a depth of 22 mm. In this project, the beam pipe AFP1 (see Fig. 5.1) hosts the first tracking stations in a pocket with a floor length of about 100 mm, while the other beam pipe (AFP2) is split in two independent portions hosting in the first one a Si detector (floor length of about 100 mm) and in the second one (floor length of about 700 mm) the timing detector (QUARTIC).

The thicknesses of the floor and the window are 300 μm and 250 μm respectively so that the maximum level of stress, located at the transition between the thin wall and the rest of the beam pipe, does not exceed the yield point of the chosen material (austenitic steel AISI 316LN). The value of the window meets the need of a cumulative thickness smaller than 1 mm.

To realize this beam pipe several manufacturing steps are needed. The portion of pipe including floor and window is roughly machined leaving a fairly good amount of extra material to preserve its rigidity during laser or electron beam welding. In the case of full a penetration weld, all welding burrs interacting with the beam must be removed by polishing the surfaces before doing the final EDM machining setting the definitive dimensions. To reduce the roughness, the beam pipe may be electro-polished before being NEG coated.

To prevent a possible vacuum breakdown, the beam pipe and all detectors are housed in a sealed container where medium vacuum is mantained (secondary vacuum). From a mechanical point of view, the beam pipe does not see any wall deformation and, therefore its horizontal movement towards the beam does not have to be corrected or offset. Operating in medium vacuum might be electrically unsafe because of voltage breakdown, as the Si detector (voltage up to few hundred volts) should be placed very close to the beam pipe floor. This implies that the floor or the detector

BELLOWS

SILICON DETECTOR BEAM PIPE

BPM

TIMING DETECTORS BEAM PIPE

214 m

SILICONDETECTORS

QRL

206 m
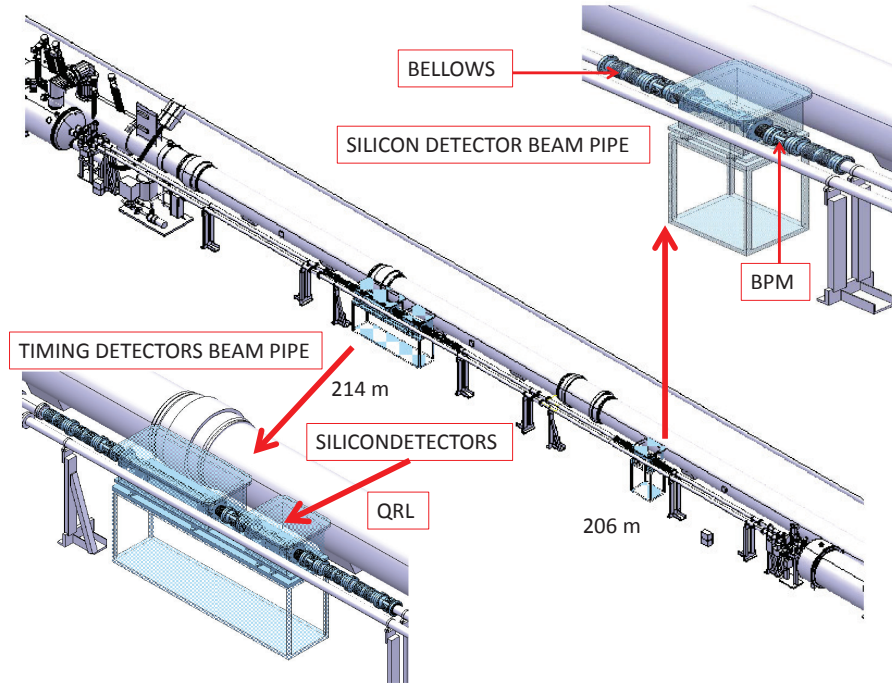
Figure 5.7. Overall setup at 210 m.

has to be insulated. The range of motion of the beam pipe can vary from 15 to 35 mm according to its shape depending on vacuum impedance. The target for the precision and the reproducibility of the displacement towards the beam of the whole assembly (beam pipe, detectors and container), placed on a moving table remotely controlled via a system similar to the one used for the LHC collimators, would be around 10 - 20 μm while the accuracy of the measurement of the movement should be better than 10 μm.

In the direction of the scattered proton, the layout of the installation consists of a first BPM, two or three bellows (depending on the vacuum impedance) permitting a displacement from 25 to about 40 mm (around 12 mm per bellow), the second BPM, the container where the beam pipe and the detector is housed in, the third BPM out of the container, two or three bellows and the forth BPM. A WPS (Wire Position System) is installed on the first and the fourth BPM.

5.4 Silicon tracking detector

The purpose of the tracker system is to measure points along the trajectory of beam protons that are deflected at small angles as a result of collisions. The tracker when combined with the LHC dipole and quadrupole magnets, forms a powerful momentum spectrometer. As anticipated in the introduction, the silicon tracker stations will be installed in HBP at $\pm$ 206 and $\pm$ 214 m from the ATLAS IP. To reconstruct the mass of the central system produced in ATLAS, it is necessary to measure both the distance from the beam and the angle of the proton tracks relative to the beam with high precision, so, as already mentioned, BPMs have been integrated into the HBP system.

The smallest distance at which sensors can approach the beam to detect the scattered protons determines the minimum fractional momentum loss (ξ) of detectable protons. With a typi-

cal LHC beam size at 210 m of $\sigma_{beam} \approx 100\ \mu$m, the window surface of HBP can theoretically safely approach the beam to $15 \times \sigma_{beam} \approx 1.5$ mm. The thickness of the thin window is approximately 250 μm and the dead region of the sensors ranges between $\sim 200 \mu m$ (for 3D sensors) and 250 μm (for planar) giving the closest distance of about 2 mm. This corresponds roughly to the range $0.02 < \xi < 0.2$ and consequently to a range of central masses from a few hundred GeV to beyond one TeV for double-tagged events as already shown in Fig. 5.5 for the case of central photoproduction. Placing the sensors a few millimeters from the beam imposes high demands on the radiation hardness, the radio frequency pick-up in the detector and the local front-end electronics.

The key requirements for the silicon tracking system at 210 m are:

- Spatial resolution of $\sim$ 10 (30) μm per detector station in x (y)

- Angular resolution for a pair of detectors of about 1 μrad

- High efficiency over an area of 20 mm $\times$ 20 mm.

- Minimal dead space at the edge of the sensors

- Sufficient radiation hardness

- Capable of robust and reliable operation at high LHC luminosity

The basic building unit of the AFP track detection system is a module consisting of an assembly of a sensor array and on-sensor read-out chip, passive components and electrical services for LV, HV and signal routing. The module will be mounted on the mechanical support with embedded cooling and other necessary services.

Concerning the choice of the sensor type, the AFP is closely watching the decision process of the IBL (Insertable B Layer) upgrade project [38] and is willing to follow its decision because it has a very similar time schedule and main requirements (see above). The IBL considered two options of the silicon sensors, namely the 3D and planar slim-edge n-in-n. Recently, the Panel for the choice of the IBL sensor type concluded that both technologies satisfied the IBL performance requirements. For the AFP detectors, the 3D option has clear advantages in providing very short inactive edges (of the order of $\sim 200 \mu m$), high radiation tolerance and low bias voltage. Therefore the 3D technology is considered as the baseline for the 2013-2014 installation (see Section 5.6) and the planar slim-edge n-in-n as the backup one.

For ATLAS tracking upgrades, starting with the IBL, the new front-end chip FE-I4 has been developed which supersedes the FE-I3 presently installed. The FE-I4 integrated circuit contains read-out circuitry for 26880 hybrid pixels arranged in 80 columns on 250 μm pitch by 336 rows on 50 μm pitch, and covers an area of about 19 mm $\times$ 20 mm. It is designed in a 130 nm feature size bulk CMOS process. Sensors must be DC coupled to FE-I4 with negative charge collection. The FE-I4 is very well suited to the AFP requirements: the granularity of cells provides a sufficient spatial resolution, the chip is radiation hard enough (up to a dose of 3 MGy), and the size of the chip is sufficiently large that one module can be served by just one chip. This significantly simplifies the design of the AFP tracker, as no special tiling arrangement is needed.

The dimensions of the individual cells in the FE-I4 chip are 50 μm $\times$ 250 μm in the x and y directions, respectively. Therefore to achieve the required position resolution in the x-direction of

$\sim 10~\mu$m, six layers with sensors are required (this gives $50/\sqrt{12}/\sqrt{5} \sim 7~\mu$m in x and roughly 5 times worse in y). Offsetting planes alternately to the left and right by one half pixel will give a further improvement in resolution of at least 30%. The required position and angular resolution is indeed obtained from the tracking studies and is consistent with a mass resolution of ~ 5 GeV.

Preliminary evaluations, to be confirmed, show that the AFP sensors are expected to be exposed to a dose of 30 kGy per year at a luminosity of 10^{34}cm^{-2}s^{-1}. For comparison, the innermost layer of the ATLAS Pixel detector is expected to be exposed to a dose of 200 kGy per year, and therefore much bigger than the one expected for the AFP. Results from test beams with the silicon pixel sensors in the ATLAS [39] and CMS [40] detectors show that the detection efficiency may be kept above 95% for fluences lower than $\sim 10^{15}$ n$_{eq}$ cm^{-2} if the irradiated sensors are operated at bias voltage of 600 V (non-irradiated sensors are normally operated at 150 V) and the pixel electron threshold are lowered.

The operation of silicon detectors at low temperature limits the leakage current. The experience with the ATLAS Pixel detector shows that it is sufficient to cool only the read-out electronics (the sensors are cooled indirectly via bump-bonding) to temperatures well below 0°C (-13°C in this case). Until proper thermal tests are done it is assumed that the detectors will be cooled to -15°C. A preferred option for the cooling is the Vortex based Dry Air Cooling System. A laboratory-scale prototype is available with a possibility to manipulate cooling air temperature between -40° and -10°. The dry air flows through channels inside the detector support structure and the cooling circuit is strictly separated from the secondary vacuum part. Tests with realistic AFP detector engineering mockups are envisaged.

5.5 The timing detector

A fast timing system that can precisely measure the time difference between outgoing scattered protons is a key component of the AFP detector. The time difference is equivalent to a constraint on the event vertex, thus the AFP timing detector can be used to reject overlap background by establishing that the two scattered protons did not originate from the same vertex as the central system, and can also be used to confirm that any observed signal is consistent with a single interaction. The final timing system should have the following characteristics:

- 10 ps or better resolution (20 ps is likely sufficient for the first couple of years of operation);

- acceptance comparable with the one of the tracking detector and efficiency close to unity;

- up to several MHz rate capability;

- enough granularity to minimize the pile-up of protons in the same readout channel also at the highest μ ;

- trigger capability.

Figure 5.8 shows a schematic overview of the proposed timing system, named QUARTIC, consisting of a quartz-based Cerenkov detector coupled to a microchannel plate photomultiplier tube (MCP-PMT), followed by the electronic elements that amplify, measure, and record the time of the event along with a stabilized reference clock signal. The QUARTIC detector consists of an array of

fused silica bars ranging in length from about 8 to 12 cm and oriented at the average Cerenkov angle. A proton that is sufficiently deflected from the beam axis will pass through a row of eight bars emitting Cerenkov photons, with those emitted in the appropriate azimuthal angular range accepted by the MCP-PMT, providing an overall time resolution that is approximately $\sqrt{8}$ times smaller than the single bar resolution of about 30 ps, thus approaching the 10 ps resolution goal without putting overly stringent requirements on any single measurement. Prototype tests have generally been performed on one row (8 channels) of 5 mm $\times$ 5 mm pixels, while the initial detector is foreseen to have four rows to obtain full acceptance out to 20 mm from the beam. The initial design had equal area pixels, but it is more sensible to have equal rate pixels, so it is planned to reduce the width of detector bins close to the beam, where the proton density is highest, while maintaining the same MCP-PMT pixel size to equalize the rate per unit area. One option to accomplish this is using a quartz-fiber version of the QUARTIC. Not only does this improve the multi-proton timing capability (which becomes important at high luminosity, where the overlap background is worst), but it also equalizes the current among MCP-PMT pixels, which helps extend the device lifetime.

Since MCP-PMT's were not believed to be sufficiently robust for the high rate LHC environment, MCP-PMT lifetime has been one of the key concerns about the viability the timing system. Consequently, lifetime studies and improvement has been one of the major focal points of the fast timing group's R&D effort (see for instance [41]). An extended lifetime multi-channel MCP-PMT suitable for the early phase of AFP deployment has been developed in conjunction with the companies Arradiance Inc. and Photonis. Laser tests performed have demonstrated that the modified device shows no quantum efficiency loss out to 3 C/cm^2, an improvement of 6-8 times with respect to the previous measurements on similar devices. This corresponds to an integrated luminosity of about 30 fb^{-1}, sufficient for operation in 2014. Further planned improvements are expected to yield at least a factor of three improvement in lifetime, which, when combined with a more finely pixellated detector, will allow operation in the high luminosity regime, where an annual integrated luminosity of 300 fb^{-1} is anticipated.

The MCP-PMT output pulse is processed by the read-out system, which must digitize the signal and interface with the ATLAS trigger and data acquisition system, while maintaining the excellent time resolution. A pre-amplifier board has been designed and built based on the low noise, high radiation-tolerant GALI-39+ amplifier. The amplified signal is processed by a constant fraction discriminator (CFD), which corrects for variations in pulse height that would otherwise dominate the timing resolution. Coincidences of the CFD output signals will be used to form Level-1 triggers, which can range from a simple "proton in detector" trigger, to more sophisticated triggers that select mass bins (based on the distance of the proton from the beam), to complex triggers that correlate the proton and calorimeter information. The trigger signal will also be used to gate the reference clock signal, based on a SLAC designed phased-lock-loop feedback system that maintains the jitter of the clock on the few ps scale. This gated clock signal will thus only be recorded for events with protons, avoiding the loss of information in the digitization stage that arises when the occupancy is too high. The gated CFD and timing signals are digitized by a TDC board which utilizes the HPTDC chip (high precision time-to-digital converter) and will interface with the ATLAS read-out system.

Tests of the prototype detector and electronics chain (except for the reference clock which has been independently validated and the trigger which is under development) indicate the approaching
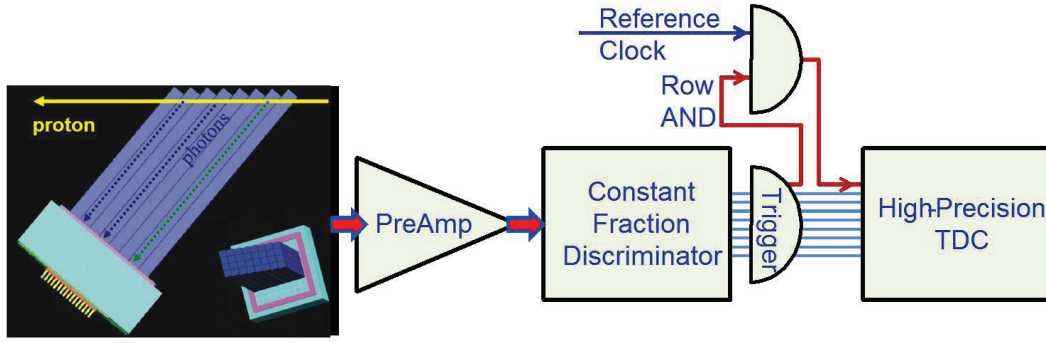
Figure 5.8. A schematic diagram of the fast timing system as described in the text.

of a time resolution of 10 ps, corresponding to a vertex resolution of about 2 mm which would reject about 95% of the overlap background (see Fig.5.2). Final R&D efforts to complete the electronics chain and extend the MCP-PMT lifetime are in progress, with a full prototype system test planned in 2012, such that, as described in the following, a prototype of the timing system could be deployed in 2014.

Finally, as a general reference, in Table 5.1 a summary of the performances and of the design specifications for the various parts of the AFP detector (including the timing part) discussed in this chapter is reported.

Acceptance	Tagged proton momentum loss ξ	$0.02<\xi<0.2$
	Typical di-photon mass acceptance	$300<\sqrt{(\xi_1\xi_2 s)}<1200$ (GeV)
Si Tracker	Spatial Resolution	$\sim 15~\mu$m
	Angular Resolution	$\sim 1~\mu$rad
	Reconstructed Mass Resolution	~ 5 GeV
QUARTIC	Time resolution	<10 ps

Table 5.1. Summary of the AFP detectors parts design specifications.

5.6 Proposed time scale and milestones

As described above the AFP project consists of three main parts, which are being developed in parallel: the movable beam pipe, the silicon position detectors, and the quartz timing detectors.

The installation of the movable beam pipe, cables, and other infrastructure requires a long shutdown and therefore must be installed during the 2013/2014 shutdown. During the same shutdown is foreseen also the installation of one Silicon tracker station per side and one QUARTIC timing detector per side. The Silicon tracker station will be based on the same production of 3D sensors and FE-I4 read-out chip of IBL. The QUARTIC timing detectors will belong to the prototypes realized during the R&D program from 2012 on. Both the tracker and the timing detectors will be fully instrumented for being read out in the ATLAS TDAQ. Therefore the data taking after the 2014 shutdown, will be considered as an engineering run, with the data already relevant for the physics program outlined in Section 5.1. The remaining part of the tracking detector (one station

per side) will be then installed during the winter shutdown of 2015. The winter shutdown of 2016 will be used to install the final version of the timing system (two stations per side with the removal of the two prototype stations installed in 2014), and, could also be used to upgrade the silicon detectors to increase the acceptance, if the edgeless 3D detectors (which reduce the dead area near the beam from about 200 μm to about 50μm) are ready for installation.

6. Fast TracKer

6.1 Functional overview and performance goals

Effective triggering at high luminosity is extremely challenging, especially for triggers that require track reconstruction. The problem is clearly seen in Fig. 6.1, which shows the number of hits in each silicon layer as a function of luminosity. Note that the y intercept, which is barely visible above the origin, represents all of the hits from the hard scattering process!
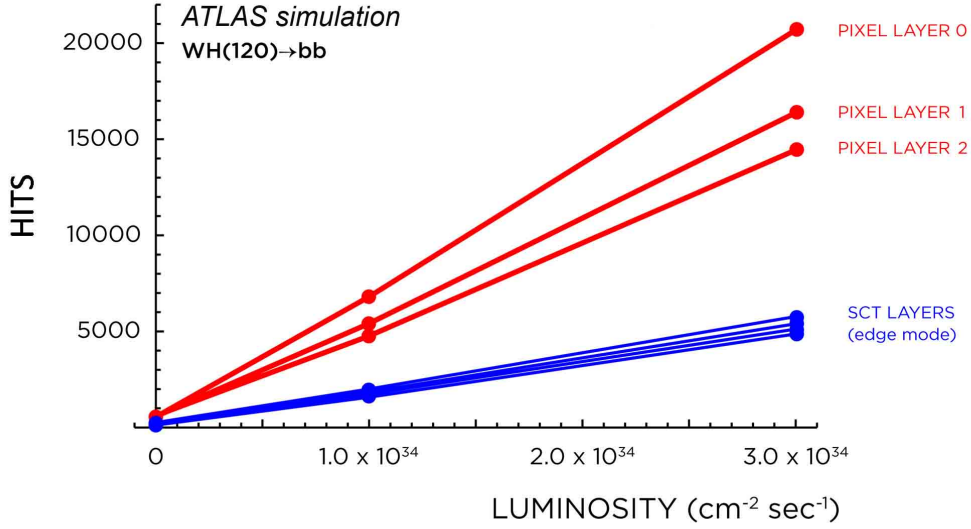
Figure 6.1. The number of hits from each silicon layer in the barrel vs. luminosity.

The FastTracKer (FTK), a descendent of the very successful CDF Silicon Vertex Trigger (SVT) [42, 43], is a pipelined electronics system that rapidly finds and fits tracks in the inner-detector silicon layers for every event that passes the Level-1 trigger. Its goal is global track reconstruction with near offline resolution at a maximum Level-1 rate of 10^5 events per second and a latency per event of less than 100 μs. This can be compared with the time to carry out full track reconstruction in the Level-2 processors which is estimated to be several hundred milliseconds at Phase-I luminosity. FTK uses 11 silicon layers over the full rapidity range covered by the barrel and the disks. It receives a copy of the pixel and silicon strip (SCT) data at full speed as it moves from the RODs to the ROSs following a Level-1 trigger, and after processing it provides the helix parameters and χ^2 of all tracks with p_T above a minimum value, typically 1 GeV/c. The Level-2 processors can request the track information in a Region of Interest or the entire detector.

FTK is a scalable processor. The system described below will work well at the LHC Phase-I luminosity of $2 - 3 \times 10^{34} \mathrm{cm}^{-2}\mathrm{s}^{-1}$. To deal with the large input data rates as well as the large number of track candidates found at high luminosity, FTK has been designed as a highly parallel system that is segmented into η-ϕ towers, each with its own pattern recognition hardware and track fitters.

6.2 System architecture

The FTK algorithm consists of two sequential steps of increasing resolution. In step 1, pattern recognition is carried out by a dedicated device called the Associative Memory (AM) which finds track candidates in coarse resolution roads. When a road has silicon hits on all layers or all except one, step 2 is carried out in which the full resolution hits within the road are fit to determine the track helix parameters and a goodness of fit. Tracks that pass a χ^2 cut are kept. If there are hits in all layers and the χ^2 fails the cut but is not extremely large, the track is refit a number of times with the hit on one of the layers dropped each time. This "majority recovery" allows for the loss of a single hit due to detector inefficiency with a random hit picked up instead.

The first step rapidly carries out what is usually the most CPU intensive aspect of tracking by massive parallelism – processing hundreds of millions of roads nearly simultaneously as the silicon data pass through FTK. The road width must be optimized. If it is too narrow, the needed size of the AM and hence the cost is too large. If roads are too wide, the load on the track fitters can become excessive due to the large number of uncorrelated hits within a road. This increases both the number of roads the track fitter must process and the number of fits within the road due to the hit combinatorics.

Because hit combinatorics increases rapidly with the number of layers, the track reconstruction is carried out in two stages. In stage-1, 8 layers are used (3 or 4 pixel layers and 4 or 5 SCT layers). Those 8-layer tracks that pass a χ^2 cut are sent to stage-2 where hits in the 3 remaining layers are added and the full 11-layer track candidates are fit.

Figure 6.2 shows a sketch of FTK, which is FPGA based with the exception of one specially designed chip for the associative memory.

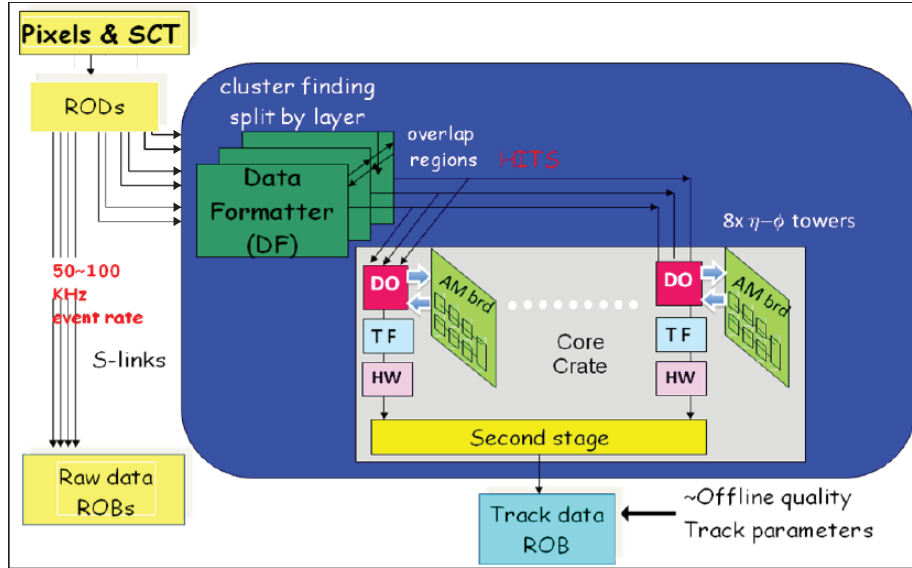**Figure 6.2.** Functional sketch of one of 8 FTK core crates plus its data connections.

The FTK input bandwidth sets an upper limit on the product of the Level-1 trigger rate and the number of silicon hits per event. In order to sustain a 100 kHz Level-1 trigger rate at luminosities up to $3 \times 10^{34} \mathrm{cm}^{-2}\mathrm{s}^{-1}$, it is necessary to organize FTK as a set of independent engines, each

working on a different region of the silicon tracker. The first step is to divide the detector into azimuthal regions. This segmentation generates some inefficiency at region boundaries that can be removed by allowing a small overlap region at the boundaries. For Phase-I luminosity, there will be 8 ϕ regions (45° wide) with an overlap of 10° to guarantee high efficiency for tracks with p_T of 1 GeV/c and above. Each region will have its own "core crate", for a total of 8 core crates working independently. Each region is further subdivided into sub-regions, corresponding to η-ϕ towers, again largely independent and with enough overlap to maintain high efficiency. The η range is divided into four intervals, and the region's ϕ range is divided again by two. The overlap in η takes into account the size of the beam's luminous region in z. Each subdivision is an independent processor with its own pattern recognition and track fitting hardware.

6.3 Description of component boards

The pixel and SCT data are sent from the detector RODs to the Data Formatters (DF) on standard ATLAS S-LINK optical fibers. The mezzanine cards in the RODs will be replaced by dual-output ones which have two optical outputs that transmit identical data to the normal DAQ ROSs and to the DFs. This is accomplished by sending the output of the serializer within the FPGA to two drivers, each of which feeds an optical transmitter.

The pixel and SCT data are received by the Data Formatters (DF) which perform cluster finding, one-dimensional in the SCT and two-dimensional in the pixels. The barrel layers and the forward disks are grouped into logical layers so that there are 11 layers over the full rapidity range. The cluster centroids in each logical layer are sent to the sub-region processors. Since the pixel and SCT RODs are not organized in η-ϕ towers, the DFs are not either and thus are not in the core crates. Rather each DF must share its output with nearby DF boards so that one fiber pack can be sent to the Data Organizers (DO) in each FTK sub-region. The need for high-speed interboard data transfer within the DF crates makes ATCA the natural choice because of its powerful data-sharing backplane. Physically a DF board consists of a motherboard and input mezzanine cards. The latter contain S-Link receiving hardware and an FPGA that will be programmed to do the cluster finding.

The stage-1 functions within an FTK sub-region processor are pattern recognition, fitting the 8-layer track candidates, and duplicate track removal. The heart of the pattern recognition is the Associative Memory (AM) board, while the other functions are carried out in the auxiliary card (AUX) behind it. Two such AM-AUX pairs cover a sub-region.

When a hit from the DF enters the AUX card, it is received by the Data Organizer FPGA. The DO is a smart database where full resolution hits are stored in a format that allows rapid access based on the pattern recognition road ID and then retrieved when the AM finds a road with the requisite number of hits. In addition to storing hits at full resolution, the DO also converts them to a coarser resolution (superstrips) appropriate for pattern recognition and sends them into the AM board on serial links through one of the AM rear connectors.

The AM boards contain a very large number of preloaded patterns or roads corresponding to the possible combinations for real tracks of a superstrip in each silicon layer. These are determined in advance from a full ATLAS simulation of single tracks using detector alignment extracted from real data. An important recent advance allows for roads whose width varies by detector layer. This improves the performance of the system by better utilizing the available pattern space and reducing the number of fake track candidates.

The AM is a massively parallel system in that all roads see each silicon hit nearly simultaneously. When a road has found the requisite number of hit layers, the AM sends the ID number for that road back to the DO. Physically the AM board consists of a motherboard and 4 large mezzanine cards (LAMB) that each hold 32 AM chips. These custom ASICs are HEP-specific content-addressable memory chips that will each contain approximately 50,000-100,000 patterns, the number needed for operation up to a luminosity of 3×10^{34} cm^{-2} s^{-1}. The large increase in pattern density has been achieved by designing in a 65 nm process. The prototype chip has gone through a CERN ASIC review and will be submitted in January 2012. Each of the 4 LAMBs on an AM board has dedicated serial links to one of 4 mezzanine cards on the AUX card that contains a DO, a track fitter (TF), and duplicate track removal (Hit Warrior or HW).

When the AUX receives a road ID from the AM, the DO immediately fetches the associated full-resolution hits and sends them and the road ID number to the Track Fitter (TF). The TF is implemented in an FPGA and can fit tracks at an average rate of 1 per nanosecond. It achieves this extraordinary speed by replacing a traditional fit with a set of simple calculations. For a small region of the detector, in our case one physical silicon module in each layer, each helix parameter and each component of the χ^2 can be calculated by an equation that is linear in the local hit position in each layer. The constants in the equation are calculated in advance and stored in on-chip memory. Fitting a track is thus just a series of integer multiply-and-accumulate steps which can be done extremely quickly in a modern FPGA.

Duplicate tracks share most but not all of their hits. They occur when a track has non-associated nearby hits, either noise or coming from another track. If the replacement of real track hits by other hits still produces a satisfactory χ^2, then there will be duplicate tracks. The Hit Warrior function (HW) is applied after track fitting and reduces the duplicate track rate by keeping only the best track among those that share at least a specified number of hits. The best can be decided based on track χ^2 and by other track characteristics such as the presence of a hit in the innermost pixel layer.

The output of the HWs on the 4 AUX mezzanine cards, consisting of the tracks that pass a χ^2 test, are merged and then sent to an FTK 2nd-stage board, each of which handles data from 4 AUX cards. In addition to the 8-layer tracks, a 2nd-stage board also receives the hits in the remaining 3 silicon layers from a DF. The 2nd-stage board extrapolates the 8-layer track into each of the other layers and looks for hits close to the track. The final fit uses hits from all 11 layers in another linear calculation. Once again a χ^2 cut is applied, duplicate tracks are removed, and the remaining tracks are sent out of the core crate.

The final set of FTK boards communicates with the rest of the High Level Trigger (HLT) system. The tracks are most conveniently accessed by the HLT if they are stored in an η-ϕ array. Since the core crates each cover a ϕ region, data from each of the 8 core crates can be handled separately. A final FTK board will receive the tracks from several core crates, process the data from each core crate independently and in parallel, organize them in the η-ϕ array, and then send them to ROSs with the usual ATLAS protocol. An ATCA crate is being considered for the final boards because it would allow easy transfer of all the tracks in an event to other boards in the crate to carry out auxiliary functions, for example rapid determination of all of the primary vertices in an event.

All interboard data transfer in FTK uses a common format, and all FTK boards carry out

common monitoring functions. Key among these is the Spy Buffer system in which each FTK function has deep circular buffers for both input and output. When an error condition occurs in the system, all boards freeze their Spy Buffers so that data from the offending event can be read into a monitoring computer for analysis. The availability of data from each step of FTK processing allows for rapid identification of board malfunctions.

6.4 Simulated performance

The performance of FTK was simulated using samples of single particles, QCD dijets, inclusive W's, associated production of a W and a Higgs boson with the latter decaying into quark pairs, and vector-boson fusion into a Higgs boson that decays into a pair of τ leptons. Both in-time and out-of-time pile-up were included for luminosities up to $3*10^{34} \text{cm}^{-2}\text{s}^{-1}$ (an average of 75 pile-up events per beam crossing). These samples were used to estimate data flow through the FTK, FTK execution time, tracking efficiency and resolution, and performance in tagging b-jets, identifying τ-jets, and triggering on single muons.

The single-particle efficiency is shown for muons in Fig. 6.3 as a function of pseudorapidity. The plateau efficiency is lower than for offline tracking because of the more stringent requirement we place on the number of hits on a track. The dips seen in the figure at the transition regions between the silicon barrel and disks have now been reduced by more than a factor of 2 by allowing more missed layers in those regions. FTK track resolution is compared to offline tracking in Fig. 6.4. Curvature and impact parameter are shown; the agreement is similar for the other three helix parameters.
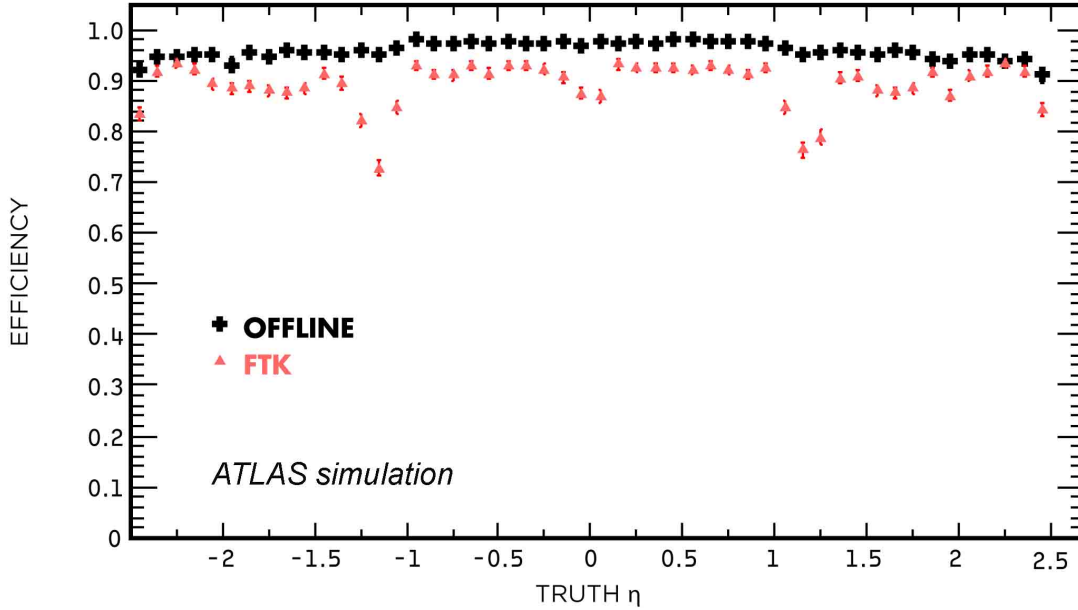
Figure 6.3. FTK track efficiency compared with offline tracking as a function of pseudorapidity.

The tagging of b-jets is shown in Fig. 6.5 for an average of 75 pile-up interactions per beam crossing. FTK performance is not as good as in offline tracking, although the selection criteria for FTK tracks have not yet been optimized. Moreover, since the tracks will be available at the start of
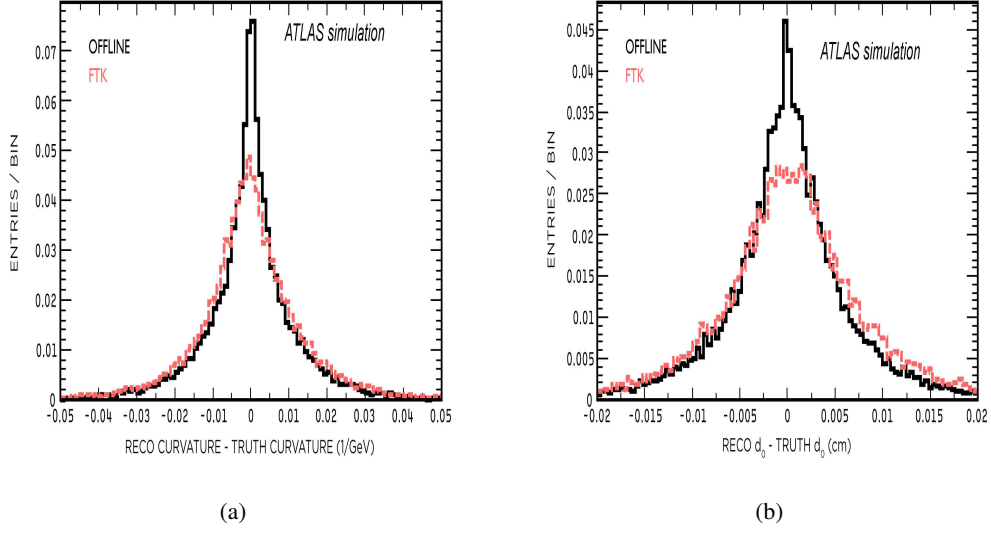
Figure 6.4. Curvature (a) and impact parameter (b) FTK resolution compared to offline tracking.
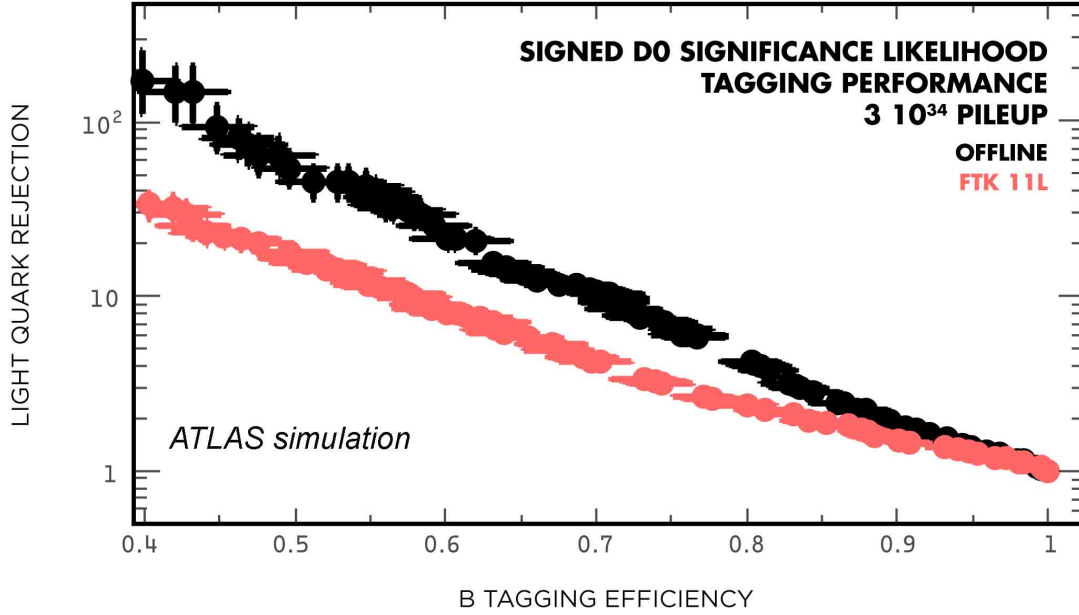
Figure 6.5. Comparison of *b*-tagging with a simple d_0-significance tagger for an average of 75 pile-up interactions per crossing.

Level-2 processing, some of the freed-up level-2 execution time can be used for more sophisticated *b*-tagging algorithms which will further improve light-quark rejection.

The efficiency for identifying 1-prong and 3-prong τ-jets in the same high-luminosity environment is shown in Fig. 6.6 for an operating point where the probability of misidentifying a light-quark jet is $\sim 10^{-3}$.

(a)   (b)
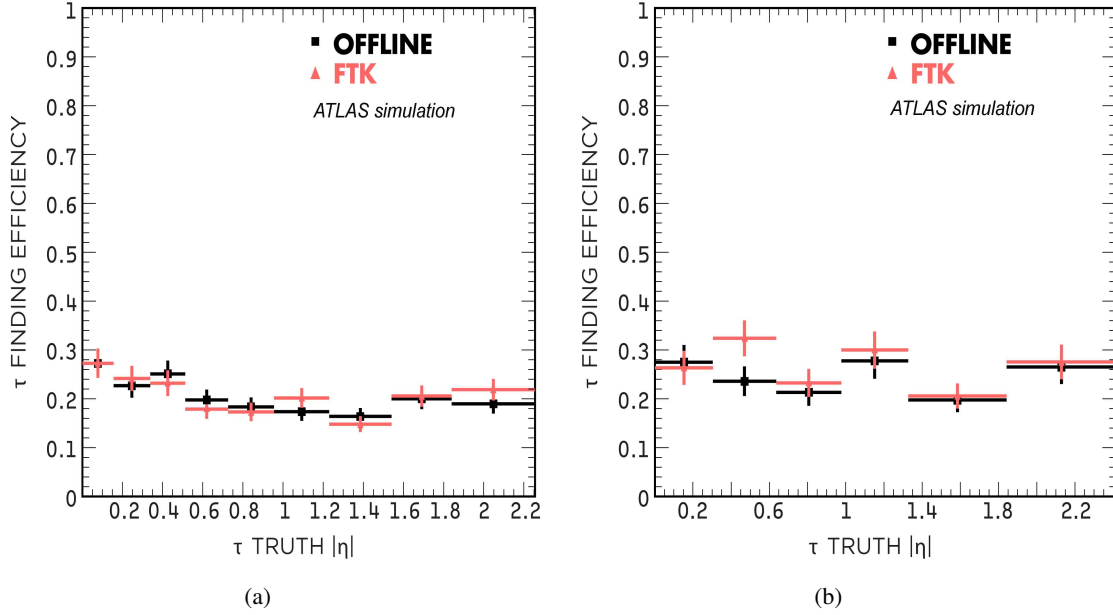
Figure 6.6. τ identification efficiency for 1-prong (a) and 3-prong (b) decays for an average of 75 pile-up interactions per crossing.

Single muon triggers rely on an isolation requirement to maintain a low p_T threshold. At high luminosity, the traditional calorimeter isolation fails because the calorimeter integrates over all the pile-up interactions. Track isolation solves the problem if a $|\Delta z_o|$ cut is used to select only those tracks that point to the lepton primary vertex. Figure 6.7 shows the efficiency for muons from W decay as a function of pile-up for both calorimeter and tracking isolation. The latter remains flat out to very large pile-up.

The enormous timing advantage that FTK provides at high luminosity is shown in Fig. 6.8. On the left is execution time per jet Region of Interest with the current level-2 tracking software. For events that require b-tagging of all high-p_T jets, the total time required is at least several hundred milliseconds for Phase-I pile-up conditions. On the right is the execution time for global tracking in FTK which averages 25 microseconds, 4 orders of magnitude less.

6.5 Schedule

A FTK Vertical Slice (VS) that covers a few small $\eta - \phi$ regions of the detector is being commissioned at CERN. Its goals are to test integration into the ATLAS TDAQ environment, check real-time performance with data, and serve as a test bed for prototype FTK boards. The VS is beginning with existing boards that will be replaced later by final prototypes.

The hardware design of all FTK boards is underway, and the simulation is regularly updated to keep pace with the design choices. The goal is to have prototype boards and a Technical Design Report by the spring of 2013.
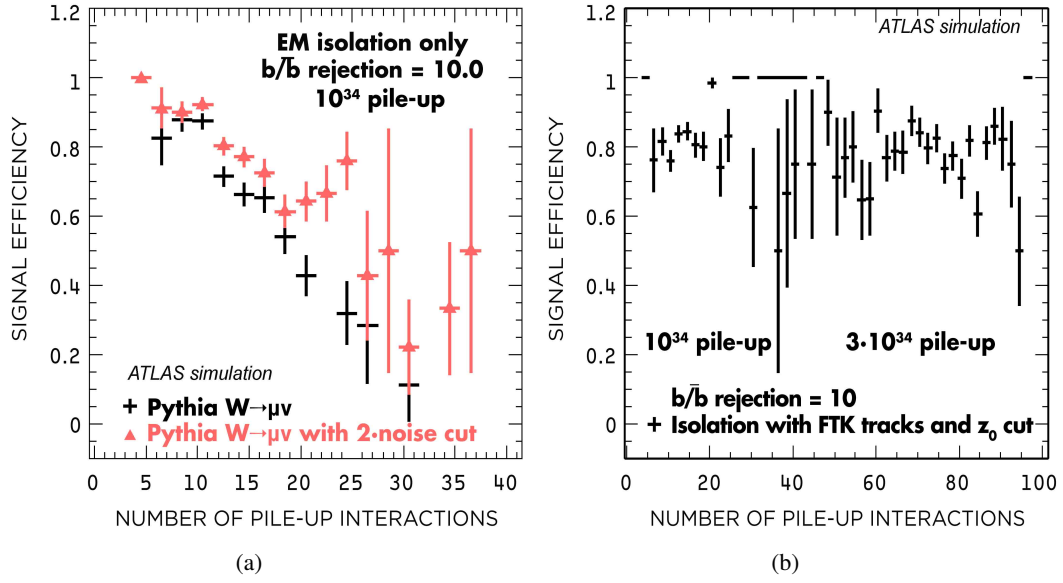
Figure 6.7. Isolated muon efficiency using (a) EM calorimeter with two cell energy thresholds or (b) tracking isolation with a $|\Delta z_\circ|$ cut as a function of the number of pile-up interactions in the event. The isolation cut is selected to provide a $b\bar{b}$ rejection factor of 10.
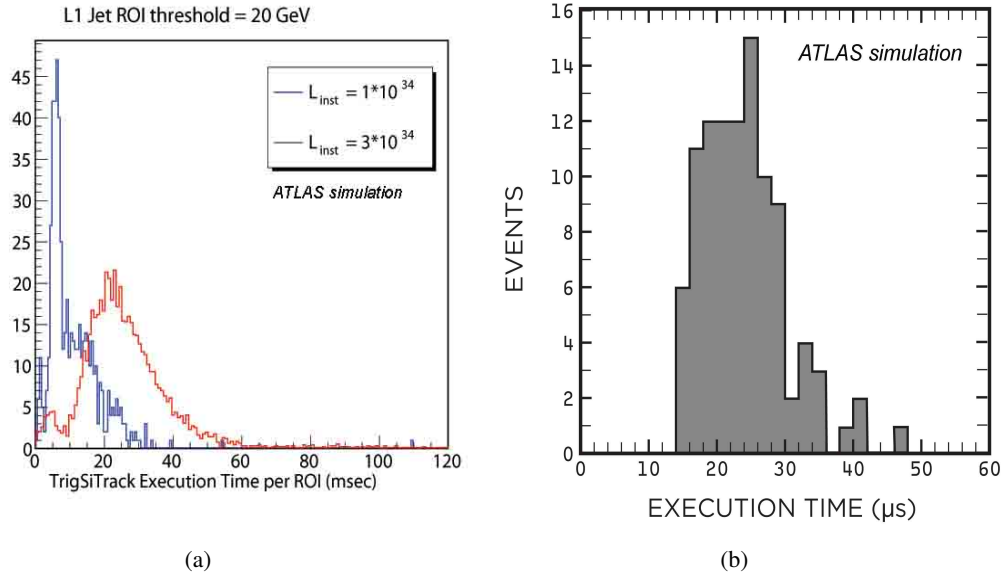
Figure 6.8. The execution time for software level-2 track reconstruction in one jet Region of Interest (a) and for global FTK track reconstruction (b) at a luminosity of $3 \times 10^{34} \mathrm{cm}^{-2}\mathrm{s}^{-1}$.

7. Trigger and Data Acquisition System

The ATLAS Level-1 trigger system searches for signatures from high-p_T muons, electrons/photons, jets, and τ decaying into hadrons, and also selects events with large missing transverse energy and large total transverse energy. Reduced-granularity information is used from a subset of detectors: for high-p_T muons, these are the Resistive Plate Chambers (RPC) in the muon barrel, and Thin-Gap Chambers (TGC) in the muon end-caps; all the calorimeter sub-systems contribute to triggers on electromagnetic clusters, jets, τ, E_T^{miss}, and large total E_T.

Two detector changes are important for the upgraded Level-1 trigger in Phase-I. The replacement of the muon small wheel will help to maintain Level-1 muon trigger (L1Muon) performance in the forward region against the expected large cavern backgrounds; and a partial replacement of the LAr on-detector electronics will enable higher-granularity calorimeter data to be available to the Level-1 calorimeter trigger (L1Calo). Upgrades to the Level-1 trigger electronics will use these data to improve performance at higher pile-up and provide increased trigger flexibility. ATLAS does not plan major architectural changes to the current detector read-out and data acquisition, so the Phase-I trigger must operate within the current detector pipeline latency limits of ~2.5 μs, using the spare ~0.5 μs latency (20 bunch crossings) in the present system. The maximum average Level-1 Accept rate will not exceed 75 kHz (upgradeable to 100 kHz).

The Phase-I Level-1 trigger is organised as three subsystems, as illustrated in Fig. 7.1. The functions are described below.
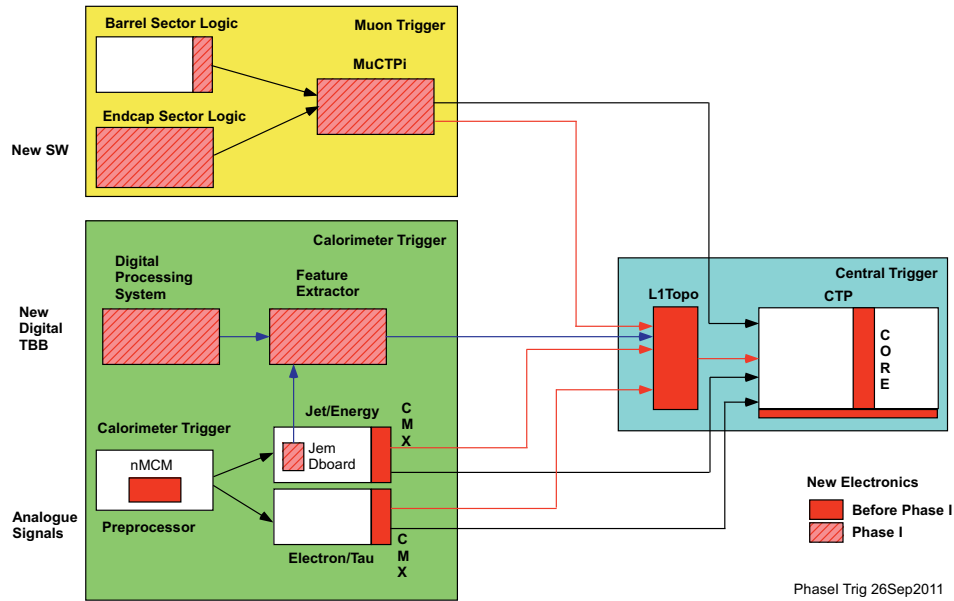
Figure 7.1. Diagram of Level-1 trigger system at Phase-I. Developments installed before Phase-I are shown in red, those added at Phase-I are shown shaded.

Significant software modifications are needed to use tracking information from FTK in the

High-Level Trigger (HLT), and to adapt to the modified Level-1 strategy.

The present detector timing infrastructure and Detector Control System (DCS) will remain for Phase-I running.

7.1 Level-1 calorimeter trigger

7.1.1 Preprocessor

At the heart of the preprocessor subsystem are four-channel Multi-Chip Modules (MCMs), which convert analogue input signals to time-aligned, calibrated and noise-suppressed digital outputs. A replacement MCM is being developed for installation before Phase-I, with new FADCs to provide faster digitization with low noise, and with the remaining functions implemented in a single FPGA. This provides flexibility to improve the digital filter and BCID algorithms, and the possibility of increased granularity at Phase-I for signals into the Jet/Energy processor.

7.1.2 Cluster processor and Jet/Energy processor

The main change to the existing Cluster Processor (CP) and Jet/Energy Processor (JEP) subsystems is the provision of topological trigger information for a new Topology Processor (L1Topo). Tests have shown that the present crate backplanes can run without error at four times their current bandwidth, enabling the transmission on the real-time data path of the coordinates as well as individual threshold bits for all identified Regions of Interest (RoIs). In the existing Cluster Processor Modules (CPMs) and Jet/Energy Modules (JEMs), modified FPGA firmware will collect and format the additional information, which will then be sent both to the real-time path and to the DAQ for readout.

In the present system, CPM and JEM output data are collected in each crate by Common Merger Modules (CMMs). These modules cannot be modified to handle the quadrupled data volume, so they will be replaced by new eXtended Common Merger (CMX) modules capable of receiving and processing the higher-speed real-time data, and equipped with high-speed optical links to the L1Topo. The CMX modules will be installed before Phase-I with firmware transparently reproducing the existing CMM signals to the Central Trigger Processor (CTP). Studies will also be made on the cost-benefits of a single CMX module in the system performing limited topological processing using the RoI information data from all other CMX modules.

For Phase-I, the mezzanine modules on the JEMs will be upgraded to higher electrical input and optical output bandwidth, offering the possibility to transmit hadronic data to the new digital processor system.

7.1.3 Digital processor system and feature extractors

The present inputs to the L1Calo are analogue trigger tower signals, the majority covering an area in $\eta \times \phi$ of 0.1×0.1. On-detector analogue summations over depth, η, and ϕ are carried out to form these signals. In the case of the LAr detector, Layer Sum Boards (LSB) and Tower Builder Boards (TBB) perform the summation.

As an intermediate step towards a possible fully digital calorimeter system foreseen for Phase-II, new LAr TBBs and LSBs will be developed to provide additional trigger information at finer granularity and in digital form via radiation-hard optical links. Options being considered include four

separate depth samples of granularity 0.1×0.1 and higher-lateral granularity, e.g. 0.025×0.1 in $\eta \times \phi$ in the second sampling layer. Implementation details are given in Chapter 4. The analogue sums provided to the current L1Calo will be maintained.

As shown in Fig. 7.1, the analogue signals will continue to be used by the upgraded CP and JEP subsystems. The new finer-grain LAr signals will be processed through a new real-time data path — the Digital Processor System (DPS) and Feature Extractor (FEX) — allowing for more refined electron identification algorithms and potentially improved Jet and E_T^{miss} calculation. The DPS will mirror the functionality of the existing Preprocessor: reception of optical signals, digital signal time alignment, digital filtering to extract E_T contributions and pedestal subtraction, calibration, noise thresholding, and serial transmission to the following FEX stage by optical link.

In the FEX subsystem, sliding-window algorithms will be performed over the $\eta \times \phi$ region of calorimetry. The internal structure and algorithms of these modules will be defined by future R&D: hadronic data from the JEM mezzanine boards will be used if available at a granularity of 0.1×0.1; RoI data will be transmitted from the CMX modules to the FEX if latency permits, as the data volume forwarded to L1Topo could be considerably reduced. In the absence of either of these options, the FEX will perform shower shape analysis for all possible RoI positions, forwarding the results to L1Topo for matching with the CP subsystem output.

The addition of hadronic data from the upgraded JEM mezzanine modules to the electromagnetic data from the DPS will allow hadronic isolation to be used for electron identification in the FEX, as well as jet-finding algorithms with finer calibration and granularity. Several options are currently under consideration; in one option the FEX contains separate jet and electron processor modules, while another option performs jet processing in a separate subsystem (Jet FEX). In both options the jet algorithm would receive the hadronic layer information from the upgraded JEM and the electromagnetic layer either directly from the DPS or from the electron FEX modules. Simulation studies are underway to determine the benefits of a jet trigger with higher granularity.

7.2 Level-1 muon trigger

One of the major changes to the ATLAS detector during the Phase-I shutdown will be the replacement of the muon chambers located at the end-cap inner station, the muon small wheel. The primary motivation for the change is to maintain tracking performance under the large cavern background of neutrons and photons. Details of the detector options for the new chambers are given in Chapter 3.

The track segment information available from this new detector will also be used to reinforce the current Level-1 muon trigger. For muons with p_T above 20 GeV, initial studies indicate that the trigger rate in this region could be reduced by more than a factor of ten compared to the current system, without loss of trigger efficiency. The new detector, illustrated in Fig. 7.2, will provide trigger capability in the range $1.3 < \eta < 2.4$. Although the choice of technology has not yet been made, the new detector must provide a position and angular resolution of reconstructed track segments better than 60 μm and 0.3 mrad, and the segment finding efficiency should be as good as the present MDT chamber at low intensity.

For L1Muon, an angular resolution of 1 mrad is needed in this region to achieve the best p_T resolution. This will be obtained from the combination of track angle measurements by the new small wheel and the TGC big wheel. Related improvements to L1Muon electronics include new

sector logic for the end-cap muon chambers, and a new muon to the CTP Interface (MUCTPI) that will, among other things, allow muon RoI coordinates to be extracted and processed in real time for the L1Topo.

7.2.1 Sector logic

The track segment information from the new small wheel will be combined with information from the current L1Muon. An example data flow diagram is shown in Fig. 7.3.

The boxed area for the current system in Fig. 7.3 corresponds to a part of the current L1Muon end-cap trigger based on the TGC big wheel. TGC chamber hit information is sent to a low-p_T coincidence matrix, where 3 out of 4 coincidences among two doublets and 2 out of 3 coincidences in the triplet are formed. In the next step, further coincidences are made between two low-p_T trigger outputs in the high-p_T coincidence matrix.

The trigger RoI is sent to the sector logic with an $\eta \times \phi$ granularity of 0.03×0.03. The deviation of the track angle with respect to the straight line from the interaction point is also provided to the sector logic and used to determine the transverse momentum of the trigger candidate. Trigger information is processed independently between η (wire readout) and ϕ (strip readout) up to this stage.

Hits from the new small wheel are processed in parallel to those from the TGC big wheel, which takes 1 μs to reach the input of the new sector logic. Information from the new small wheel should reach the sector logic within the same delay to avoid adding latency compared to the present L1Muon end-cap trigger system.
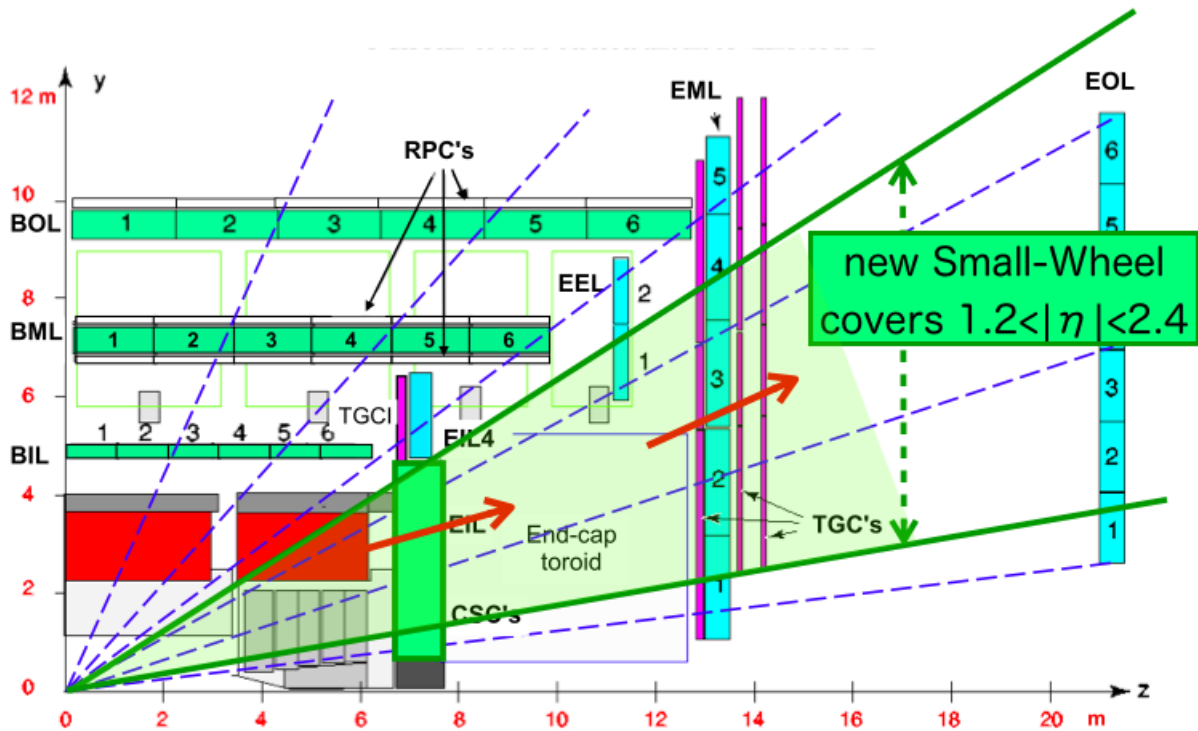
Figure 7.2. Muon new small wheel

The trigger decision is performed in two steps due to the limitation of the size of FPGA. In the first stage, a coincidence between high-p_T output of TGC big wheel from the wire and strip passing the highest threshold (e.g. L1MU20) and the track segment in the new small wheel is required. Before making the coincidence, the following cuts are made:

- the dR between RoI found in the TGC big wheel and the location of track segment in new small wheel is less than 0.1 ; and

- the angle difference (dθ) between the track segment in the new small wheel and the trajectory of an infinite momentum particle is less than 10–20 mrad, depending on the material in front of the small wheel due to the multiple scattering.

In the second stage, the p_T of the track is calculated from the angular difference between the track segments in the new small wheel and the TGC big wheel.

Many charged particles are generated near the beam pipe at the z position of the end-cap toroid magnet, then bent into the TGC big wheel with an angle similar to high momentum particles from the interaction point. The first stage above rejects the majority of such fake tracks. Particles coming from upstream of interaction point also penetrate the small wheel, but are eliminated by applying the angle cut for the track segment found in the new small wheel. In the second stage, the sharpness of the turn-on curve is enhanced due to the improved momentum resolution. A momentum resolution of 15% at p_T of 20 GeV/c is expected.

7.2.2 Muon-CTP interface

The final stage of L1Muon processing is provided by the MUCTPI. A new MUCTPI is needed to receive data from the upgraded end-cap sector logic, and to provide muon information to L1Topo as well as to the CTP. As currently implemented, the new MUCTPI will count the number of muon candidates for each p_T threshold and send this multiplicity information directly to the CTP. It will
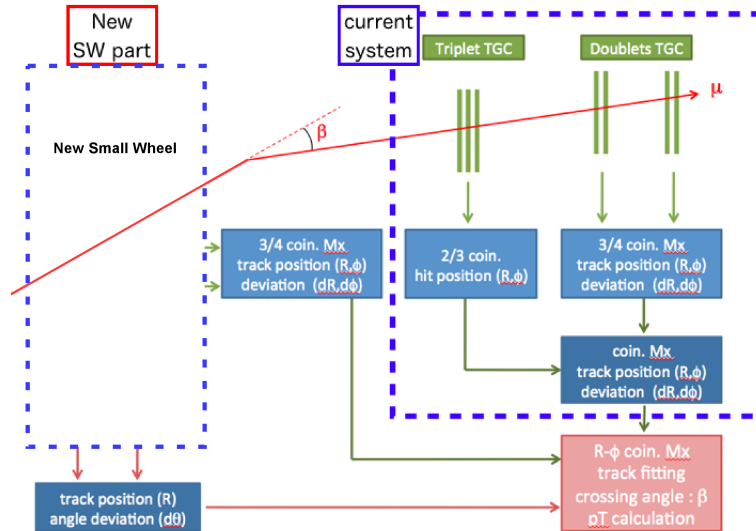
Figure 7.3. Block diagram of the new Level-1 muon trigger logic

also extract, compress, pre-process and send muon RoI information to L1Topo for every bunch crossing, concentrating the data from all of the (> 200) muon trigger inputs and handling trigger overlaps.

One potential implementation would see the merging of four of the existing octant (MIOCT) modules into a single board, which would produce p_T threshold and RoI data for each of the eight highest-p_T muon candidates per bunch crossing. This scenario would imply a total of four outputs from the new MUCTPI system to the topological processor. The final design will necessarily need to be based on detailed physics input, e.g. the average number of muon candidates expected at Phase-I and Phase-II luminosity.

The module will use high-speed serial optical inputs in place of the present bulky cable plant. The adoption of an optical interface for the new MUCTPI will allow more information to be transferred from the sector logic, for example data for more than two muon candidates, more p_T thresholds, or additional bits indicating the quality of muon track. The new implementation will also foresee additional inputs from the MDT chambers and thus be forward compatible with options currently being studied for Phase-II. The new MUCTPI could possibly also include improved overlap handling, adding more flexibility and possibly spanning octants; use of calorimeter data for muon isolation, as an alternative to doing this in the sector logic or the topological processor; and muon-only topological algorithms, such as computation of di-muon invariant mass. These would be complementary to the global topological processor, as they would be based only on muon information.

The current interface between the L1Muon barrel sector logic and the MUCTPI will be replaced with a new one providing the same functionality but using optical outputs; a total number of 64 VMEbus boards have to be replaced.

Despite the additional processing requirements and the adoption of higher-latency serial optical inputs, initial studies indicate that the latency of the new MUCTPI system could be kept within the time of eight bunch crossing.

7.3 Level-1 topological and central trigger

For Phase-I, the topological information to be processed will be the η and ϕ coordinates, threshold bits and possibly transverse energy of RoIs identified by the L1Calo and L1Muon subsystems. High-speed optical links will gather and concentrate the RoI data into single processing units capable of executing algorithms with the full event topology.

The enhancements to the Level-1 trigger described above will require more trigger bits to be processed by the CTP to produce a Level-1 Accept. Additional input and processing capacity will be added to the CTP to accommodate the increase.

7.3.1 Topological processor

While the emphasis in Level-1 trigger developments is to retain low lepton thresholds, topological algorithms are used in the Level-2 trigger. For selections based on di-lepton triggers, jet topology, muon isolation or MET isolation, these typically achieve rate reduction factors of 2–5 in the channels concerned. Studies indicate that significant benefits are retained in the Level-1 environment. It is with this in mind that the RoI detail are extracted from the Level-1 processors and transmitted to the L1Topo.

Two sets of topological algorithms are currently being explored:

- Those which improve single lepton performance. This category includes the matching of electron information from the CP and the FEX, the use of jets to provide muon isolation, and the separation of electron and jet signatures (an isolated energetic electron also fires the jet trigger).

- Those which use multiple trigger objects, for example identifying W or Z leptonic decay candidates by computing transverse mass.

A variety of topological parameters are under study for physics performance and hardware implementation. These include $\Delta\phi$, $\Delta\eta$, ΔR, Jet E_T^{miss}, effective mass and transverse mass, aplanarity, and sphericity. Use of topological algorithms at Level-1 has the potential to introduce bias into physics results, so a topological trigger needs a low rate of non-topological triggers to monitor the trigger behavior.

A technology demonstrator of the L1Topo is currently under construction, and it is expected that a production system could be installed during before Phase-I. Firmware and algorithms will be adjusted to suit the LHC luminosity.

7.3.2 Central trigger processor

The Central Trigger Processor (CTP), illustrated in Fig. 7.4, is housed in a single 9U VMEbus crate, and consists of four types of module: CTP_MI which receives LHC timing signals, CTP_IN which receive the L1Calo and L1Muon input signals, CTP_ CORE where the main combinatorial logic is performed, and CTP_OUT which provides the trigger output signals to the detector. Additional modules include CTP_Mon responsible for monitoring and CTP_CAL which controls calibration processes.
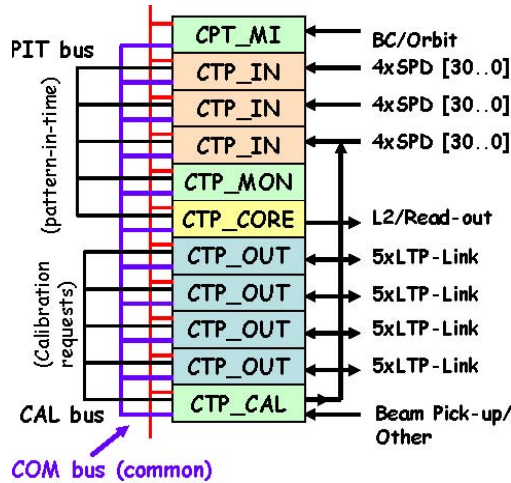

Figure 7.4. Central Trigger Processor structure

The inter-module PIT-bus will be doubled in speed and a new CTP_ CORE module produced, both before Phase-I. The additional input data will be handled both by running the input modules at higher speed, and through direct optical inputs to the CTP_ CORE module. The new CTP_ CORE

will implement more items allowing the trigger menu to be expanded. These capabilities will be matched by an improvement in trigger monitoring logic. They will be available before Phase-I and will be useful as soon as they are implemented.

7.4 High-Level trigger

The High-Level Trigger (HLT) comprises the hardware and software of the Level-2 and Event Filter (EF) farms. The farms consist of around 2300 PCs running the trigger selection software. The movement of event data is performed by the data flow system that includes the Read-out System (ROS), the Event Builder and network infrastructure. Event data are read from the detector following a Level-1 Accept and are stored in the ROS pending a Level-2 decision. The event data are stored in fragments, with the data from each sub-detector distributed over several ROS. The ROS serves event data to the Level-2 processors and, for events accepted by the Level-2 trigger, to the Event Builder (EB). The EB assembles the data fragments prior to processing by the EF. Events passing the EF are sent to long term storage.

The HLT selection is achieved by identifying specific physics objects such as electrons, photons, muons, tau leptons and jets. The HLT selection software consists of: reconstruction algorithms (calorimeter clustering and tracking in the muon spectrometer and inner detector); selection algorithms, which identifies the physics objects; trigger steering software which configures and controls the HLT reconstruction and selection algorithms. The Level-1 and HLT configuration is defined by trigger menus which specify the trigger conditions to be satisfied to accept the event, the physics objects upon which the trigger conditions are based and the reconstruction and selection steps leading to the creation of the physics objects.

Several changes are needed to adapt the HLT selection software for higher luminosity and for the upgrades to the detector and Level-1 trigger. The HLT steering software will be upgraded to provide greater flexibility to optimize the event processing to minimize average execution times and prevent excessive times in the case of events with many RoIs. The HLT tracking code will be upgraded to limit the rise of algorithm execution times as events become more complex due to the higher levels of pile-up and cavern background, affecting the muon detector, as luminosity increases. In addition to minimizing the average per-event processing time, it is important to prevent very long execution times which would otherwise cause time-outs. The HLT muon code must be adapted for the new small muon wheels and the ID tracking must be adapted for the insertable B-layer and to use FTK information. The FTK will provide initial track parameter information which can be used to guide (seed) the HLT tracking that will add TRT information and refine and refit the tracks.

The HLT selection algorithms will need to be upgraded to achieve the required rate reduction. This upgrade is needed because of the greater complexity of events with high levels of pile-up, and since the upgraded Level-1 will take over some of the selection steps currently performed at the HLT. The new selections will make increased use of multi-object and topological triggers (for example selections based on geometrical cuts and the reconstructed invariant mass of intermediate-state particles). The order of reconstruction and selection steps will be optimized to achieve the earliest possible rejection and so reduce the average per-event processing time and the rate of data-requests to the ROS. It is likely that Level-2, EB and EF functionality will be combined in the same processor and this will allow a greater integration of Level-2 and EF selections with a

potential saving in overall execution times. The availability of FTK track information provides the possibility to perform track-based selections (including B-jet tagging, primary and secondary vertex reconstruction, and invariant mass reconstruction) from the start of the HLT selection.

7.5 Data acquisition

Given the detector changes described above, and that the maximum Level-1 Accept rate will not increase, it is expected that the current DAQ/HLT architecture will be able to meet the needs of the experiment at a peak luminosity of 3×10^{34} cm^{-2} s^{-1} with respect to Level-1 rate and bandwidth. Further studies and additional experience of operating the current systems at increased luminosity are required to clarify the demands that the High-Level trigger selection may impose on the system.

Although it is not proposed to change the architecture of ATLAS readout (ROD and ROS) in Phase-I, some changes to the implementation may be required to meet the challenges that running at 3×10^{34} cm^{-2} s^{-1} pose. A new version of the readout link (ROL), the point-to-point link between the RODs and ROS, whose current implementation runs at 160/200 Mbyte/s, may be needed to provide increased bandwidth for new detectors, e.g. new small wheel, and the readout of the FTK.

The physics demands of ATLAS have pushed the operation of the ROS a factor of two beyond its original design specification. The performance is currently network bandwidth limited (2x1Gbit/s). This limit constrains those Level-2 trigger chains that, for example, require all event data from a specific sub-detector. To remove this limitation and re-establish some of the operational headroom originally provided in the system, the dataflow network will be upgraded to a 10 Gbit/s Ethernet connection at the ROS and, via link aggregation, 100 Gbit/s Ethernet connections to a central core. This upgrade would also allow the rate at which events are built to be increased. A sub-component of the ROS is the ROBIN, a PCI-X card. By the Phase-I shutdown, it is anticipated that PCI-X slots will no longer be deployed in sufficient numbers on commercially available computers, having been replaced by PCI-express. The ROBIN will be re-designed and re-implemented to follow this technological trend and support readout links of higher speeds than the current 160/200 Mbyte/s.

By the end of Phase-I operations, the custom VMEbus electronics implementing the Region of Interest Builder (RoIB) will have been in operation for sixteen years, well beyond the generally accepted operational life of custom electronics. Two upgrade paths are currently being investigated. The first aims to exploit the continued advances in server technology. It is expected to be able to implement the RoIB functionality in one or more servers housing one or more custom mezzanine cards that handle the small data packets arriving at up to 100 kHz from the Level-1 system. This will remove or reduce the dependency on custom electronics and introduce additional operational flexibility into the system. The alternative of re-implementing the RoIB in modular electronics will also be investigated as a back-up solution.

Other upgrades to the ATLAS detector imply the deployment of additional DAQ/HLT hardware. Additional ROLs and ROSs (including ROBINs) will be deployed to readout the new small wheels. Similarly, plans presented in this document to upgrade the Level-1 calorimeter trigger and associated LAr electronics implies additional channels to be readout, i.e. additional ROSs and ROBINs. For most detector systems increasing the bandwidth of the ROL will not increase the readout bandwidth, as the necessary changes cannot be made to the RODs. Such systems are con-

sidering the deployment of additional ROLs, and therefore additional ROSs and associated ROBINs will have to be deployed.

As well as hardware, some of the software technologies deployed in the DAQ/HLT system will have become obsolete and in some cases no longer meet the requirements on the DAQ/HLT system for operations at 3×10^{34} cm^{-2} s^{-1}. In addition, the computers on which the DAQ/HLT software is deployed will have significantly evolved compared to that for which it was originally designed, i.e. single-core versus multi-core CPUs. Similarly, the operating system software deployed on the hardware will have evolved and will necessitate the upgrade of the DAQ/HLT software to allow the full potential of the hardware to be exploited, and in some cases to make it possible to just run the system software. Therefore, following a period of technical evaluation, particularly in the areas of online databases, information sharing and expert systems, new open-software technologies will be selected and where necessary the DAQ/HLT software re-designed and implemented.

8. Phase-I Shutdown Scenario and Work Organization

8.1 Requirements

The LHC project is scheduling a long shutdown (LS2) in 2018 to allow the detectors and the accelerator to face under optimal conditions the LHC data taking period from 2019 to 2021, where the 350 fb^{-1} integrated luminosity, baselined in the initial project planning, should be accumulated. The cavern (UX15) will be accessible for about 13 months starting in December 2017. The ATLAS collaboration will make use of this period to open the detector and to allow a series of modifications and improvements, which are the subject of this LOI document (Phase-I upgrade).

The mechanical operations required by the Phase-I upgrade are mainly concerned with the trigger system and affect largely two sub-detectors: the muon small wheels and the calorimeters.
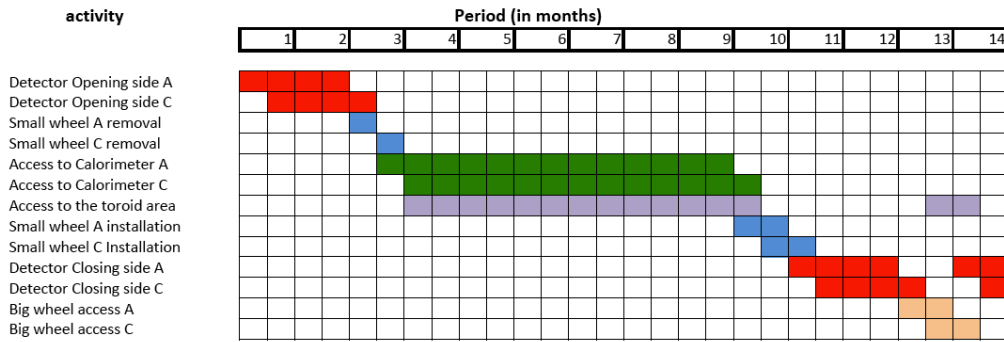
Figure 8.1. Items assigned to the various activities over the 14 months of access

The muon small wheels will be fully rebuilt and the new assemblies will become available at the pit surface about four months after the start of the shutdown. Therefore the old ones will need to be removed from the pit and brought to the surface for storage in a dedicated buffer zone at CERN for an initial radioactivity cool-down until they can be decommissioned. The decision if to reuse or not the existing JD shielding disk is still pending, with ALARA[1] considerations being part of the decision process. Before lifting it to the surface all services must be carefully disconnected and if necessary refurbished for the next installation. Because of the time criticality of this operation, the removal of the small wheels will get priority at the beginning of the shutdown period over all other activities.

To allow enough time (3 months) for connection and tests of the new wheels, the new assemblies will be lowered in position onto the ATLAS main rails approximately five months after the initial removal or as soon they are fully ready and tested on the surface.

The calorimeters crew (both technologies) will work intensively on their front-end electronics, which sits in crates on the front faces of the LAr cryostats or, for the Tile calorimeter, inside the electronics drawers. This implies that all calorimeters front faces will need to become accessible for working on the electronics, and this as soon as it is possible.

---

[1]As Low As Reasonably Achievable risk of radioactive exposure

All other activities in the ATLAS pit should be performed in the background of these two critical operations. The only other task which requires prime time, relates to the access to the muon big wheels, which are not fully accessible when the toroid end-caps are in the open position. If this is proven necessary, it will be possible to schedule it at the end of the shutdown period, when the muon small wheels are installed and the end-cap toroids are in running position.

8.2 Operation layouts and configurations

Figure 8.1 shows a schematic view of the time assigned to the various prime time configurations. It is clear that all operations are very concentrated in time and the schedule will be very challenging. To arrive to the main configuration (Fig. 8.2), the forward shielding will be moved to the surface, the beam pipe will be open and vented, the last beam pipe section which includes the LUCID detector moved to the surface and the end-cap Toroids will be moved to the side in their garage position. The end-cap calorimeters will be moved by about 3 m longitudinally, allowing full access to the frond-end crates and electronics of both barrel and end-caps.
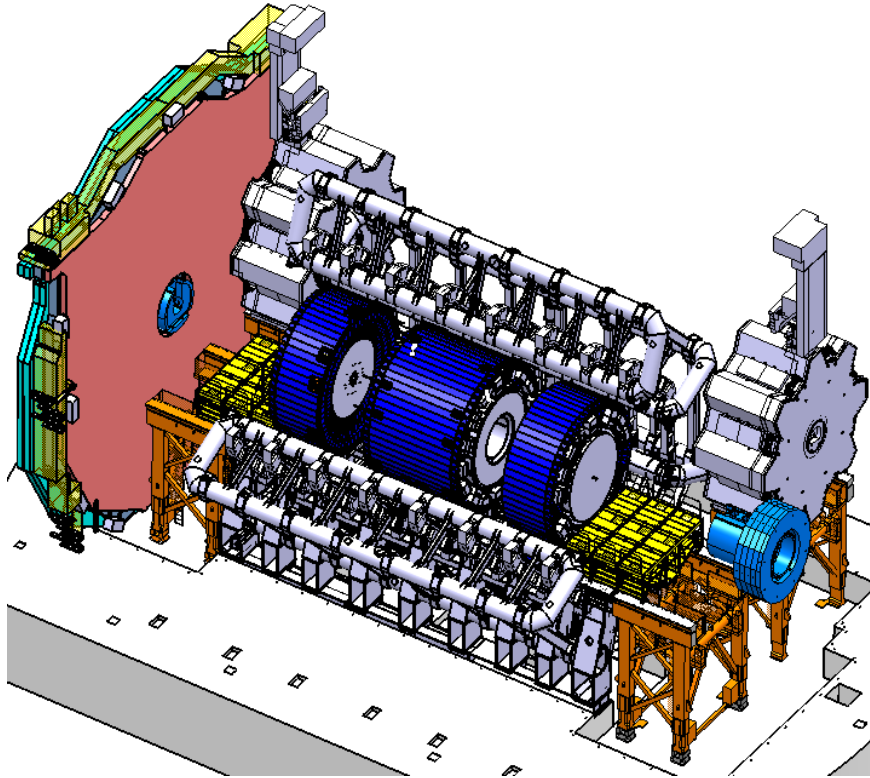
Figure 8.2. Detector configuration during LS2 shutdown, with both small wheels removed

All these opening activities are not new and will be exercised in many occasions over the coming years, and by then the ATLAS technical coordination will have acquired quite some experience. The most critical and risky operation is the removal of the small wheels which will need to be brought to the surface. In the LS1 shutdown (ATLAS Phase-0 in 2013-2014) also this operation will be exercised and the specific technique should already be acquired and qualified. The plan is

to arrive to this main working configuration after 11 weeks of activity, working partially in 2 shifts or extended shifts (from 7 am to 9 pm).

8.2.1 Calorimeters access

All calorimeter front faces will be accessible through a dedicated scaffolding with access from the lowest toroid sector (#13) and through an emergency exit from sector 1. A new set of access tools is under preparation and will be deployed and exercised already in winter 2011. Access will be granted to typically 4 people working at the same time on each of the four partitions. The Tile calorimeter crew shall be able to extract completely all drawers if necessary, bring them to the cavern ground floor for additional repair and tests or to work on the electronics drawers in situ if more suitable. Access to all drawers will be granted by scaffolding modifications following an agreed plan of work. The LAr calorimeter crew shall be able to access all electronics crates and power supplies, and shall be able to exchange and/or introduce electronics cards. As of today there are no plans to open the ID endplate, and therefore the main users of these four partitions are the calorimeters intervention crews. Because of the expected activation level around the beam pipes, the region within 1 m radius will be protected and excluded from any access in normal conditions (see paragraph 8.3).

8.2.2 Small wheels removal and installation

The removal and reinstallation of the small wheels represents the most complex and risky step in the entire process. The entire procedure, which makes use of a special transport frame developed in the years 2007-8 for the main installation step of the initial detector, will be fully exercised in the LS1 2013-2014 shutdown when one small wheel will be removed and raised to the surface, in order to have enough space for the IBL ("insertable b layer") installation. The plan is to remove the two small wheels as soon as possible in LS2, bringing them to the surface buffer zone, to dismount the present muon wheel and to dispose of it according to the CERN nuclear waste disposal procedure, to reshape the present JD shielding elements where necessary and to finally install and fully qualify the new small wheels. Typically the process on the surface should not last more than 5 months. The new small wheels, ready for installation, should be made available at Point 1 at the beginning of the LS2 shutdown period, in order to account for a safe three months of ready for installation milestone. It is expected that for each wheel the removal or re-installation procedure, including de-cabling or re-cabling, will last about two weeks. During that period, access to UX15, at least in the concerned half of the cavern, will not be granted without proper restrictions. At the surface, all operations will have to be agreed through a proper ALARA analysis and a dedicated team trained on how to precisely act in such a complex situation (see paragraph 8.3) will be established.

8.3 ALARA strategy

Just before opening for LS2, the LHC to have delivered to ATLAS an integrated luminosity exceeding 50 fb^{-1}. Taking into account a safety factor of 20% and a typical 2 months cooling time, an estimation of the radiation dose, for workers active near to the beam pipe or working on the dismounting the small wheel shielding, can be calculated. Figure 8.3 shows the expected level of activation, translated in a dose rate mostly for gamma rays, as a function of the spectator position

for the main configuration and for a radius of maximum 2 m from the beam line. These estimations already take into account the fact that the present iron beam pipes in 2013 will be replaced with an aluminum one, with a clear effect (40%) on lowering the expected activation dose rate.
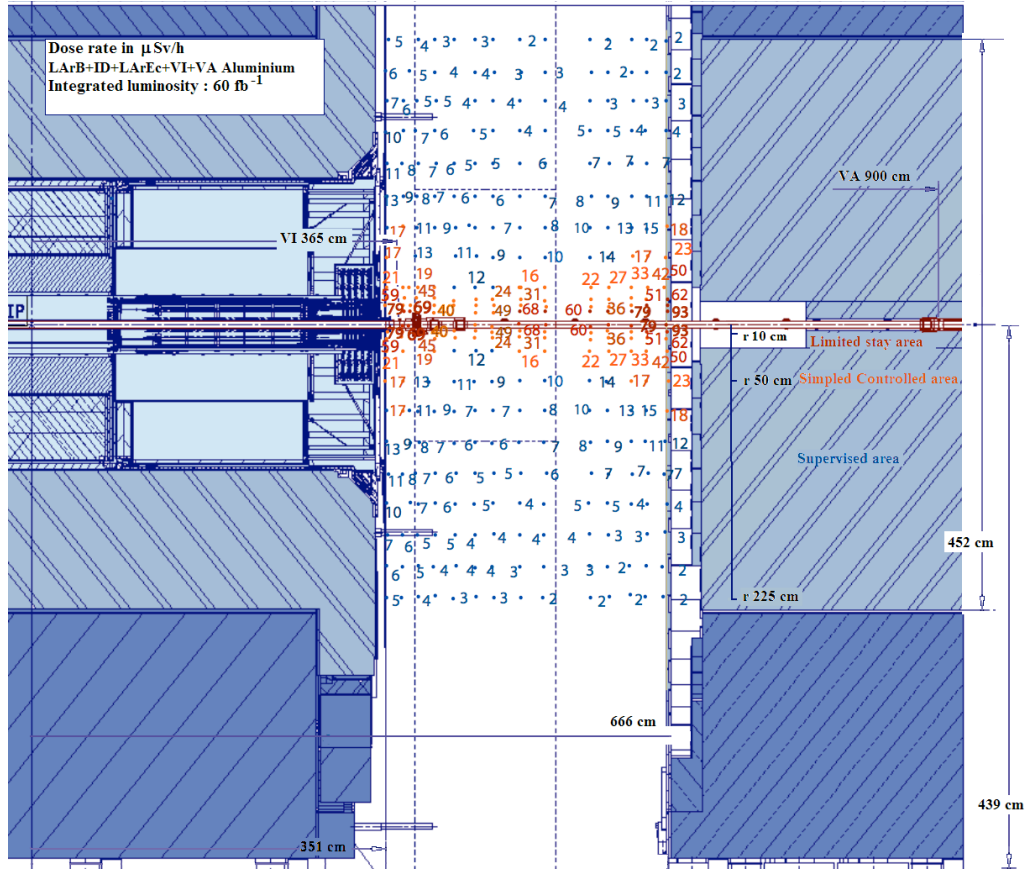
Figure 8.3. Expected radiation dose during the installation activities close to the beam pipe in the area between barrel and end-caps calorimeters

The present legislation and common sense suggest to minimize the exposure of workers to radiation in any case. The maximal dose rate a professional worker should be allow to take at CERN is 2 mSv/month, for a maximum exposure per year of 6 mSv. The ATLAS collaboration would like to make sure that nobody gets exposed to more than 0.2 mSv/month under any circumstance. This means that people working very close to the beam pipe, where the dose rate is expected to be of the order of 5-7 μ Sv/h shall not be active for more than 40 hours/month. This implies that additional shielding elements must be introduced around the beam pipe to protect active workers. A physical line all around the beam pipe at a radius of about 1 m, will be in any case installed to prevent coming closer. On top of this, it is foreseen to add about 16 mm of tungsten-loaded thick plastic shielding, which should absorb about 40% of the gamma rays energy. This would lower the dose rate and allow people to work safely for more hours.

Similar precautions will be taken at the surface of the JD, near to the conical shielding elements and the bore of the stainless steel tube. The radiation dose, in particular for some inner shielding

elements, can be substantial and particular care must be given to the entire process. The inner bore of the stainless steel cylinder will need a protective shielding cover to be installed in situ before raising the SW assembly to the surface, The region within 1 m from the beam pipe, which radiates ~ 30 to $70\,\mu$ SV/h will need to be physically protected with additional shielding barriers to prevent any close access.

The success of such an enterprise will not just be based on shielding and access limitations, but will go through a proper analysis and preparation of the work and a proper follow-up of the activity in situ, to avoid errors and unnecessary exposures. The ATLAS safety group will actively be involved in the actual working process in situ and will actively define the necessary boundaries and limitations to the exposure of personnel in situ. All activities will have to be prepared in detail and analyzed beforehand.

8.4 Schedule constraints and work organization

Thirteen months of access represent a challenging requirement for this enterprise. Out of the 13 months, at least 5 will be spent to open and close the detector. Assuming that one needs, in the end, at least 1 month to absorb eventual delays and run all necessary quality tests before closing the detector, one is left with no more than 6 months to perform the actual work of installation of the new small wheels, work on the calorimeter front faces and eventually act on the muon big wheels. Figure 8.1 summarizes all the above operations within the schedule.

To achieve such an ambitious goal, the work must be well prepared at the surface, all elements tested and qualified and all installation and the subsequent commissioning activities must be perfectly mastered and followed-up. As ATLAS does during all access periods, all activities will be subdivided in work packages, which must be formally analyzed, understood and accepted by the ATLAS central safety team. Only work packages accepted and signed by the safety team will be implemented and people assigned to it will be granted access via the new work management system (IMPACT) just deployed in the winter 2011.

To avoid disseminating potentially radioactive material throughout the entire UX15 cavern, all material exiting the zone at a radius smaller than the outer radius of the Tile calorimeter (excluding the Tile drawers) will be brought by crane to the surface inside a dedicated basket, temporarily deposited in the dedicated buffer zone and properly measured and identified. On a case by case basis the radio-protection team will define its further destination and possible usage. This way of acting is already part of the ATLAS working procedures established since the beginning of operations in 2008. Near to SL2 all this will acquire even more importance and particular care will be given to train and instruct the community on all these necessary procedures.

9. Expected Physics Performance of Upgraded ATLAS at Phase-I

The ATLAS detector upgrades proposed in the previous chapters have been placed under careful scrutiny by identifying physics channels that will represent a challenge for the Level-1 trigger during the LHC Phase-I running period. Simplified simulations of the performance of the new muon small wheel (Chapter 3), of the improved Level-1 granularity of the second layer of the EM section of the LAr calorimeter (Chapter 4) and of the AFP (Chapter 5), have been used to estimate the signal efficiencies as well as the background Level-1 rates. These studies were performed as a function of the instantaneous luminosity or, equivalently, of the average number of pile-up events expected. Several physics channels were used for this purpose, whose implications on performance represent different scenarios of new physics. The event samples were generated and then processed through the standard ATLAS full-simulation and reconstruction software.

The rationale was to show for most of these studies that the ability to trigger efficiently at Level-1 on a single electron or muon with p_T thresholds as low as 20 GeV, maintains the present ATLAS performance, even in the much harsher environment expected during the Phase-I period. This strategy is relevant to a wide range of physics processes that might prove to be central to the physics aims of the LHC this decade.

One possibility that is explored here is the case of WH associated production for a light Higgs in the range not yet excluded by data. In this channel, triggering on the e or μ from the W decay should allow a least biased detection of the Higgs boson, so that the different decay branching ratios can be measured accurately and therefore the Higgs couplings computed. The capability of triggering on single low-p_T leptons can be helpful also in the case in which no Higgs boson will be found, since it will allow ATLAS to select with high efficiency boson-boson scattering (WW, WZ, ZZ), where new physics is expected to emerge.

A large-statistics sample of low-mass Higgs (m_H = 120 GeV) decays in the $\gamma\gamma$ channel was used as a case study to determine how low the thresholds for two EM Level-1 triggers could be kept in a high-pileup environment.

In the case of the AFP, the physics program is twofold. On the one hand tagging both scattered protons in double-pomeron exchange (DPE) at the LHC gives access to a deeper understanding of the model of diffraction and to the possibility of constraining the structure of the pomeron in a completely new kinematic domain. On the other hand, anomalous quartic gauge couplings between γ and W or Z bosons would allow ATLAS to probe Higgsless or extra-dimension models with two-orders of magnitude higher sensitivity than achievable by the present ATLAS detector. For these purposes, samples of dijet and W-boson production in DPE events were generated, as well as quartic-gauge anomalous coupling events. The systems in the central ATLAS detector (up to $|\eta| = 5$) were subject to full simulation, while an ad-hoc fast tracking was used for protons in the LHC beam-line magnetic elements (FPtracker program, [44]).

Finally, a broad program of supersymmetry searches and measurements becomes kinematically accessible with the increased luminosity. Sensitivity to supersymmetry models was considered for direct production of gauginos and sleptons, as well as for squark and gluino cascade decays. Efficiency and acceptance for many of the key discovery and model-discriminating signatures becomes compromised if lepton thresholds are increased, particularly for general SUSY models with compressed spectra.

Other BSM models will be addressed in the near future and reported in the corresponding Technical Design Reports.

9.1 Large statistics measurement of low-mass Higgs-boson properties

In the physics scenario in which the Higgs mechanism is the correct one for explaining Electroweak Symmetry Breaking and the origin of masses, and under the assumption that the Higgs boson has been discovered using 50 fb^{-1}, the Phase-I running will focus on determining precisely the Higgs couplings to different fermions and bosons, in order to assess in a definite way its nature. Additionally, the rare decays $H \rightarrow \mu\mu$ with a cross-section of 15 fb, and maybe $H \rightarrow \gamma Z \rightarrow \gamma\ell\ell$ with a cross-section of 3 fb, could first become accessible in Phase-I with 300 fb^{-1} [45]. In the following, we will focus on precise Higgs couplings measurement, since this poses the strongest constraints on the design of trigger upgrades for Phase-I. To exploit fully the factor 10 gain in statistics provided by Phase-I, one should aim at proposing a trigger design that preserves as much as possible the present efficiency, and therefore low thresholds, for all production channels.

Higgs Production Channel and Decay	Cross-Section [pb]	Branching Ratio	Events/fb^{-1}	Significance for 30 fb^{-1}
$gg \rightarrow H \rightarrow \gamma\gamma$	53	0.002	20	8
VBF ($H \rightarrow \tau\tau$)	4.4	0.07	2	6
VBF ($H \rightarrow bb$)	4.4	0.7	1	3
WH/ZH ($H \rightarrow bb$)	1.7/1.0	0.7	5	5

Table 9.1. Summary of signal yields and sensitivities for various SM Higgs channels at $\sqrt{s}$ = 14 TeV and m_H = 120 GeV, for $L = 3 \cdot 10^{33} cm^{-2}s^{-1}$ scenario and 30 fb^{-1} updated according to recent NNLO prediction estimates.

In Table 9.1 expectations are shown for $\sqrt{s} = 14$ TeV and $m_H = 120$ GeV for some key Higgs-production channels that are most promising for the measurement of Higgs couplings [45, 46, 47]. The $\tau\tau$ and bb final states give a slower increase in significance with luminosity, mainly due to lower trigger efficiency (limited already at Level-1 by bandwidth) and slightly worse reconstruction efficiency in the presence of higher pile-up. As hinted by the results shown in Table 9.1 for 30 fb^{-1}, the goal for the trigger design should be to keep accumulating the already limited Higgs signal yield. This is mandatory in order to deepen the understanding of the Higgs mechanism. Production modes like $gg \rightarrow H \rightarrow \gamma\gamma$ allow not only a precise measurement of $H\gamma\gamma$ coupling, but also precision in measuring $\Gamma_{H \rightarrow WW}$, at the price of introducing some theoretical assumptions. Additionally, the Htt coupling can be measured, by comparing the rate of $WH\gamma\gamma$ and $H\gamma\gamma$ (relying on gluon-gluon fusion as being the main production mechanism). Vector Boson Fusion and Z/WH processes where Higgs decays into $\tau\tau$, WW and bb, can be combined to obtain a precise measurement of $\Gamma_{H \rightarrow \tau\tau}/\Gamma_{H \rightarrow WW}$ and $\Gamma_{H \rightarrow \tau\tau}/\Gamma_{H \rightarrow b\bar{b}}$, which probes the nature of the Higgs boson in a model independent way. It should be noted that the Z/WH channel , due to the presence of a lepton in the W/Z final state, will become, with increasing pile-up, of similar or larger importance than the VBF channel, for measuring precisely decay rates of Higgs to fermions or bosons.

9.1.1 $H \rightarrow \gamma\gamma$ and the advantage of a higher EM calorimetry granularity at Level-1

The increase in granularity at Level-1 of the second layer of the LAr EM calorimeter (see Chapter 4) allows low thresholds to be maintained for combined electro-magnetic triggers. This allows building new selection variables that are closer to the offline ones and therefore allows a significant reduction of the Level-1 rate due to background processes, while keeping a high efficiency at low E_T thresholds. This is shown in Fig. 9.1, where the Level-1 quantity $rCore_{L1}$, defined as the energy deposited in a 3×8 over a 7×8 array in the 2nd layer of the EM calorimeter by using a digit scale of 256 MeV (see Sections 2.3.2 and 2.3.4), is plotted for the $H \rightarrow \gamma\gamma$ and background samples. Requirement of two EM18 clusters, isolation[2] and $rCore_{L1} > 0.93$, provides 98% efficiency for the $gg \rightarrow H \rightarrow \gamma\gamma$ signal selected by the offline analysis[3], with a 2 kHz Level-1 output rate. As shown in Table 9.2, without the increased granularity, the Level-1 rate would be 8 kHz, for comparable Level-1 thresholds and isolation.

Level-1 trigger	Eff$_{H \rightarrow \gamma\gamma}$[%]	Rate [kHz]
Two $E_T^{EM} > 18$ GeV	100	26.4
Two $E_T^{EM} > 18$ GeV & isolation	98.5	7.7
Two $E_T^{EM} > 18$ GeV & isolation & $rCore_{L1} > 0.93$	98.0	2.0
Two $E_T^{EM} > 18$ GeV & isolation & $rCore_{L1} > 0.93$ (LSB = 1 GeV)	98.2	4.7

Table 9.2. Efficiencies with respect to the offline selection for $H \rightarrow \gamma\gamma$ production and Level-1 rates. The results were obtained with full-simulation events with $\mu = 46$. An energy least significant bit of 256 MeV has been used for the calculation of $rCore_{L1}$ for all lines in the table, except for the last one which is obtained with the present 1 GeV least significant bit.

This result was obtained using full simulation samples with average pile-up $\mu = 46$. The power of the offline analysis is reduced by the presence of high pile-up. As an example, the isolation required of the photons cannot be maintained as tight as in the current run. Nonetheless, thanks to the low trigger thresholds allowed, the loss of signal in this channel is small and does not compromise the final goals and the sensitivity shown in Table 9.1 for lower luminosities.

It should be noted that the capability of running a two-EM cluster Level-1 trigger without prescaling is extremely important also for the gluon-gluon fusion processes $H \rightarrow WW \rightarrow ee\nu\nu$ and $ZH(Z \rightarrow ee)$.

9.1.2 WH and ZH final states

The inclusion of the new muon small wheel (see Chapter 3) and the increased LAr EM granularity at Level-1 will allow keeping under control the single-muon and single-electron Level-1 trigger rates at low thresholds and thus avoid prescaling. As shown in Table 9.3, the proposed upgrades will allow ATLAS to reach a very high efficiency for WH events (and even more for ZH events) by

---

[2]In this chapter, the isolation requirement is defined as: $EM\_ISO \leq 3$ GeV .and. $HAD\_CORE \leq 1$ GeV .and. $HAD\_ISO \leq 2$ GeV.

[3]The absolute efficiency w.r.t. the generated sample in the kinematic range $p_T^{\gamma 1} > 40$ GeV, $p_T^{\gamma 2} > 25$ GeV, and $\eta^{\gamma 1}, \eta^{\gamma 2} < 2.37$ is 87% .
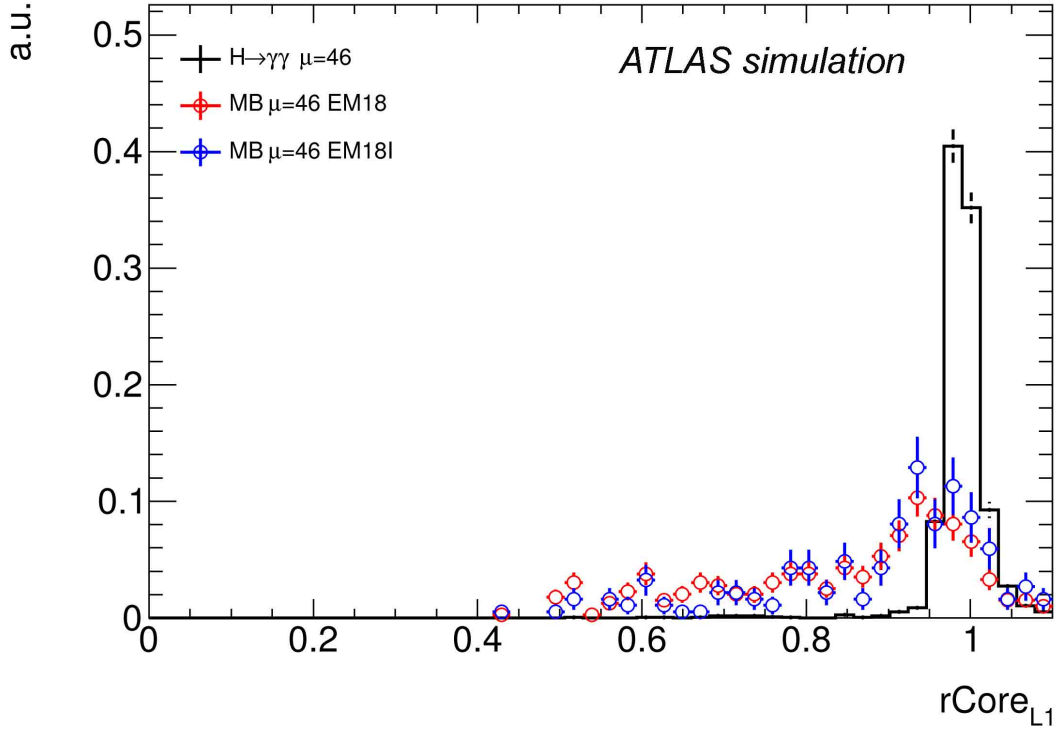
Figure 9.1. Histogram showing the $RCore_{L1}$ variable for the $H \rightarrow \gamma\gamma$ and the minimum bias MC samples as obtained using the proposed increased granularity in the Level-1 calorimeter trigger. Black: RoIs matching a photon passing the Higgs offline reconstruction selection. Red dots: Level-1 EM clusters for minimum bias events with EM cluster $E_T > 18$ GeV. Blue dots: Level-1 EM clusters for minimum bias events with EM cluster $E_T > 18$ GeV and isolation. The Higgs and background samples are at $\mu = 46$ and were processed through the ATLAS full simulations chain.

triggering on the lepton from the vector-boson decay with moderate Level-1 E_T threshold requirements (20 GeV for muons and 35 GeV for electrons).

The results of studies in full simulation and high pile-up reported in Table 9.3, clearly show the advantage of upgrading the muon and electron Level-1 triggers. In the case of the electron channel, isolation and $rCore_{L1}$ requirements allow 6.5 kHz Level-1 rates with 71% efficiency[4], while use of MET would be less efficient and at the same time much harder to control with varying pile-up conditions. In the case of the muon channel, the new muon small wheel will allow keeping the Level-1 rates at 15 kHz with WH efficiency of 78%. Similar rates could be achieved with the present muon small wheel either increasing the Level-1 muon threshold or prescaling, which would however reduce the efficiency and therefore the sensitivity of the measurements.

It is important to remark that the Level-1 trigger efficiencies shown in Table 9.3 for Phase-I proposed upgrades are very similar to what is measured for the unprescaled single lepton triggers at current luminosities and pile-up.

---

[4]Efficiencies are computed w.r.t. the electrons or muons reconstructed offline with $p_T > 25$ GeV, which is the p_T requirement presently used in ATLAS for the analyses discussed in this Section.

Level-1 trigger	Eff$_{WH}$[%]	Rate [kHz]
$E_T^{EM} > 35$ GeV	73	54
$E_T^{EM} > 35$ GeV .and. isolation	71	16
$E_T^{EM} > 35$ GeV .and. isolation .and. $rCore_{L1} > 0.94$	71	6.5
$E_T^{\mu} > 20$ GeV for old small wheel	82	40
$E_T^{\mu} > 20$ GeV for new small wheel	78	15
$E_T^{\mu} > 40$ GeV	50	18

Table 9.3. Efficiencies with respect to the offline selection for WH associate production ($H \to b\bar{b}$ and $W \to e\nu$ or $\mu\nu$) and Level-1 rates. The results were obtained with full-simulation events with $\mu = 46$.

9.2 WW, WZ, ZZ boson scattering

A major part of the LHC physics programme is the exploration of electroweak symmetry breaking at energies up to 1 TeV and beyond. Even if a light Higgs boson is discovered, it is mandatory to check if alternative theoretical mechanisms of symmetry breaking are excluded. One possibility for new physics involves models of strong interactions in the electroweak symmetry breaking sector. In this class of models, longitudinal vector boson scattering is often enhanced by high-mass resonances of unknown coupling. A Pythia implementation of the electroweak chiral Lagrangian has been modified to use amplitudes calculated for unitarized WW scattering at high energies through high-mass resonances [48].

A striking feature of vector boson scattering is the presence of two high-p_T "tag jets" in the forward regions. In the $WW/WZ \to \ell\nu jj$ channel, the hadronic decay is reconstructed from a pair of boosted jets, and the boson momenta are required to be $p_T > 200$ GeV. The largest backgrounds are $t\bar{t}$ and W+jets production. In the $WZ \to \ell\nu\ell\ell$ channel, the highest-p_T W boson candidate is used in the reconstruction, after the Z decay has been identified. The largest background is non-resonant SM $WZjj$ production.

The sensitivity to new physics in vector boson scattering depends greatly on future progress in jet and lepton reconstruction in a high pile-up regime. Such progress is difficult to estimate quantitatively, but previous benchmark studies indicate sensitivity with approximately 100 fb^{-1} data at 14 TeV [49, 50]. One key component that is straightforward to measure is the trigger efficiency for various signal scenarios. The $WW/WZ \to \ell\nu jj$ channel places the most stringent requirements on the single lepton triggers. Given that without the new small wheel triggering at $3 \cdot 10^{34}$, even at high thresholds, is impossible without prescaling, this channel also clearly benefits from such an upgrade. If these single lepton triggers are restricted in coverage or prescaled, the signal efficiency suffers, as shown in Table 9.4 .

9.3 Search for quartic-gauge anomalous coupling by scattered-proton tagging

The AFP is expected to improve ATLAS sensitivity in searches for quartic-gauge anomalous couplings between photon and W/Z bosons as a probe for extra-dimensions and Higgs-less models [51]. Integrated luminosities of 40 and 300 fb^{-1} with, respectively, 23 or 46 average pile-up events per beam crossing have been considered for the study of anomalous coupling. The case of

Scattering Process	$|\eta| < 1.3$	$|\eta| < 2.4$	$|\eta| < 2.4$ & MET>40 GeV
$WW \to \ell\nu jj$ (800 GeV)	0.41	0.50	0.49
$WZ \to \ell\nu jj$ (800 GeV)	0.42	0.51	0.51
$WZ \to \ell\nu\ell\ell$ (800 GeV)	0.56	0.71	

Table 9.4. Efficiency of different Phase-I L1MU20 single-muon triggers on vector boson scattering channels.

Cuts	Top	Dibosons	Drell-Yan	W/Z+jet	Diffr.	$a_0^W/\Lambda^2 = 5 \cdot 10^{-6}$ GeV^{-2}
timing < 10 ps $p_T^{lep1} > 150$ GeV $p_T^{lep2} > 20$ GeV	5198	601	20093	1820	190	282
M(ll)>300 GeV	1650	176	2512	7.7	176	248
nTracks ≤ 3	2.8	2.1	78	0	51	71
$\Delta\phi < 3.1$	2.5	1.7	29	0	2.5	56
$m_X > 800$ GeV	0.6	0.4	7.3	0	1.1	50
$p_T^{lep1} > 300$ GeV	0	0.2	0	0	0.2	35

Table 9.5. Number of expected signal and background events for $300\,\mathrm{fb}^{-1}$ at pile-up $\mu = 46$. A time resolution of 10 ps has been assumed for background rejection. The diffractive background comprises production of QED diboson, QED dilepton, diffractive WW, double pomeron exchange WW.

a pair of *W* bosons in the final state that decay leptonically are considered. The full list of background processes used for the ATLAS measurement of Standard Model *WW* cross-section was simulated, namely $t\bar{t}$, *WW*, *WZ*, *ZZ*, *W*+jets, Drell-Yan and single top events. In addition, more specific backgrounds containing intact forward protons in the final state such as QED $\ell\ell$, Double-Pomeron Exchange (DPE) *WW*, DPE $\ell\ell$, single diffractive *WW* productions were also simulated, although their contributions have been found to be small. All background samples were generated using Herwig++, except for single top which was generated using Pythia8. Signal samples were produced using the FPMC generator.

The analysis cuts are shown in Table 9.5. The requirement of the presence of at least one proton in each side of the AFP within a time window of 10 ps allows background reduction by a factor of about 200 (50) for $\mu = 23$ (46). The p_T of the leading lepton originating from the leptonic decay of the *W* bosons is required to be $p_T^{lep1} > 150$ GeV, while that of the next-to-leading lepton $p_T^{lep2} > 20$ GeV. Additional requirement of the dilepton mass to be above 300 GeV allows removal of most of the *Z* and QED *WW* events. Since only leptonic decays of the *W* bosons are considered, the events are selected requiring ≤ 3 tracks associated with the primary vertex (see Fig. 9.2 left), therefore rejecting a large fraction of non-diffractive backgrounds (e.g. $t\bar{t}$, diboson productions, *W*+jet, etc.) that present much higher track multiplicities. Remaining Drell-Yan and QED $\ell\ell$ backgrounds are suppressed by requiring the difference in azimuthal angle between the two leptons $\Delta\phi < 3.1$.

Figure 9.2 right displays the reconstructed mass in AFP for the irreducible QED WW back-
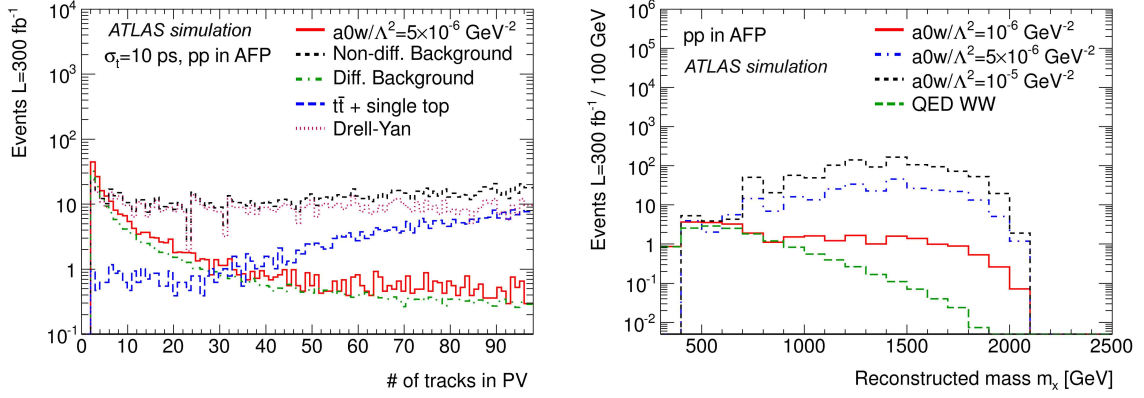
Figure 9.2. Left: Number of tracks fitted to the primary vertex for background and signal events at pile-up $\mu = 46$. Signal events present a small number of tracks fitted to the vertex. **Right:** Distribution of the mass of the W-pair system for WW anomalous quartic-gauge coupling and for the irreducible QED WW background. The mass $M_X = \sqrt{\xi_1 \xi_2 s}$ is computed using the protons tagged in the AFP, where $\xi_{1,2}$ are the proton fractional momentum losses. Anomalous coupling events appear at high mass.

	a_0^W / Λ^2 Sensitivity	
	5σ	95% C.L.
$\mathscr{L} = 40\ fb^{-1}, \mu = 23$	$5.5\ 10^{-6}$	$2.4\ 10^{-6}$
$\mathscr{L} = 300\ fb^{-1}, \mu = 46$	$3.2\ 10^{-6}$	$1.3\ 10^{-6}$

Table 9.6. Reach on anomalous couplings obtained in γ-induced processes after tagging the protons in the final state in the AFP detectors. The 5σ discovery and 95% C.L. limits are given for an integrated luminosity of 40 fb^{-1} at $\mu = 23$ and 300 fb^{-1} at $\mu = 46$ as obtained using the full MC and the background processes described in the text.

ground and for signal events produced with three values of anomalous coupling. Anomalous-coupling events are seen to appear at high W-pair invariant masses. The requirement $m_X > 800$ GeV, where m_X is the invariant mass reconstructed using the two scattered protons in the AFP, allows rejection of the backgrounds by an additional factor of four.

After the above selection, the contribution of all considered backgrounds is found to be smaller than 0.4 events for $\mu = 23$, which allows to reach the sensitivity to anomalous coupling shown in Table 9.6. In the case of $\mu = 46$, the additional requirement of $p_T^{lep1} > 300$ GeV is necessary to bring the total background and the sensitivity to a similar level even in such a high pile-up environment (as shown in the last raw of Table 9.5 and in Table 9.6.

In conclusion, full AFP simulation in presence of pile-up confirms the gain in sensitivity between one and two orders of magnitude for quartic anomalous couplings with respect to the standard (non-AFP) ATLAS methods [52], which was obtained using a fast simulation of the ATLAS detector [53]. The use of the AFP should therefore allow reaching the values expected in Higgsless or extra-dimension models [51] already with 40 fb^{-1} and moderate (pre Phase-I) pile-up. Additional sensitivity will be provided by the full Phase-I data sample, by tightening of the analysis cuts.

In addition, the AFP is expected to allow exploration of QCD and the structure of diffraction in a completely new kinematic domain of high diffractive mass and high p_T. The inclusive jet p_T cross-section with both scattered protons tagged in the AFP should allow further constraining of the gluon content of the Pomeron especially at high β, where β is the momentum fraction of the Pomeron carried by the interacting parton. The measurement of W-production asymmetry in diffractive events [54] could allow probing of different models of diffraction, to attempt to distinguish Soft Colour Interaction models, in which diffractive events are due to special string rearrangement in the final state at the hadronization stage, from Double Pomeron Exchange. Studies are ongoing on this QCD-physics program and its dependence on the level of pile-up.

9.4 Supersymmetry searches and measurements

Supersymmetry (SUSY) remains one of the most compelling extensions of the Standard Model at the electroweak scale. While the masses of the supersymmetric partner particles are not predicted *a priori*, naturalness requires that the supersymmetric partners of the top quark, the Higgs bosons and the gluino should have masses not much larger than a TeV – and therefore in the range accessible at the LHC. Supersymmetric models with kinematically accessible masses continue to provide dark matter candidates with appropriate relic densities, though there is tension developing within the highly constrained framework of mSUGRA/CMSSM [55, 56]. Models with less rigid theoretical assumptions easily allow for consistent dark matter relic densities [55, 56, 57, 58, 59] for sparticles within the reach of a $300\,\mathrm{fb}^{-1}$ LHC.

Searches by ATLAS with $\int \mathscr{L} \sim 5\,\mathrm{fb}^{-1}$ have placed $\sim$TeV bounds on the masses of the gluino and the squarks of the first two generations. These limits are, however, only valid with particular assumptions about high-scale unification and/or masses of other SUSY particles. The limits are substantially weakened: if either the squark or gluino are heavy, if the sparticle spectrum is compressed in mass space, or if the squarks are of the third generation. With integrated luminosity up to $5\,\mathrm{fb}^{-1}$, ATLAS has obtained only limited sensitivity to bottom squarks, and less still to stop squarks and to the weakly interacting gauginos, higgsinos and direct slepton production. The supersymmetric partners which naturalness arguments dictate should be light are those which couple most strongly to the Higgs field. These tend to have relatively smaller cross-sections, and so are amongst the most poorly constrained [60].

With $\sim 300\,\mathrm{fb}^{-1}$ of integrated luminosity:

- The increased parton-parton luminosity permits searches with jets and E_T^{miss} at larger values of $\sqrt{\hat{s}}$. The extent of the expected improvement can be interpolated from previous studies [61] which show that an increase in integrated luminosity from $100\,\mathrm{fb}^{-1}$ to $1000\,\mathrm{fb}^{-1}$ would increase the mass reach for squarks and gluino by about $500\,\mathrm{GeV}$.

- A crucial test of supersymmetry is the search for stop squarks $\tilde{t}$ lighter than about 1 TeV. The most sensitive decay modes depend on the model parameters, and analyses are required in a variety of channels. In some cases the dominant decay chain may be difficult to separate from background, such as in the case of loop-mediated decay $\tilde{t} \to c\,\tilde{\chi}_1^0$, or all cases in which the stop mass is near to the mass of the gauginos. It is likely that Phase-I searches will not be able to cover all possible scenarios, and for some scenarios it will be necessary to study subdominant low-statistics processes, requiring several hundreds of inverse femtobarns. Such

processes include three or four body decays [62], and the associated production of $\tilde{t}$ with b quarks [63].

- Sensitivity is obtained to direct production and decay to multi-lepton states of heavier electroweak gauginos and higgsinos with masses of order several hundred GeV. The reach depends on the gaugino couplings, and the mass hierarchy amongst the supersymmetric particles, with higher integrated luminosities allowing one to probe heavier particles, lower gaugino mixing and more compressed mass spectra.

- The supersymmetric lepton sector becomes accessible through the direct selectron and smuon production $q\bar{q} \to \tilde{\ell}^+ \tilde{\ell}^-$, for slepton masses up to about 300 GeV [64].

- Processes which are very rare in the Standard Model but common in SUSY — such as decays to same-sign di-lepton pairs — have statistical sensitivity that improves up to linearly with additional luminosity, but also require efficient leptonic triggers over a wide range of p_T.

Supersymmetry can be discovered in any of these channels. In the event of a discovery, each channel will provide complementary information about the masses, couplings and spins of different SUSY particles.

Searches for selectrons, smuons and electroweak gauginos require isolated electron and muon triggers. The momentum scale of the emitted leptons depends on the masses of the charginos ($\tilde{\chi}_i^\pm$), neutralinos ($\tilde{\chi}_i^0$) and sleptons ($\tilde{\ell}$). For a two-body decay such as $\tilde{e}^- \to e^- \chi_1^0$ the characteristic lepton momentum is

$$|p_\ell^*| = \frac{m_{\tilde{\ell}}^2 - m_{\tilde{\chi}_1^0}^2}{2m_{\tilde{\ell}}}.$$

For three-body decays such as $\chi_1^+ \to \chi_1^0 \nu_\mu \mu^+$, typical lepton momenta are $|p_\ell^*| < m_{\tilde{\chi}_1^+} - m_{\tilde{\chi}_1^0}$. Any increases in the electron or muon trigger thresholds lead to a corresponding reduction in the space of supersymmetric models to which the experiment has sensitivity. The luminosity required to measure the spin of the sleptons via direct production is typically of the order of a few hundred fb^{-1} for sleptons in the approximate range 200 to 300 GeV (Fig. 9.3 left, [65])[5].

Leptonic triggers are also centrally important in supersymmetric cascade and multi-body decays initiated by strongly interacting particles. Figure 9.3 (right) shows the effect of lepton threshold changes for a cascade decay. An existing ATLAS search at $\sqrt{s} = 7$ TeV, using a single-lepton trigger, has sensitivity to a wide range of models [66]. The plot shows the relative offline acceptance times efficiency of a $p_T > 35$ GeV offline requirement compared to a $p_T > 25$ GeV requirement.[6] For all gluino masses, increasing the lepton trigger threshold reduces the signal acceptance. The loss is particularly serious for models with small gluino–neutralino mass difference.

In general, increasing lepton trigger thresholds particularly hamper the SUSY acceptance of, and hence sensitivity to, all 'compressed' spectra where mass differences between sparticles are small.

---

[5]Some of the model points in the plot have squark and gluino masses which have since been excluded, but the direct lepton results are decoupled and remain valid in general models of supersymmetry.

[6]Based on an existing grid of model points simulated at $\sqrt{s} = 7$ TeV, and cross checked for several example points at $\sqrt{s} = 14$ TeV.
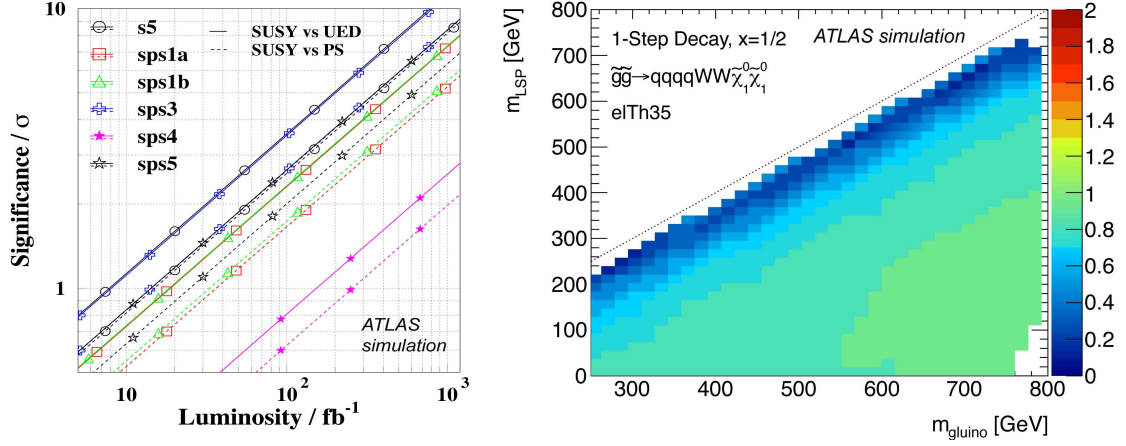
Figure 9.3. **Left**: Luminosity required to obtain significance of spin-discrimination in $q\bar{q} \rightarrow \tilde{\ell}^+ \tilde{\ell}^- \rightarrow \ell^+ \ell^- \tilde{\chi}_1^0 \tilde{\chi}_1^0$. **Right**: The ratio of the product $A \times \varepsilon$ of acceptance and efficiency for two different offline electron p_T thresholds: 35 GeV relative to 25 GeV. The SUSY model shown is an example simplified supersymmetry model in which each of two gluinos decays to $q\bar{q} + W + \tilde{\chi}_1^0$.

9.5 Topological Level-1 triggers

The present Level-1 trigger hardware can only count the number of objects above a set of thresholds. With the proposed hardware upgrade, the number of thresholds can be increased, and topological capabilities will be introduced. Specifically, regions of interest will have available at Level-1 their position in η and ϕ, and their E_T. This enormously increases the flexibility of the Level-1 trigger. This flexibility includes a considerable range of algorithms to be implemented in FPGAs, ranging from differences in η and ϕ, or ΔR, to H_T variables (sums of jets, and possibly leptons and missing E_T), and variables such as invariant and transverse mass, but also allows further evolution based on new variables invented by physics groups which formerly would have been impossible to migrate from the HLT to the Level-1 trigger. These new possibilities open up the option of signal-specific triggers which offer better operating points for physics selection in higher level triggers and offline analysis.

In order to qualify these new features several physics channels have been studied under the following conditions. A specific state is simulated with an average of 46 pile-up events per crossing, from -34 to +4 crossings around the nominal beam crossing, which could be understood as representative of a bunch in the middle of a bunch train. Then a combination of cuts is found, to reduce the minimum-bias (background) trigger rate to 5 kHz or less, which is a scale appropriate for an exclusive, process-dependent trigger within the overall 75 kHz rate. Finally, the efficiency of these cuts on the signal simulated samples is computed.

As an example the $t\bar{t}$ sample decaying to all possible final states was studied, but analyzing them only as *jets* in the Level-1 view of the calorimeter. The $t\bar{t}$ case is used as a stand-in for complex decays of high-mass states such as SUSY. Only jet RoIs are used in this analysis, whether the decay products are actually jets, electrons, or taus; muons are ignored since they leave little energy in the calorimeter. In this case a number of combinations of variables is considered. Without adding a
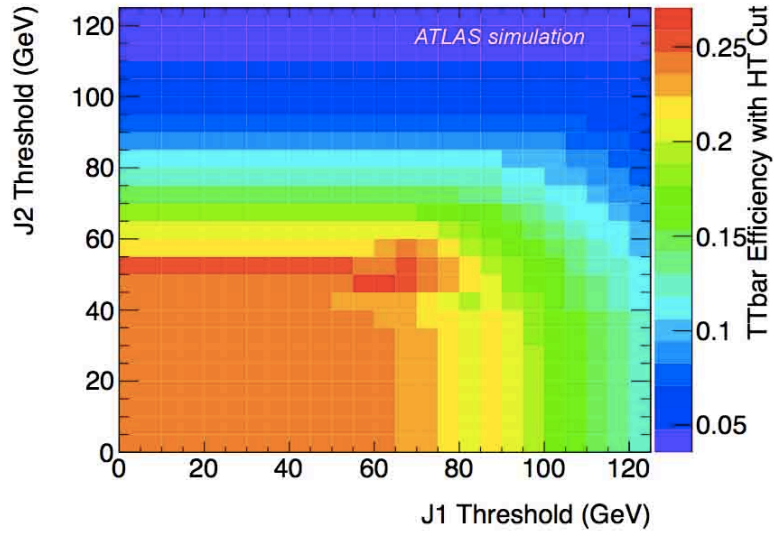
Figure 9.4. Efficiency of the Level-1 $t\bar{t}$ trigger as a function of the two leading jet E_T thresholds. The efficiencies shown refer to a 5 kHz output rate when $H_T > 180$ GeV is requested. .

topological trigger, the best efficiency achieved at a 5 kHz trigger rate was 19.7% for a jet-1, jet-2 (J1, J2) threshold of (85, 60), or (75, 65) GeV. However, as shown in Fig. 9.4, an efficiency of 27.1% was achieved by triggering instead on (J1, J2) > (55, 45) GeV combined with an H_T cut of 180 GeV, where H_T is the scalar sum of jets with threshold > 20 GeV.

With the H_T cut, one records 1.37 times as many events for the same Level-1 trigger rate. Compared with a (J1, J2) cut at (55,45), the H_T cut achieves a rate reduction of a factor of 3.7, at a cost of reducing the efficiency by only a factor of 1.24. The H_T cut improves therefore the s/b by a factor of 3 and this is much better than prescaling in order to control the rate. The jet thresholds are reduced by ≈ 20 GeV, which for some physics purposes may be even more important than the improvement in efficiency or s/b. As an example of the flexibility introduced, other good operating points are opened up by having H_T as a possible cut: requiring $H_T > 210$ GeV but no other cuts gives an efficiency of 24.6% at 5 kHz, which represents an intermediate value in efficiency between the J1, J2, and the J1, J2, H_T cuts discussed above.

A number of other processes was studied. One is VBF H(120) decaying to tau tau, where the combination of cuts on jets, missing E_T and H_T looks promising. For this process forward jets tagging is presently under investigation, suppressing backgrounds by requiring large $\Delta\eta$ between the forward tag jets and other central jets. SUSY (with cuts on contra-transverse mass and H_T) and $H \rightarrow WW \rightarrow ee\nu\nu$ (with cuts on $\Delta\phi$ between the leptons) are also considered. None of these studies would even be feasible without the more detailed RoI information which this hardware upgrade provides.

10. Compatibility with Phase-II Upgrade

In this section, the ATLAS planning for the Phase-II upgrade is briefly outlined to demonstrate that the changes proposed at Phase-I are fully compatible with the further upgrades needed for operation at an instantaneous luminosity of $5\text{-}7\times10^{34}$cm^{-2} s^{-1} and integrated luminosity up to 3000 fb^{-1}.

10.1 Level-1 muon trigger upgrade scenario

The small wheel upgrade in Phase-I is designed to achieve a rate reduction at Level-1 for the muon triggers, at a given threshold, by a factor 6-7. This is mainly achieved by removing the fake triggers in the end-cap, since these dominates the Level-1 muon rate. At Phase-II, the rate can be further reduced by improving the p_T resolution of the muon trigger system in both barrel and end-cap. The new small wheels are designed to already provide the required resolution for this possibility.

A substantial improvement in the p_T resolution can be achieved if additional information on position or angular resolution are available for generating the muon Level-1 trigger. Such an upgrade will become feasible given a longer Level-1 latency anticipated for the Phase-II upgrade of ATLAS. Various ideas are currently under consideration; basically this can be realized by importing the Level-2 algorithms to Level-1.

In the barrel region, all the three muon stations are inside the toroidal magnetic field. By using the three stations to determine the track sagitta, over the lever arm of about 5 m, the p_T resolution can be significantly improved for the muons with p_T around the trigger thresholds. In this way the p_T determination is not affected by the size of the luminous region nor multiple scattering in the calorimeter. A simulation study has shown that a p_T resolution comparable to that of Level-2 trigger could be achieved if a modest position resolution of 1-2 mm is available, leading to a reduction of rate of more than a factor 6 [49]. However, the present granularity of the barrel trigger chambers does not allow such a position resolution. Furthermore only 2 stations, middle and outer, are equipped with the trigger chambers. Therefore a possibility would be to use the MDT chambers for the Level-1 trigger.

In the end-cap, since the end-cap toroid is a closed object, no detector can be installed in the region with the magnetic field. The analysis of p_T should be based on precision track angles before and after the magnetic field. With the new small wheel the precision before the magnet will be improved to better than 1 mrad. Remaining improvements require achieving a precision angle after the magnet on the EM station. In the inner part of the EM station, it is conceivable to replace the relatively small number of trigger chambers with new chambers of higher granularity. Given a lever arm of nearly 2 m, a position resolution of 1 mm on the new trigger chambers will be sufficient to achieve an angular resolution of 1 mrad, thus improving the p_T resolution by a factor 3. At larger radius, the same technique as proposed for the barrel can be adopted using the MDT chambers to achieve an improved angular resolution in the EM station. Access to the front-end electronics is possible for all the EM MDT chambers. If a p_T resolution similar to that of Level-2 is achieved by such an upgrade, a rate reduction by about factor 2.5 is expected in the end-cap [49].

With these upgrades, an overall reduction of Level-1 muon rate with respect to the Phase-I of more than a factor 2 would be achievable. Accurate assessment of achievable goals is further required.

10.2 LAr FCal and HEC electronics upgrade scenario

The ATLAS calorimeters are designed to cope with a peak luminosity of 10^{34} cm^{-2}s^{-1} and an integrated luminosity of 700 fb^{-1} [4]. The instantaneous and integrated luminosity expected during the operations in Phase-II create two separate classes of problems for the ATLAS calorimeter systems: issues related to rates and average energy deposited by particles from minimum bias events, dependent on the instantaneous luminosity, which impact the functionality of the forward calorimeter (FCal [67]), and issues related to long-term radiation damage of the on-detector electronics. The latter affects the cold pre-amplifier and summing electronics of the Hadronic End-cap Calorimeter (HEC [68]), and the front-end readout of the LAr barrel and end-cap calorimeters. Further motivations for changes related to the calorimeter system are improvements of the ATLAS trigger system in Phase-II and natural ageing effects of electronic components.

The known limitations of the LAr FCal at luminosities beyond the LHC design value of 10^{34} cm^{-2}s^{-1} are ion build-up in and HV drop across the LAr gaps of the FCal, as well as possible boiling of argon. Due to space-charge effects above the critical ionization rate, the calorimeter signal is no longer proportional to the deposited energy [69]. Ion build-up effects are measured in reduced-size FCal modules with a dedicated experimental setup using a ^{90}Sr source at the University of Arizona [70] and at the Hilum testbeam experiment at IHEP in Protvino, Russia [71]. The results of FCal pulse shape analyses and HV currents drawn at the highest particle fluxes are in agreement with a modeling of ion build-up in the LAr gap [72]. Uncertainties on the predictions are currently being determined. The predicted FCal signals at different instantaneous luminosities are shown in Figure 10.1, left panel, for the region at the largest pseudo-rapidity of $|\eta| \approx 4.7$. The resulting degradation of the FCal at different instantaneaous luminosities is illustrated in Fig. 10.1, right panel. Three performance regions are defined in each FCal module: a degraded $|\eta|$ region with signal amplitudes reduced by 20% or more, indicated in red in Fig. 10.1; a marginally degraded $|\eta|$ region with HV drop of more than -30 V, indicated in yellow, and a region with normal performance, indicated in green. The degraded region is therefore at $4.5 < |\eta| < 4.9$ in FCal-1 and at $4.8 < |\eta| < 4.9$ in FCal-2 at luminosities of 3×10^{34} cm^{-2}s^{-1}.

Furthermore, dE/dx and Ohmic heating of the FCal may cause the liquid argon to boil. Simulations put the FCal right at the edge of proper functioning for instantaneous luminosities of 5×10^{34} cm^{-2}s^{-1} and beyond. Additional cryostat cooling loops near the FCal can avoid overheating.

Therefore, a possible option is to design a new FCal detector (sFCAL) with a reduced gap size, with a modified HV distribution circuit, and with the addition of cooling loops. An alternative upgrade option to deal with the limitations of the FCal, is to install a small warm calorimeter inside the inner warm tube of the calorimeter just in front of the FCal. This detector, called Mini-FCal [73] shown in Fig. 10.2, is composed of copper absorber plates interleaved with diamond detector sensor planes. Alternatively, high pressure Xenon or liquid Argon are studied for use as active medium. A MiniFCal will, however, introduce a region with reduced response due to inactive material at η ranges close to its outer boundary, where support and readout structures need to be placed. Furthermore, the proposed technology with diamond sensors shows strong dependence of the signal yield on the irradiation [74].

On the other hand, the replacement of the FCal with a new sFCal requires an opening of the
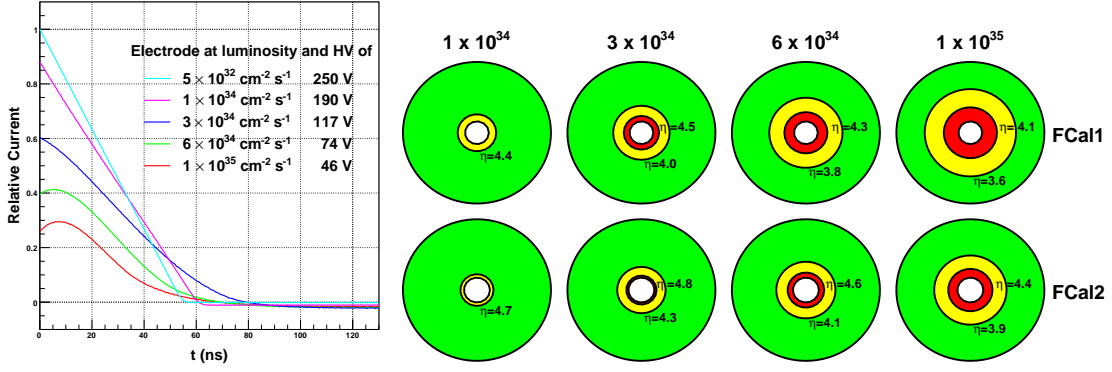
Figure 10.1. Left: Simulated signal pulses at $|\eta| = 4.7$ for different luminosities. For each luminosity the same signal energy is deposited in the FCal1 module on top of the minimum-bias background and the signal current pulse is extracted. For luminosities below $10^{33} \text{cm}^{-2}\text{s}^{-1}$ the signal on the electrodes is the familiar triangular pulse. Even at $10^{34} \text{cm}^{-2}\text{s}^{-1}$ the signal is nearly trianguar but degraded a bit due to the sagging potential from the excessive current drawn through the protection resistor and due to the build-up of positive ions in the liquid argon gap. At higher luminosities both the magnitude and shape of the pulse are degraded. At $|\eta| = 4.0$ the current pulses are the same as shown here but at luminosities a factor 8 higher. Right: Degradation maps superimposed on the face of the FCal1 and FCal2 modules for various luminosities. Green indicates acceptable performance, yellow indicates marginal performance, and red denotes unstable, degraded operation. At $10^{35} \text{ cm}^{-2}\text{s}^{-1}$ about 20% of the coverage in the forward region of the FCal1 module is lost.
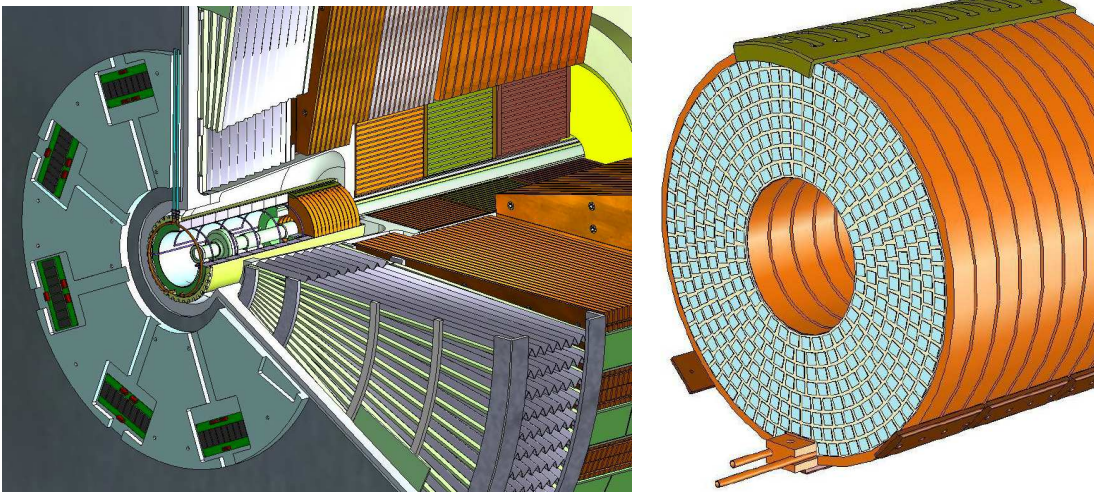
Figure 10.2. Baseline layout of Mini-FCal. The left hand illustration is an overview of the Mini-FCal showing the surrounding detectors and cryostat with part of the beam pipe still in place. Five of the preamplifier boards can be seen on the front face of the LAr cryostat. The right hand diagram shows the Mini-FCal in detail with the first absorber removed so that the diamond detector layer can be seen. The cooling pipes are visible at the bottom.

end-cap cryostats, which also house the electromagnetic and hadronic end-cap calorimeters. The estimated risk of compromising calorimetric measurements in the end-cap region is considered significant. For these reasons, the FCal detectors remain unchanged during LHC Phase-I and a

replacement of the FCal or installation of a MiniFCal are only considered for Phase-II.

As for the Hadronic End-cap Calorimeter (HEC) [4] Monte Carlo simulations estimate a neutron fluence of 0.2×10^{14} n/cm^2, a dose of 330 Gy and a hadronic fluence of 3.1×10^{11} h/cm^2 after an integrated luminosity of 1000 fb^{-1} at the location of HEC cold electronics. Their design specifications on radiation tolerance include a safety factor of 10 to take into account the simulation uncertainties as also confirmed by a complete radiation characterization of both pre-production and production batches [75, 76]. Thus, only a reduced safety margin remains until the end of LHC Phase-II, i.e. the present HEC cold electronics may be at its limit of reliable operation. A new ASIC is currently being developed [77, 78] that will be ten times more radiation hard. It would be available to replace the present GaAs chips in LHC Phase-II.

Since a replacement of the HEC cold electronics also requires an opening of the end-cap cryostat, which is a major high-risk intervention, it is essential to accumulate more experience on the level of agreement or disagreement between calculated and measured radiation doses in this region. If the expected dose in this region is close to current projections, and the safety factor of 10 can be reduced by at least a factor 3, the problem even for Phase-II could be removed. The following 3 scenarios therefore have to be considered:

1. If the HEC cold electronics does perform as required and if the current FCal fulfils the performance requirements imposed by Phase-II physics goals, no replacement of the HEC electronics or of the FCal will be necessary.
2. If the HEC cold electronics must be replaced, the large cold cryostat cover will be opened, the HEC pre-amplifier and summing electronics will be replaced. The irradiated FCal will be removed and a newly built cold sFCal will be inserted before closing the cryostat.
3. If the HEC cold electronics does not need to be replaced, but if the FCal shows intolerable performance losses, either the FCal will be replaced by a new one of the sFCal type, or a MiniFCal will be placed in front of the existing cold FCal. In case of a FCal replacement it is anticipated that only the small cover (the FCal bulkhead) of the cold vessel has to be removed. Should a MiniFCal be installed, only the cryostat warm vessel needs to be opened.

In case the performance degradations of the FCal turn out to be more significant than estimated at the time of this Letter of Intent, the installation of a warm MiniFCal would need to be brought forward as a further Phase-I upgrade.

10.3 Calorimeter read-out electronics upgrade scenario

For the LHC Phase-II, LAr Front-End Boards (FEB [79]), installed on the detector in an area of high radiation dose, are planned to be upgraded. The reason is that the total dose for an integrated luminosity of 3000 fb^{-1} exceeds the FEB specifications [80], the Level-1 trigger latency may exceed the depth of the analog pipeline memories installed on the FEB [81], and the natural ageing of electronic components of the FEBs.

The next generation FEB is being planned to be designed either with a fully digital free-running readout, i.e. avoiding trigger signal receivers and data buffering on the FEB, or with a large digital data buffer on the front-end to cope with increased latency requirements. The sTBB system foreseen in Phase-I (see Chapter 2) will be able to receive trigger data also from the new

FEB boards in Phase-II. Such a solution allows sending LAr trigger primitives respecting both the Phase-I and future Phase-II latency requirements, where the latter are to be optimized with respect to the overall ATLAS trigger system.

Similarly, the readout of the Tile calorimeter will be upgraded with new front-end electronics in new drawers which are also providing data in free running mode with highest possible granularity.

10.4 Inner detector and R&D technologies

The present inner detector for ATLAS has a limited lifetime. The functionality of the silicon-based parts of the ATLAS detector have a limit based on total radiation dose (fluence), the gas based TRT outer tracker has a limit based on instantaneous luminosity because of very high occupancy. The TRT is not designed to run at $5 \times 10^{34} \text{cm}^{-2}\text{s}^{-1}$ instantaneous luminosity, leading to the proposal to construct an all silicon replacement for the current tracker. The most fundamental limits are those associated with the silicon sensors. The critical factors for the sensors include reduction in depletion depth at a given voltage (resulting in loss of signal), increased leakage current (potentially leading to thermal runaway from detector self-heating) and ultimately charge trapping (also resulting in loss of signal). Radiation damage also affects the operation of the read-out electronics and will decrease the operating voltage margin, the difference between the required voltage and the maximum voltage allowed for the integrated-circuit electronics in each pixel module. Some parts of the optical data transmission system (lasers that transmit light from the pixel detector and diodes that receive light from outside the detector) will also suffer from radiation damage.

The design limit for the currently installed pixel system is estimated to be 50 MRad and 10^{15} (1 MeV neutron equivalent per cm^2), values not expected to be reached before the end of Phase-I running. The new Insertible B-layer (IBL) is designed to be able to withstand the much higher doses closer to the beam, and to be fully operational also through to the shutdown for Phase-II.

The pixel detectors are significantly more radiation hard than the current ATLAS strip detectors due to two factors. The first has to do with the pixels exploiting n-on-n (n-implant read-out) technology, resulting in charge collection on the (high field) junction-side of the detector after irradiation (which reduces sensitivity to partial depletion and trapping). The second factor is the very low electronics noise that results from the low input capacitance (due to the smallness of the individual sensor elements).

n-on-n based detectors have subsequently been proven with the new FE-I4 pixel chip, developed for the IBL, to doses well beyond $5 \times 10^{15} \text{n}_{eq} \text{ cm}^{-2}$ (1 MeV equivalent). They are to be employed for that detector, ideally complemented by 3D based sensors providing coverage at high η, and both they, and the 3D sensors, have shown excellent performance in test-beam after such high doses.

The n-on-n detectors, although more robust, were considered too expensive for the strip region, which has a much larger area than the pixel region. The current strip detector lifetime is limited to about $2 \times 10^{14} \text{n}_{eq} \text{ cm}^{-2}$ (1 MeV equivalent). This represents an upper limit to the integrated luminosity that can be survived of 700 fb^{-1}. However, with improved electronics, shorter strips and n-implants using p-type technology, it can be shown that a replacement silicon strip tracker at the same radii can be constructed to withstand 3000 fb^{-1} (large area sensors and prototype modules having been shown to survive the corresponding doses, including a factor of 2 safety margin).

The overall new tracker layout is currently foreseen to have at least four pixel layers followed by 5 back-to-back small angle stereo strip layers. The intention is to design the detector with a longer barrel than current ATLAS to move the services further out in eta. The final layout is still under discussion with the barrel length and number of discs being optimised. Because it is possible in some designs to respect the current radial boundary between the pixel and strip systems (the Pixel Support Tube), it is possible to consider staging the pixel upgrade at a different time from the tracker replacement. Furthermore, the IBL is, by design, independently accessible. These possibilities are being actively studied in the context of the Phase-II upgrade planning, but could be compatible with the Phase-I timescale if required.

10.5 Pixel detector strategy

Recognizing that the present pixel detector pushed the limits of available technology at the time, soon after installation the ATLAS collaboration began developing new technologies for future pixel detectors. Developments that are already advanced today include a new readout integrated circuit called FE-I4, new sensor developments, mechanical structures based on a new type of high thermal conductivity carbon foam, electro-mechanical integrated structures, and power distribution. The technology developments follow a road-map inspired by the requirements of a future high luminosity LHC upgrade, but have the generic goals of reducing mass and cost while increasing rate capacity and radiation tolerance. The Insertable B-Layer (IBL) upgrade represents the first deployment of some of these new technologies.

The installation of the insertable B-layer (IBL) in the 2013-2014 shut-down provides an early improvement of the ATLAS b-tagging capability by taking advantage of a smaller beam pipe, reduced material and a smaller pixel granularity. As part of the upgrade of the complete inner detector foreseen for Phase-II, the pixel detector will also be replaced. However, earlier upgrading might become necessary, if a strong increase in the physics performance can be realized or the detector performance degrades such that significant inefficiencies can be expected before the start of Phase-II. Since the pixel detector can be extracted separately from the other part of the inner tracker, an upgrade already in Phase-I can be envisaged. To be prepared for such a scenario, the performance of the current pixel detector should be closely monitored and, in parallel, studies to build an optimal detector should be performed.

Inefficiencies of the current pixel detector may come from several causes. They may result from losses of modules during operation, e.g. thermal cycling, damage caused by the 10^{15} n_{eq}/cm^2 of radiation expected by 2021, increased occupancy in the module and too high bandwidth required of the read-out. Extrapolating the observations of the first 18 months of data taking leads to the current expectation that the performance of the pixel detector is only modestly degraded. Furthermore, in the framework of the IBL installation in 2013-2014, a possible intervention is planned for fixing the existing problems and mitigating further potential readout problems at the ultimate luminosity (the new Service Quarter Panels, nSQP, project). Such repairs will require the extraction of the entire pixel detector to the surface for installation of the new service quarter panels along with the IBL detector itself. During 2012 the Collaboration will decide whether this critical operation should go ahead or not. If the decision is negative, then some extrapolations of the current pixel performance with dose and ageing approach thresholds where different options, such as substituting the entire pixel detector, might have to be considered.

In parallel, first simulation studies have been performed to evaluate the physics gain of using IBL technologies to replace the three current pixel layers and the forward region. They indicate for *b* tagging an increased rejection of the light flavor background which is about 25-50%. Furthermore, such an early replacement should accommodate the boundaries of the foreseen Phase-II upgrades which are still uncertain.

Therefore a possible Phase-I upgrade should be revisited in 2013. Such a reassessment should account for developments both in the performance of the current pixel detector and further technology and lay-out improvements, To prepare this decision, the current detector should be closely watched, an R&D program be developed and simulations performed to arrive at an optimal lay-out, also taking into account the emerging constraints of the Phase-II upgrade.

- With the rapidly increasing luminosity and occupancy, in 2013 a better picture of potential deficiencies in the losses of modules, radiation damages and the read-out will be obtained. The quantitative gains due to the eventual repair can be better estimated in 2013.

- Substantial physics gain may be realized by evolving technologies allowing e.g. for further reduction of material and better resolutions. The plan is therefore to launch an R&D program such that a reasonable assessment of new technologies for a Phase-I upgrade can be made in 2013. This program includes sensor technologies, front-end chips, interconnects, powering schemes and reduced stave materials. Its principle aims are a smaller pitch and reduced materials. This R&D effort is seen also as part of arriving at the best Phase-II pixel detector technology

- Simulation studies on relevant physics processes should be performed. This aims at finding an optimal lay-out including granularity, new stave concepts etc. First ideas can be seen in Fig. 10.3

Although currently there is no decision on the upgrade of the pixel detector foreseen for Phase-I, physics may call for such an option. Provisions should be made in the next years to eventually arrive at a well founded assessment and an optimal detector lay-out.

10.6 Phase-II TDAQ and Level-1 track trigger upgrade compatibility

It is expected that all calorimeters will convert to on-detector digitisation for Phase-II operation. Hadronic data, probably with finer granularity than current trigger towers, would be provided in real time for the trigger either from the new calorimeter RODs, or by an extension of the Digital Processing System (DPS). Additional EM information would also become available in calorimeter RODs. The hadronic information, and additional EM information if needed, would enter the Feature Extractor (FEX) using inputs prepared in Phase-I but mostly unused at that stage. The FEX would thus have data from all ATLAS calorimetry, and would be able to identify all current calorimeter-based trigger signatures with improved performance. The previous analogue-based L1Calo, by now of order 15 years old, could be retired.

The muon trigger would be provided by existing and possibly additional detectors via the sector logic and Phase-I MuCTPI. This might require firmware changes but would otherwise use optical capability prepared for L1Muon in advance in the new Phase-I design. The trigger decision
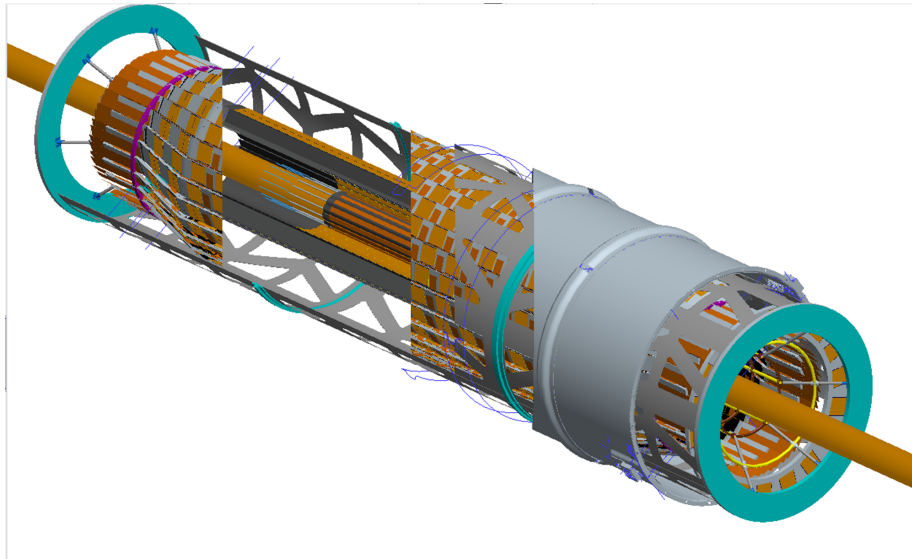
Figure 10.3. 3-D model view of part of a preliminary layout for a phase-II pixel detector, shown staged inside the existing pixel detector support tube (solid outer shell).

would be formed by processing calorimeter and muon data in a topological processor, possibly adapted from the proposed Phase-I L1Topo with more closely integrated CTP functions (trigger rate management, bunch structure awareness, etc). Although demanding to realize, it is desirable that the trigger signal in this scheme be provided with roughly the same latency as today's Level-1 Accept (i.e. $\sim 3\mu$s).

Tracking is a key ingredient in the current Level-2 trigger. Given the great challenges for the Level-1 trigger in Phase-II, it is likely that tracking information will have to be used in the hardware trigger to achieve the full physics potential of ATLAS. Work is underway to quantify the benefits of a Level-1 track trigger (L1Track) and to evaluate alternative designs. The main design challenge is to reduce the bandwidth of data coming out of the tracker, as it is unrealistic to read out the whole tracker for every bunch crossing. The architecture that is currently preferred is an RoI-seeded L1Track, fitting into a two step hardware trigger.

In the RoI-seeded concept, the RoIs are projected into the tracker, and only the regions they select are used in the search for tracks. This approach has several advantages: it does not require any modifications to the tracker layout, which can therefore be optimized for offline performance; it provides a uniform coverage in pseudorapidity; and it may require an equivalent overall readout rate in the tracker of less than 100kHz. Work is advanced to include the two-step functionality in the next iteration of the front-end readout chip for the strip layers of the new tracker. However, alternative designs for L1Track are also under consideration. A decision on the need and benefits of a track trigger and on the optimal design is expected during 2012.

To provide the two-stage hardware trigger, the Phase-II trigger described above would be re-labelled as the Level-0 trigger, and would provide RoI seeds with a rate of up to 500kHz to initiate data capture in L1Track and possibly in L1Muon. The second stage of the Phase-II hardware trigger, i.e. the Level-1 Trigger, would start processing following a Level-0 Accept (L0A) decision. The additional time allowed implies that this stage of trigger could have available not only the

Inner Detector tracks (from L1Track), but also more refined fine-grain calorimeter data (obtained by additional calorimeter ROD interrogation following the L0A), and improved muon track information (from the high-precision but slower MDTs). Processing for the Level-1 trigger decision would culminate in global trigger decision logic incorporating both topological and combinatorial functions. New electronics would be required for the Level-1 trigger, as nothing comparable is planned earlier. An overall latency of $\sim 10\mu$s is under discussion for this trigger.

Detector front ends and readout would need some revising to accommodate the two-stage hardware trigger, and could then also take advantage of new precision timing distribution. Accommodating the two-stage concept implies a more complicated readout architecture, but this is principally an issue for the detectors not directly involved in the Phase-I upgrade, notably the barrel muon detector.

11. Phase-I Resources

The collaboration decision and strategy is to express the costs associated to the activities described in this LOI in terms of CORE values.

The CORE values basic idea is to focus on direct production costs (external costs) and exclude basic infrastructure and personnel costs. CORE thus includes things like components (but not necessarily spares, except in TDAQ), production (incl. industrial manpower but not institute manpower), outsourced parts of assembly, outsourced parts of installation, commissioning. CORE does NOT include items such as infrastructure (i.e. production area, halls, tech support etc.) R&D, design, (early stage) prototyping, institute manpower, physicists, taxes, contingency.

The strategy is to rely on the concept of deliverables. Institutes and their Funding Agencies commit to provide given in-kind items, assemblies and detector parts as deliverable objects, after having agreed on the CORE value. What are defined as deliverables reflect the core competences of the institutes providing them and will not be subject to central accounting and book-keeping.

Item	Core cost (MCHF)	Possible additions	2012	2013	2014	2015	2016	2017	2018
New muon small wheels	9.20	0.14	0.00	0.63	1.75	2.54	2.95	1.28	0.04
New LAr calorimeter electronics	7.98	0.00	0.19	0.78	0.13	0.94	4.06	1.88	0.00
New Tile calorimeter upgrade	0.38	0.00	0.00	0.03	0.03	0.14	0.14	0.03	0.00
Fast TracKer	3.59	0.00	0.51	0.96	0.63	0.8	0.34	0.26	0.00
Trigger and DAQ upgrade	8,78	3.21	0.33	1.36	0.62	0.44	0.98	1.35	3.70
Forward physics	2.70	0.00	0.33	1.04	0.88	0.10	0.35	0.00	0.00
Total (MCHF)	32.62	3.35	1.37	4.80	4.03	5.05	8.83	4.81	3.73

Table 11.1. CORE Cost table

Table 11.1 shows the cost of the 6 projects defined in this LOI. In the second column, each project CORE cost is expressed in MCHF units. In the third column some possible additional costs are anticipated. These are the costs of items which may still need to be part of the overall procurement. The final decision on these can only be taken at a later stage, when the corresponding projects are better understood and defined. In the left column the payment profile is presented. It peaks during the year 2016, when all major components will be procured. The total figures amount to 36 MCHF to be spent between 2012 and 2018. About 9M out of the 36M is of a common nature and will be handled centrally through a special common fund. A more detailed cost table, with a break down item by item can be found through the following WWW-address: https://edms.cern.ch/document/1164764.

For each of the 6 projects it is foreseen that a MOU document will be produced which will describe the duties of each institute involved in the construction, with a proper corresponding acknowledgement of the associated CORE value. Each MOU will then be signed by each Funding Agency involved and will define the time profile for each delivery. Before submission of the MOUs, ATLAS management will organize a proper scrutiny of the costs and of the related project milestones. Where needed by the relevant Funding Agencies to allow commitment of early resources, an interim MoU can also be established, to be superseded by the full MoU once that is adopted.

12. Conclusions

The Letter of Intent presents the strategies for ATLAS running in Phase-I (after the upgrades foreseen in the period 2017-2018), where the LHC is expected to run at a center of mass energy of 14 TeV with a luminosity that could reach 3×10^{34} cm^{-2} s^{-1}, while retaining or enhancing the ATLAS sensitivity to perform accurate measurements and discover new physics.

Full efficiency at the higher luminosities is achieved for muons by introducing a new trigger and tracking device (new small wheel) in the inner forward part of the muon spectrometer, where the trigger rate is dominated by low momentum backgrounds.

New trigger boards, better exploiting the existing granularity of the e.m. calorimeters, will allow a better discrimination between electrons and narrow jets as well as improving the resolution for missing transverse energy at Level-1 trigger. All this will keep the present large (η<2.4) acceptance for single leptons triggers with p_T>20 GeV with high efficiency at the highest luminosities.

The single isolated lepton trigger will allow ATLAS to perform measurements of the relative couplings of the Higgs boson, for example, via the WH final state, using an unbiased W trigger, independent of possible systematic errors due to the assumed production mechanism. It should be noted that the Level-1 threshold usually imposes the need for a higher offline cut, to avoid additional uncertainties due to the details of the threshold turn-on curve. Furthermore, simply raising the p_T threshold to reduce rates will be less effective for the present muon forward region without a detector upgrade due to resolution limitations. Because of both these factors, such trigger improvements can also contribute to the measurement of vector boson scattering at high luminosity, where new phenomena are expected to be found, either in the case that a light Higgs protects the cross-section against unitarity violation, or several Higgs particles exist, or in Higgs-less or non SM-Higgs scenarios. Achieving low value of the p_T lepton trigger thresholds as described in this proposal is particularly crucial for SUSY searches with a compressed mass spectra and for other searches for new physics. In such searches, low thresholds are needed to avoid reduced acceptance and poor efficiencies.

The proposed upgrade to the forward detectors will permit ATLAS to place the best possible limits on a Quartic Gauge coupling of $\gamma\gamma WW$, while offering the capabilities to extend the understanding of the structure of the Pomeron. The proposed Level-1 topological trigger will provide a good level of flexibility to deal with non-standard event topologies and to reinforce the isolation requirements for muon triggers. Finally, the fast accurate tracking at the second level trigger that will be implemented using the FTK will permit events containing b jets and τ leptons to be tagged accurately, while strongly reducing the background due to jet mis-tagging. This will be a very important factor for studying Higgs boson decays, in particular if it decays predominantly into 3rd generation fermions.

The ATLAS inner detector should be able to cope with the occupancy and data rate requirements of Phase-I operation, but a full upgrade of the inner detector, and eventually other components, will be needed for the further luminosity increases expected after 2022. The proposed upgrades in this LoI are, however, designed to be fully compatible with the needs of the Phase-II upgrade. The present LoI therefore constitutes a coherent set of upgrades that will allow ATLAS to fully exploit the LHC physics for the first 300-400 fb^{-1} of integrated luminosity at the highest LHC collision energy.

References

[1] G. Aielli et al., *Comparisons of cavern background simulation and data in the ATLAS muon spectrometer for proton-proton collisions at $\sqrt{s} = 7$ TeV*, ATLAS Note in preparation (2011).

[2] J. Bougher et al., *A FLUGG based cavern background simulation application*, ATLAS Note in preparation (2011).

[3] Deile, M. and Dubbert, J. and Horvat, S. and Kortner, O. and Kroha, H. and others, *Resolution and efficiency of the ATLAS muon drift-tube chambers at high background rates*, Nucl.Instrum.Meth. **A535** (2004) 212–215.

[4] The ATLAS Collaboration, G. Aad et al., *The ATLAS Experiment at the CERN Large Hadron Collider*, JINST **3** (2008) S08003.

[5] The ATLAS Collaboration, *Performance of the ATLAS transverse energy triggers with initial LHC runs at $\sqrt{s} = 7$ TeV*, ATLAS Conference Note, ATLAS-CONF-2011-072 (2011).

[6] D. Casadei, et al., *The implementation of the ATLAS missing E_T triggers for the initial LHC operation*, ATLAS Note, ATL-DAQ-PUB-2011-01 (2011).

[7] ATLAS Collaboration, *ATLAS Tracking Performance in the Presence of Pile-up*, ATLAS-INDET-2010-001.

[8] ATLAS Collaboration, *Performance of the ATLAS Silicon Pattern Recognition Algorithm in Data and Simulation at sqrt(s) = 7 TeV*, ATLAS-CONF-2010-072.

[9] ATLAS Collaboration, *Tracking Results and Comparison to Monte Carlo simulation at sqrt(S) = 900 GeV*, ATLAS-CONF-2010-011.

[10] ATLAS Collaboration, *Tracking Studies for b-tagging with 7 TeV Collision Data with the ATLAS Detector*, ATLAS-CONF-2010-070.

[11] ATLAS Collaboration, *ATLAS TDR 19, IBL Technical Design Report*, CERN/LHCC 2010-013.

[12] ATLAS Collaboration, *Track Reconstruction in Pb-Pb collisions at sqrt(SNN) = 2.76 TeV*, ATL-COM-PHYS-2011-015.

[13] Alexey Antonov, Anatoli Romaniouk, Evgeny Shulga and Sergej Timoshenko, *TRT tracking study and optimization for Heavy Ions*.

[14] *ATLAS muon spectrometer: Technical design report, CERN-LHCC-97-22, ATLAS TDR-10*, (1997).

[15] *The ATLAS shielding project*, http://atlas.web.cern.ch/Atlas/GROUPS/Shielding/shielding.htm.

[16] Bittner, B.and Dubbert, J.and Kortner, O.and Kroha, H. and Legger, F. and others, *Development of muon drift-tube detectors for high-luminosity upgrades of the Large Hadron Collider*, Nucl.Instrum.Meth. **A617** (2010) 169–172.

[17] Giomataris, Y. and Rebourgeard, P. and Robert, J.P. and Charpak, Georges, *MICROMEGAS: A High granularity position sensitive gaseous detector for high particle flux environments*, Nucl.Instrum.Meth. **A376** (1996) 29–35.

[18] Giomataris, I. and De Oliveira, R. and Andriamonje, S. and Aune, S. and Charpak, G. and others, *Micromegas in a bulk*, Nucl.Instrum.Meth. **A560** (2006) 405–408.

[19] Alexopoulos, T. and Burnens, J. and de Oliveira, R. and Glonti, G. and Pizzirusso, O. and others, *A spark-resistant bulk-micromegas chamber for high-rate applications*, Nucl.Instrum.Meth. **A640** (2011) 110–118.

[20] De Geronimo, G. and Fried, J. and O'Connor, P. and Radeka, V. and Smith, G.C. and others, *Front-end ASIC for a GEM based time projection chamber*, IEEE Trans.Nucl.Sci. **51** (2004) 1312–1317.

[21] ATLAS Collaboration, *Liquid Argon Calorimeter Technical Design Report*, CERN/LHCC/96-041 (1996).

[22] N.J. Buchanan et al., *ATLAS liquid argon calorimeter front end electronics*, JINST **3** (2008) P02010.

[23] A. Bazan et al., *ATLAS liquid argon calorimeter back end electronics*, JINST **2** (2007) P06002.

[24] N.J. Buchanan et al., *Design and implementation of the Front End Board for the read-out of the ATLAS liquid argon calorimeters*, JINST **3** (2008) P09003.

[25] J. Collot et al., *The LAr tri-gain shaper*, LARG-NO-92, 1998.

[26] C. Cerna et al., *Cabling of the ATLAS liquid argon calorimeters*, ATL-A-EN-0001, 2003.

[27] T. Andeen, *Update on the ADC developments at NevisTitle not yet available*, https://indico.cern.ch/getFile.py/access?contribId=0&resId=0&materialId=slides&confId=144588.

[28] D. Dzahini, *ADC developments at Grenoble*, https://indico.cern.ch/getFile.py/access?contribId=1&resId=0&materialId=slides&confId=156528.

[29] The Liquid Argon Group (LARG), *Proposals for Upgrade of the ATLAS Liquid Argon Calorimeter Front-End Read-out*, ATU-SYS-ES-0010, EMS Doc. No: 1160765 https://edms.cern.ch/1160765/1, 2011.

[30] E. Chapon, O. Kepka, C. Royon, *Anomalous $WW\gamma$ coupling in photon-induced processes using forward detectors at the LHC*, Phys. Rev. D **78** (2008) 073005.

[31] G.Altarelli and G.Parisi, Nucl. Phys. **B126** 18C (1977) 298. V.N.Gribov and L.N.Lipatov, Sov. Journ. Nucl. Phys. (1972) 438 and 675. Yu.L.Dokshitzer, Sov. Phys. JETP. **46** (1977) 641.

[32] V.A. Khoze, A.D. Martin, M.G. Ryskin, Eur. Phys. J. **C19** (2001) 477; Eur. Phys. J. C**23** (2002) 311; Eur. Phys. J. C**24** (2002) 581; M. Boonekamp, R. Peschanski, C. Royon, Phys. Rev. Lett. **87** (2001) 251806.

[33] F. Roncarolo, R. Appleby, K. Potter, P.Bussey and C. Bracco, CERN-sLHC-Project-Note-0029.

[34] R. Appleby et al., *The proceedings of EPAC08*, Genoa, Italy, June 23-27 2008.

[35] P.J. Bussey and W. Plano, *FPTrack*, in preparation.

[36] J. Monk and A. Pilkington, *ExHuME: A Monte Carlo event generator for exclusive diffraction*, Comput. Phys. Commun. **175** (2006) 232 [arXiv:hep-ph/0502077]; M. Boonekamp, A. Dechambre, V. Juranek, O. Kepka, M. Rangel, C. Royon, R. Staszewski, [arXiv:1102.2531].

[37] K. Piotrzkowski, U. Schneekloth, *Proc. of the ZEUS Collaboration meeting*, March 1994, DESY, Hamburg.

[38] IBL Coll, CERN-LHCC-2010-013, ATLAS-TDR-019 5/09/2010.

[39] ATLAS Collab., JINST **3** (2008) P07007.

[40] CMS Collab., NIM **A 552** (2005) 232.

[41] A. Brandt, *Microchannel Plate PMT Lifetime and Performance*, DIRC2011: Workshop on Fast Cerenkov detectors, Giessen, Germany, April 4-6, 2011.

[42] B. Ashmanskas et al. (CDF Collaboration), *The CDF silicon vertex trigger*, Nucl.Instrum.Meth. A518, 532 (2004).

[43] J. Adelmanet al. (CDF Collaboration), *The Silicon Vertex Trigger upgrade at CDF*, Nucl.Instrum.Meth. A572, 361 (2007).

[44] P. Bussey, *FPTrack Programme*, http://ppewww.physics.gla.ac.uk/ bussey/FPTRACK/.

[45] CERN-TH/2002-078, http://arxiv.org/pdf/hep-ph/0204087v1.

[46] CERN-OPEN-2008-020, http://arxiv.org/pdf/0901.0512.

[47] ATL-CONF-2011-103, http://cdsweb.cern.ch/record/1369826.

[48] Dobado, A. and Herrero, M. J. and Pelaez, J. R. and Ruiz Morales, E., *LHC sensitivity to the resonance spectrum of a minimal strongly interacting electroweak symmetry breaking sector*, Phys. Rev. **D62** (2000) 055011.

[49] Aad, G. and others, *Expected Performance of the ATLAS Experiment - Detector, Trigger and Physics*, (2009).

[50] Schumacher, J., *Sensitivity of ATLAS to Alternative Mechanisms of Electroweak Symmetry Breaking in Vector Boson Scattering $qq \rightarrow q\bar{q}\ell\nu\ell\nu$*, Ph.D. thesis, TU Dresden, 2010.

[51] R. Gupta, *Probing quartic neutral gauge boson couplings using diffractive photon fusion at the LHC*, http://arxiv.org/pdf/1111.3354.

[52] P. J. Bell, Eur. Phys. J. **C64** (2009) 25..

[53] E. Chapon, O. Kepka, C. Royon, Phys. Rev. **D81** (2010) 074003; O. Kepka and C. Royon, Phys. Rev. D **78** (2008) 073005..

[54] K. Golec-Biernat, C. Royon, L. Schoeffel, R, Staszewski, arXiv:1110.1825, in press in Phys. Rev. D..

[55] Buchmueller, O. and others, *Supersymmetry in light of $1 fb^{-1}$ of LHC Data*, (2011).

[56] Akula, Sujeet and Feldman, Daniel and Liu, Zuowei and Nath, Pran and Peim, Gregory, *New Constraints on Dark Matter from CMS and ATLAS Data*, Mod. Phys. Lett. **A26** (2011) 1521–1535.

[57] Allanach, Benjamin C. and Barr, Alan J. and Dafinca, Alexandru and Gwenlan, Claire, *Discovery reach for generic supersymmetry at the LHC: M_{T2} versus missing transverse momentum selections for pMSSM searches*, JHEP **07** (2011) 104.

[58] Cassel, S. and Ghilencea, D. M. and Kraml, S. and Lessa, A. and Ross, G. G., *Fine-tuning implications for complementary dark matter and LHC SUSY searches*, JHEP **05** (2011) 120.

[59] Allanach, B. C. and Khoo, T. J. and Lester, C. G. and Williams, S. L., *The impact of the ATLAS zero-lepton, jets and missing momentum search on a CMSSM fit*, JHEP **06** (2011) 035.

[60] Papucci, Michele and Ruderman, Joshua T. and Weiler, Andreas, *Natural SUSY endures*, (2011), arXiv:1110.6926.

[61] Gianotti, F. and others, *Physics potential and experimental challenges of the LHC luminosity upgrade*, Eur. Phys. J. **C39** (2005) 293–333.

[62] Djouadi, A. and Mambrini, Y., *Three body decays of top and bottom squarks*, Phys.Rev. **D63** (2001) 115005.

[63] Bornhauser, S. and Drees, M. and Grab, S. and Kim, J.S., *Light Stop Searches at the LHC in Events with two b-Jets and Missing Energy*, Phys.Rev. **D83** (2011) 035008.

[64] Lytken, E., *Searches for direct slepton production with ATLAS*, Czech. J. Phys. **54** (2004) A169–A173.

[65] Barr, A. J., *Measuring slepton spin at the LHC*, JHEP **02** (2006) 042.

[66] Aad, Georges and others, *Search for supersymmetry in final states with jets, missing transverse momentum and one isolated lepton in $\sqrt{s}$ = 7 TeV pp collisions using 1 fb^{-1} of ATLAS data*, Phys.Rev.D (2011).

[67] A. Artamonov et al., *The ATLAS Forward Calorimeter*, JINST **3** (2008) P02010.

[68] D. M. Gingrich et al., *Construction, Assembly and Testing of the ATLAS Hadronic End-cap Calorimeter*, JINST **2** (2007) P05005.

[69] B. Toggerson, A. Newcomer, J. Rutherfoord, R. B. Walker, *Onset of space charge effects in liquid argon ionization chambers*, Nucl. Inst. Meth. **A608** (2009) 238.

[70] J. Rutherfoord, et al., *Measurement of ion buildup and Ar^{+} mobility in a small-scale ATLAS FCal module*, to be published (2011).

[71] A. Glatte, et al., *Liquid Argon Calorimeter Performance at High Rates*, submitted to Nucl. Inst. Meth. A (2011).

[72] J. Rutherfoord, *Signal degradation due to charge buildup in noble liquid ionization calorimeters*, Nucl. Inst. Meth. **A482** (2002) 156–178.

[73] RD42 Collaboration, *Development of Diamond Tracking Detectors for High Luminosity Experiments at the LHC*, Internal Report CERN/LHCC 2008-005 LHCC-RD-016, April 4, 2008, CERN, 2008.

[74] D. Axen, et al., *Diamond detector irradiation tests at TRIUMF*, JINST **6** (2011) P05011.

[75] J. Ban et al., *Radiation hardness tests of the GaAs amplifiers operated in liquid argon in the ATLAS calorimeter*, Nucl. Inst. Meth. **A594** (2008) 389.

[76] J. Ban et al., *Cold electronics for the liquid argon hadronic end-cap calorimeter of ATLAS*, Nucl. Inst. Meth. **A556** (2006) 158–168.

[77] A. Rudert, for the HECPAS collaboration, *Upgrade of the Cold Electronics of the ATLAS HEC Calorimeter for sLHC*, Proceedings of the TWEPP-09 Topical Workshop on Electronics for Particle Physics, Paris, 21-25 September 2009.

[78] H. Oberlack, for the HECPAS collaboration, *Upgrade of the Cold Electronics of the ATLAS HEC Calorimeter for sLHC - Generic Studies of Radiation Hardness and Temperature Dependence*, Proceedings of the NSS-2009 Nuclear Science Symposium, Orlando, 26-30 October 2009.

[79] N.J. Buchanan et al., *Design and implementation of the Front End Board for the readout of the ATLAS liquid argon calorimeters*, JINST **3** (2008) P03004.

[80] N.J. Buchanan et al., *Radiation qualification of the front-end electronics for the readout of the ATLAS liquid argon calorimeters*, JINST **3** (2008) P10005.

[81] D.M. Gingrich and S. Liu,, *Dead Time in the LAr Calorimeter Front-End Readout*, ATLAS Liquid-Argon Calorimeter Note, ATL-LARG-2003-003 (2003).